UNIVERSIDADE FEDERAL DE UBERLÂNDIA
FACULDADE DE ENGENHARIA MECÂNICA
PÓS-GRADUAÇÃO EM ENGENHARIA MECÂNICA

A Contribution to the Study of Composite Shaft Onboard Rotors

Vergílio Torezan Silingardi Del Claro

Uberlândia

2020

Vergílio Torezan Silingardi Del Claro

A Contribution to the Study of Composite Shaft Onboard Rotors

Tese apresentada ao Programa de Pós-graduação em Engenharia Mecânica da Universidade Federal de Uberlândia, como parte dos requisitos para obtenção do grau de Doutor em Engenharia Mecânica.

Área de Concentração: Vibrações e Projeto Mecânico
Linha de pesquisa: Dinâmica de Máquinas Rotativas

Uberlândia, 26 de Maio de 2020.

Banca examinadora:

Prof. Dr. Valder Steffen Jr., Orientador (UFU - Universidade Federal de Uberlândia)
Prof. Dr. Aldemir Aparecido Cavalini Jr. (UFU - Universidade Federal de Uberlândia)
Prof. Dr. Ilmar Ferreira Santos (DTU - Denmark Technical University)
Prof. Dr. Rogério Sales Gonçalves (UFU - Universidade Federal de Uberlândia)
Prof. Dr. Volnei Tita (EESC USP - Escola de Engenharia de São Carlos da Universidade de São Paulo)

A Contribution to the Study of Composite Shaft Onboard Rotors

Dados Internacionais de Catalogação na Publicação (CIP)
Sistema de Bibliotecas da UFU, MG, Brasil.

D345c
2020

Del Claro, Vergilio Torezan Silingardi, 1991-
A Contribution to the study of composite shaft onboard rotors [recurso eletrônico] / Vergilio Torezan Silingardi Del Claro. - 2020.

Orientador: Valder Steffen Junior.
Coorientador: Aldemir Aparecido Cavalini Junior.
Tese (Doutorado) - Universidade Federal de Uberlândia, Programa de Pós-Graduação em Engenharia Mecânica.
Modo de acesso: Internet.
Disponível em: http://doi.org/10.14393/ufu.te.2020.3907
Inclui bibliografia.
Inclui ilustrações.

1. Engenharia Mecânica. I. Steffen Junior, Valder, 1991-, (Orient.). II. Cavalini Junio, Aldemir Aparecido, 1983-, (Coorient.). – III. Universidade Federal de Uberlândia. Programa de Pós-Graduação em Engenharia Mecânica. III. Título.

CDU:621

Gloria Aparecida - CRB-6/2047

UNIVERSIDADE FEDERAL DE UBERLÂNDIA
Coordenação do Programa de Pós-Graduação em Engenharia Mecânica
Av. João Naves de Ávila, nº 2121, Bloco 1M, Sala 212 - Bairro Santa Mônica, Uberlândia-MG, CEP 38400-902
Telefone: (34) 3239-4282 - www.posgrad.mecanica.ufu.br - secposmec@mecanica.ufu.br

ATA DE DEFESA - PÓS-GRADUAÇÃO

Programa de Pós-Graduação em:	Engenharia Mecânica				
Defesa de:	Tese de Doutorado, nº 300, COPEM				
Data:	26/05/2020	Hora de início:	08:00	Hora de encerramento:	11:00
Matrícula do Discente:	11613EMC014				
Nome do Discente:	Vergílio Torezan Silingardi Del Claro				
Título do Trabalho:	A Contribution to the Study of Composite Shaft Onboard Rotors				
Área de concentração:	Mecânica dos Sólidos e Vibrações				
Linha de pesquisa:	Dinâmica de Sistemas Mecânicos				
Projeto de Pesquisa de vinculação:					

Reuniu-se no Auditório do MFLab, bloco 5P, Campus Santa Mônica, da Universidade Federal de Uberlândia, a Banca Examinadora, designada pelo Colegiado do Programa de Pós-graduação em Engenharia Mecânica, assim composta: Professores Doutores: Rogério Sales Gonçalves - FEMEC/UFU; Aldemir Aparecido Cavalini Júnior - FEMEC/UFU; Volnei Tita - EESC/USP; Ilmar Ferreira Santos - Danmarks Tekniske Universitet/Dinamarca e; Valder Steffen Júnior - FEMEC/UFU, orientador do candidato. Ressalta-se que o Prof. Volnei Tita e o Prof. Ilmar Ferreira Santos participaram da defesa por meio de vídeoconferência desde a cidade de São Carlos/SP e Copenhague/Dinamarca, respectivamente, em atendimento a Portaria nº 36, de 19 de março de 2020 da Coordenação de Aperfeiçoamento de Pessoal de Nível Superior - CAPES, e o orientador, professores da FEMEC e o aluno participaram *in loco*.

Iniciando os trabalhos o presidente da mesa, Dr. Valder Steffen Júnior, apresentou a Comissão Examinadora e o candidato, agradeceu a presença do público, e concedeu ao Discente a palavra para a exposição do seu trabalho. A duração da apresentação do Discente e o tempo de arguição e resposta foram conforme as normas do Programa.

A seguir o senhor(a) presidente concedeu a palavra, pela ordem sucessivamente, aos(às) examinadores(as), que passaram a arguir o(a) candidato(a). Ultimada a arguição, que se desenvolveu dentro dos termos regimentais, a Banca, em sessão secreta, atribuiu o resultado final, considerando o(a) candidato(a):

Aprovado.

Esta defesa faz parte dos requisitos necessários à obtenção do título de Doutor.

O competente diploma será expedido após cumprimento dos demais requisitos, conforme as normas do Programa, a legislação pertinente e a regulamentação interna da UFU.

Nada mais havendo a tratar foram encerrados os trabalhos. Foi lavrada a presente ata que após lida e achada conforme foi assinada pela Banca Examinadora.

Documento assinado eletronicamente por **Valder Steffen Junior**, **Professor(a) do Magistério Superior**, em 26/05/2020, às 10:51, conforme horário oficial de Brasília, com fundamento no art. 6º, § 1º, do Decreto nº 8.539, de 8 de outubro de 2015.

Documento assinado eletronicamente por **Aldemir Aparecido Cavalini Junior**, **Professor(a) do Magistério Superior**, em 26/05/2020, às 10:52, conforme horário oficial de Brasília, com fundamento no art. 6º, § 1º, do Decreto nº 8.539, de 8 de outubro de 2015.

Documento assinado eletronicamente por **Volnei Tita**, **Usuário Externo**, em 26/05/2020, às 10:52, conforme horário oficial de Brasília, com fundamento no art. 6º, § 1º, do Decreto nº 8.539, de 8 de outubro de 2015.

Documento assinado eletronicamente por **Rogerio Sales Gonçalves**, **Professor(a) do Magistério Superior**, em 26/05/2020, às 10:52, conforme horário oficial de Brasília, com fundamento no art. 6º, § 1º, do Decreto nº 8.539, de 8 de outubro de 2015.

Documento assinado eletronicamente por **Ilmar Ferreira Santos**, **Usuário Externo**, em 01/06/2020, às 16:02, conforme horário oficial de Brasília, com fundamento no art. 6º, § 1º, do Decreto nº 8.539, de 8 de outubro de 2015.

A autenticidade deste documento pode ser conferida no site https://www.sei.ufu.br/sei/controlador_externo.php?acao=documento_conferir&id_orgao_acesso_externo=0, informando o código verificador **2047771** e o código CRC **7D54B12B**.

Acknowledgments

I greatly thank my three advisors, Prof. Dr. Valder Steffen Jr., Prof Dr. Aldemir A. Cavalini Jr. and Prof. Dr. Ilmar F. Santos, for their outstanding support and assistance in the development of this work. I am also thankful to Prof. Dr. Erasmo Carrera and his work group for the development and spreading of the Unified Formulation, which has significantly contributed to the present PhD dissertation.

For their financial and institutional support I am thankful to the following organizations: CNPQ - for my PhD scholarship; CAPES - for the PDSE program scholarship; UFU/POSMEC/LMEst - for the physical facilities, laboratories and institutional support; and finally DTU - for hosting me and providing funds and manufacturing services for the construction of one of the test-rigs used in my research work.

I thank also my friends, peers and co-workers from both LMEst and DTU Mek, for their continued friendship and invaluable insights during the course of this Dissertation. A special thanks go for Msc. Paulo C. P. F. Barbosa and Msc. Marcelo S. Sousa Jr., for their companionship througout the course of their Master's Thesis, which were essential for the present work.

Lastly, a personal acknowledgment goes for my family, for their continuing support and care all along these past years.

”It is my great regret that we live in an age that is proud of machines that think and suspicious of people who try to.”

“Adept Koriel Zeth” in the novel Mechanicum by Graham McNeill

Resumo

Del Claro, V. T. S. *Uma Contribuição ao Estudo de Rotores Embarcados com Eixo de Material Composto*. Tese de Doutorado - Universidade Federal de Uberlândia, Março 2020.

O entendimento atual sobre dinâmica de máquinas rotativas, e a capacidade de modelar e prever o comportamento físico destes sistemas rotativos, tem historicamente crescido em saltos. Tempos recentes têm visto um grande interesse no emprego de eixos de materiais compostos avançados e sistemas rotativos para uma miríade de máquinas industriais e novos equipamentos.

Sendo assim, esta Tese de Doutorado apresenta a revisão de formulações de Elementos Finitos tradicionais e a implementação de métodos inovativos, adaptados para a modelagem de sistemas rotativos. Modelos acessórios para componentes dedicados dos sistemas e para fenômenos físicos específicos são também revisados e incluídos nos modelos de Elementos Finitos. Um modelo baseado na Teoria Clássica de Vigas com eixos em material composto e dinâmica embarcada é desenvolvido, seguido por um modelo de Teoria Unificada com capacidades adicionais.

Três bancadas de testes experimentais são construídas e utilizadas na validação destas metodologias, permitindo uma boa representação do comportamento dinâmico dos rotores. Um diagrama cascata adaptado é também apresentado como uma forma alternativa de interpretar a solução do modelo de Formulação Unificada completo.

Palavras-chave: Dinâmica de Rotores. Dinâmica Embarcada. Eixo em Material Composto. Formulacão Unificada. MEF.

Abstract

Del Claro, V. T. S. *A Contribution to the Study of Composite Shaft Onboard Rotors*. PhD Dissertation - Federal University of Uberlândia, March 2020.

The current understanding of rotordynamics and together with the capacity of modeling and predicting the physical behavior of such rotor systems have historically grown in bursts. Recent times have seen a great interest on the employment of advanced composite shafts and rotor systems for a myriad of industrial machines and innovative equipments.

Consequently, this PhD Dissertation presents the review of traditional methods and the implementation of innovative Finite Element formulations adapted to the modeling of rotating systems. Accessory models for dedicated system components and specific physical phenomena are also revised and included into the Finite Elements models. An onboard composite shaft Classical Beam Theory model is developed, followed by an Unified Formulation model with additional capabilities.

Three independent experimental test-rigs are utilized in the methodologies validation, reaching good representation of the rotors mechanical behavior. An adapted waterfall diagram is also presented as an alternative form of interpreting a full Unified Formulation model solution.

Keywords: Rotordynamics. Onboard Dynamics. Composite Shaft. Unified Formulation. FEM.

Publications

The research done in this PhD Dissertation either resulted on, or contributed to developing the publications listed below:

Journal Papers

- M. S. Sousa Jr., **V. T. S. Del Claro**, A. A. Cavalini Jr. and V. Steffen Jr., “Numerical investigation on the dynamic behavior of an onboard rotor system by using the FEM approach”, Journal of the Brazilian Society of Mechanical Sciences and Engineering, (2017) 39:2447–2458, DOI 10.1007/s40430-016-0640-5. (https://link.springer.com/article/10.1007

- P. C. P. F. Barbosa, **V. T. S. Del Claro**, M. S. Sousa Jr., A. A. Cavalini Jr. and V. Steffen Jr., “Experimental analysis of the SHBT approach for the dynamic modeling of a composite hollow shaft”, Composite Structures, (2020) Volume 236, 15 March 2020, 111892. (https://doi.org/10.1016/j.compstruct.2020.111892)

Conference Papers and Annals

- **V. T. S. Del Claro**, A. A. Cavalini Jr., I. F. Santos and V. Steffen Jr., “N-th Order Unified Formulation Model for Rotordynamics”, Proceedings of the COBEM 2019, ID 1048, ABCM, Uberlândia-MG, Brazil, 2019.

- P. C. P. F. Barbosa, **V. T. S. Del Claro**, M. S. Sousa Jr., A. A. Cavalini Jr. and V. Steffen Jr., “SHBT Based Modeling of a Composite Hollow Shaft Regarding Its Dynamic Behavior Prediction”, Proceedings of SIRM 2019 – 13th International Conference on Dynamics of Rotating Machines, Copenhagen, Denmark, 13th – 15th February 2019.

- P. C. P. F. Barbosa, M. S. Sousa Jr., **V. T. S. Del Claro**, A. A. Cavalini Jr. and V. Steffen Jr., “Numerical Evaluation of an Onboard Composite Hollow Shaft”, MECSOL 2019 - Proceedings of the 7th International Symposium on Solid Mechanics, ABCM, São Carlos-SP, Brazil, April 15th to 17th, 2019.

- **V. T. S. Del Claro**, P. C. P. F. Barbosa, A. A. Cavalini Jr. and V. Steffen Jr., “A Shell Based Fem Model for Thick Walled Composite Rotors”, Proceedings of the COBEM 2017, ID 2118, ABCM, Curitiba-PR, Brazil, 2017.
- M. S. Sousa Jr., **V. T. S. Del Claro**, A. A. Cavalini Jr. and V. Steffen Jr., “Experimental Validation of an Onboard Rotor Fem Model”, Proceedings of the COBEM 2017, ID 1956, ABCM, Curitiba-PR, Brazil, 2017.
- P. C. P. F. Barbosa, **V. T. S. Del Claro**, A. A. Cavalini Jr. and V. Steffen Jr., “A Comparison Between Composite Rotordynamics Modeling Theories”, Proceedings of the COBEM 2017, ID 2073, ABCM, Curitiba-PR, Brazil, 2017.
- M. S. Sousa Jr., **V. T. S. Del Claro**, A. A. Cavalini Jr. and V. Steffen Jr., “Investigação Numérica e Experimental da Resposta Dinâmica de Rotores Embarcados à Excitação Senoidal da Base”, Annals of POSMEC 2017, Faculdade de Engenharia Mecânica, Universidade Federal de Uberlândia, Uberlândia-MG, Brazil, 2017.

Other publications, published during the period of the present PhD Dissertation but not directly connected to its mainstream subject, are listed below:

- L. R. R. Silva, **V. T. S. Del Claro**, C. Andrade, W. Guesser, M. Jackson and A. R. Machado, "Tool Wear Monitoring in Drilling of High Strength CGIs", Part B: Journal of Engineering Manufacture, (2020) JEM-19-0781.R1. (Accepted for publication, waiting for DOI number).
- A. A. Vilela, **V. T. S. Del Claro**, H. M. Torezan-Silingardi, K. Del-Claro, "Climate changes affecting biotic interactions, phenology, and reproductive success in a savanna community over a 10-year period, Arthropod-Plant Interactions,(2017) Springer, DOI 10.1007/s11829-017-9572-y.
- A. L. Paiva, **V. T. S. Del Claro** and A. A. Cavalini Jr., "Modelagem, Construção e Validação Experimental de um Sistema Massa-Mola-Amortecedor de Três Graus de Liberdade", Annals of 25º Congresso Nacional de Estudantes de Engenharia Mecânica, ABCM, Brasília-DF, Brazil, 2018.

- I. A. Pereira, L. S. Leão, **V. T. S. Del Claro** and A. A. Cavalini Jr., “A Didactic Test-rig Design for Mechanical Vibrations Courses”, Proceedings of the COBEM 2019, ABCM, Uberlândia-MG, Brazil, 2019.

Table of Contents

List of Figures

List of Tables

List of Symbols

Abbreviations

ABS	Acrylonitrile Butadiene Styrene
BW	Backwards critical speed for a rotor system
CBT	Classical Beam Theory, such as Euler-Bernoulli or Timoshenko theories
$COCBT$	First model proposed, having a Timoshenko CBT with added onboard dynamics, composite material considerations via SHBT approach and dynamic stiffening terms
CPT	Classical Plate Theory, such as Kirchhoff plate theory
CST	Classical Shell Theory, such as Kirchhoff-Love assumptions
CUF	Carrera Unified Formulation
$DoFs$	Degrees of Freedom
$DTUMek$	Department of Mechanical Engineering at DTU
DTU	Denmark Technical University
EMA	Experimental Modal Analysis
$EMBT$	Equivalent Modulus Beam Theory
EoM	Equation of Motion
FEM	Finite Elements Method
$FEMEC$	Mechanical Engineering Faculty of the Federal University of Uberlândia
$FESS$	Flywheel Energy Storage Systems
FN	Fundamental Nuclei
FW	Forwards critical speed for a rotor system
$LMEst$	Structural Mechanics Laboratory at UFU
NI	National Instruments
PC	Polycarbonate
PCB	Printed Circuit Board

PVD	Principle of Virtual Displacements
$SHBT$	Simplified Homogenized Beam Theory
SHM	Structural Health Monitoring
SMA	Shape Memory Alloy
UF	Unified Formulation, nomenclature adopted as a general rule
$UF2$	Second model proposed, having a complete second order B2 UF model, with composite material considerations via SHBT approach and dynamic stiffening terms
UFU	Federal University of Uberlândia

FEM Matrices (Valid for CBT and UF formulations, unless indicated differently)

$[\cdots]$	No sub-index, indicates global-level matrix	$[-]$
$[\cdots]_e$	Sub-index e, indicates element-level matrix	$[-]$
$[\cdots]_{mod}$	Sub-index mod, indicates modal matrix	$[-]$
$[\cdots]_n$	Sub-index n, indicates node-level matrix	$[-]$
$[C]$	Shaft composite damping matrix	Ns/m
$[C_b]$	Bearing localized damping	Ns/m
$[G]$	Shaft gyroscopic effect matrix	Ns/m
$[G_d]$	Disk gyroscopic effect matrix	Ns/m
$[K]$	Shaft ortho and isotropic K with Coriolis and Coupled terms	N/m
$[K_b]$	Bearing localized stiffness	N/m
$[K_d]$	Disk K (only used when disks are bonded to shaft)	N/m
$[K_O]$	Shaft dynamic stiffening matrix	N/m
$[K_S]$	Shaft centrifugal force stiffening matrix	N/m
$[K_T]$	Shaft torque induced stiffening	N/m
$[K_{Od}]$	Disk dynamic stiffness matrix	N/m
$[K_{Sd}]$	Disk centrifugal forces matrix (only used with K_d)	N/m
$[M]$	Shaft standard mass matrix	kg
$[M_d]$	Disk standard mass matrix	kg
$CONN$	Connectivity matrix	$[-]$
$DOFMAT$	Matrix of the degrees of freedom per node	$[-]$

Constants and Variables

ν	Poisson coefficient, with sub-indexes ij $(i,j = 1,2,3)$	$[-]$

ω_d	Damped natural frequency	Hz
ω_n	Undamped natural frequency	Hz
Ω	System rotation speed around "*y*" axis	rpm
E	Young modulus, with sub-indexes 1,2 and 3	Pa
G	Shear modulus, with sub-indexes 12,13 and 23	Pa
N	Number of nodes per element, determining the order of the interpolation in the length direction	$[-]$
T	Expansion order for the cross-section Taylor-like polynomials	$[-]$
t	Time	s

Chapter 1

Introduction

Throughout history, rotating machines were essential for a number of human activities. From transportation to mechanical power transmission, encompassing energy generation and almost all forms of movement, rotors and shafts are a common feature in machines and mechanical devices. Following the trend in most engineering sciences, wars and violent conflicts played an important role on the initial development and understanding of rotordynamics, settling the fundamentals of this science as it is understood today. Naturally, due to strategic value, rotors have been thoroughly studied and analyzed by a number of nations and companies. These efforts resulted in a variety of mathematical and physical models, offering ever closer similarity to the complete real physics of the experimental phenomena observed.

1.1 Rotordynamics History and State-of-the-art

Initial models considered shafts to be rigid, operating below what is currently called the *first critical speed*, as proposed by Rankine [42]. In this situation, the system dynamics is ruled by the bearings stiffness and damping, but also by the inertia of the shaft and disks. With this basic understanding, the first balancing technique was developed by Lawaczeck in 1907, for the Schenck Company, allowing for safer and faster machines. This trend of more stable and reliable systems is one of the most common features of rotordynamics studies, further developed by the rotor model proposed by Jeffcott [30]. In 1924, many important developments were published, namely: a) the first use of the *Campbell Diagram*, developed by the Campbell Corp.; b) initial studies of oil induced excitations in fluid-film bearing rotors [38]; c) a simple model for intrinsic material damping, namely the *internal damping* [32]; d) De Laval rotor, a steam turbine operating above the first critical speed and proving that this limit was not definitive [57]. Additional developments were made on the following decade on balancing techniques [58] and the first asymmetric shaft rotor model was presented [53]. The first numerical techniques applied for rotordynamics came in 1945 [41]. During the decade following the end of WWII, several new developments were achieved, following the need for aeronautical engines, steam turbines and faster rotating systems. Some of these were the first non-linear models for rotors [61] and the first air-foil bearing rotors, developed by the Garrett Corp. by the end of the fifties. Last century, further developments are found in the next decades, developing new and improved techniques on already established fields: a) the continuous rotor model was proposed in 1959 [7], along with a modal balancing technique by the same author [6]; b) asymmetrical rotors were studied and modeled [10]; c) the self-excited vibration phenomena known as *rubbing* was described and studied [8]; d) the Finite Elements Method (FEM) was applied to rotordynamics in 1972 [43]. After this burst of development, the fundamentals of rotordynamic theories were established. A few audacious new projects were also proposed a few years later, such as the first magnectic bearings [46] and the first cracked shaft models [27]. A decade later, a model for rotor control via active bearings was proposed [39]. Synthesizing this historical review, an extended diagram similar to the one presented in [62] can be seen in Figure 1.1.

Major advancements on rotordynamics came with the use of composite shafts on flexible rotors, since they overcame intrinsic limitations of metallic rotors [48]. The low weight of composites allows for faster acceleration and deceleration as compared with conventional rotating machines [11], thus reducing effects related to rotational inertia. An unfortunate side-effect however, is that composites have a more complex behavior than isotropic materials, and in supercritical operations the vibration responses demand special attention [29] to ensure a safe operation [22], [52]. Nevertheless, it is possible to change the stiffness and damping properties of the composite material by manipulating some physical and geometrical characteristics [2]. Additionally, it is possible to attenuate the vibration amplitudes when the system undergoes critical speeds, depending on the structural damping properties of the composite [36], which signifi-

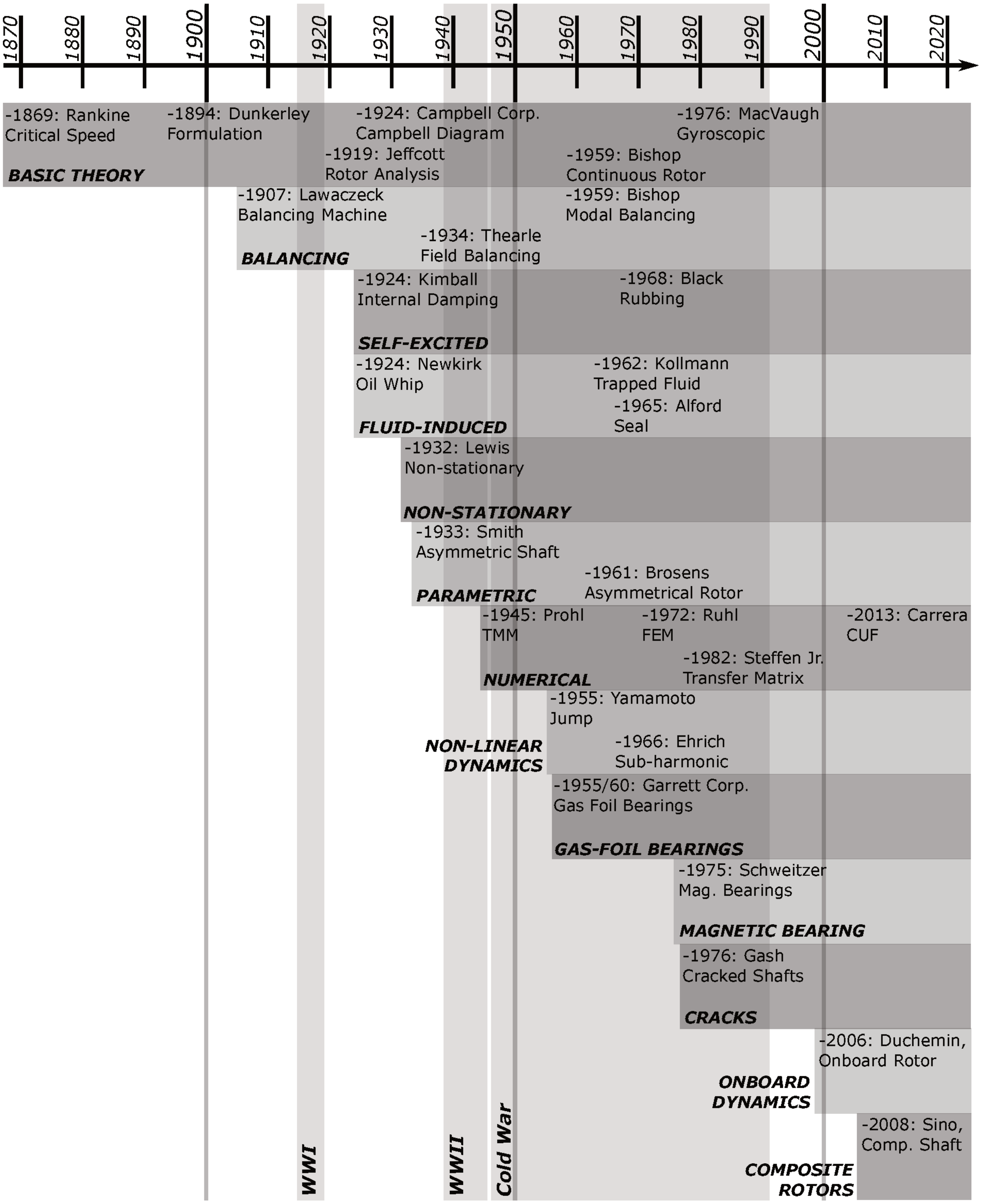

Figure 1.1: Rotordynamics historical timeline, divided by field of study, marking some milestone advancements of each area

cantly influences the dynamic response of the system [12], [60]. Despite the complexities added by the usage of composites, these can be turned into advantages via an adequate material representation. For this aim, one considers each ply fiber angle, composite internal damping properties and, depending on the precision needed, other in depth considerations. Another upcoming possibility is a parameter sensitivity analysis for evaluating the influence of each ply physical constants (such as Young Modulus, Poisson Coefficient and Transverse Shear Modulus) depending on the system rotation speed. Recent studies have shown that the sensitivity of each constant varies significantly with the rotation speed and with the frequency of excitation forces [47], leading to new possibilities for the optimal design of composite rotors. A model capable of realistically modeling the ply-dependent properties could, theoretically, be used to optimize a rotor shaft for a given set of requirements, taking into consideration the sensitivity of these properties.

Mechanical flywheels are common devices since the development of internal combustion engines, and have recently re-emerged as a relevant industrial solution. Consequently, their overall mechanical behavior and dynamic interaction with the structure (onboard dynamics) have become a focus of scientific developments. This is due to the applicability of high-speed composite flywheels as energy storage systems, as applied to vehicles such as cargo freighter ships and offshore platforms [20]. Despite the application, either a thorough study of the onboard dynamics or some mechanical device to decouple the base from the rotor dynamics often proves to be necessary [21]. The current trend is the replacement of metallic flywheel systems by composite ones, since the rotation speed has a squared influence over the kinetic energy. A comparative study on flywheel material for relative power storage capacity was made as early as 1977, by Kirk [33]. Therefore, high-speed and high-inertia systems made of orthotropic materials are preferred over the traditional metallic ones, leading to problems related to the moving base influence over these systems [54] [56]. Such developments lead to another technical challenge, *i.e.* the modeling of complex rotating geometries operating at above-critical speeds [14]. These systems demand high order models to accurately represent the stress-strain relations of the moving structure over a thick cross-section. Considering their geometry, material property and wall thickness characteristics, simplified models are unsuited for this application [23] [5]. These complexities have pushed the development of advanced models, featuring improved physical representation of the real systems. Numerous FEM formulations, based on the Simplified Homogenized Beam Theory, Equivalent Modulus Beam Theory, Classical Plate and Shell Theories and Layerwise models, have been recently proposed for the analysis of composite material shafts by different authors.

This approaches follow a general rule, *i.e.* sufficiently accurate models, while keeping the computational cost low enough for the problem to be solvable for practical situations. The Equivalent Modulus Beam Theory (EMBT) [59], such as the one applied in the contribution shown by [50], can be effectively used for the modeling of tubular composite shafts. This method can even be extended to represent rotating dynamics accordingly, with only a few limitations [28]. A Layerwise Beam Theory (LBT) [50] presents an excellent prediction of the composite shaft dynamics on various applications, regardless of the cross-section geometry or thickness, but leads to a prohibitively high computational cost [17]. An intermediary approach was studied, resulting on modified EMBT [2] models and the Simplified Homogenized Beam Theory (SHBT) [51]. The SHBT model was further developed to include onboard dynamics and additional physical considerations, such as composite internal damping and acceleration effects of rotor dynamics [5]. Alternate solutions, such as the Rayleigh-Ritz method, were also recently used for composite shafts [19]. An Unified Formulation (UF) was presented by Carrera (CUF), where a methodology to determine the best theory for a given problem [16] was explored. This methodology allows for arbitrary degree polynomial shape functions and arbitrary number of nodes per element to be chosen, leading to a very general framework. The CUF was also adapted to rotating systems [15], and later modified to include internal orthotropic material damping and stiffening effect due to acceleration [23].

1.1.1 Institutional Background

Accompanying the resurgence of rotordynamics studies on the last few decades, a number of contributions were made by the host institutions of this research effort. The Mechanical Engineering Faculty of the Federal University of Uberlândia (FEMEC-UFU) and the Department of Mechanical Engineering of the Technical University of Denmark (DTU Mekanik) have both performed numerous contributions. In the context of smart rotors, the Structure Mechanics laboratory at UFU (LMEst) and the rotordynamics research group at DTU are protagonists. Concentration areas are not only classical rotordynamics, but also mechanical vibrations modeling and control, non-linear dynamics formulations, composite and smart-materials, magnetic bearings, multiple FEM methodologies and other numerical methods.

Keeping the focus on rotordynamics and related areas, contributions began as early as in 1981, with Prof. Steffen Jr.'s publication on rotordynamics, already encompassing numeric and experimental investigations [31]. Later, Prof. Santos intensive effort on bearing modelling, understanding and control initiated with stability studies on journal bearings [45]. An application of piezoelectric materials on rotor control was then presented [49], continued by an application of Shape Memory Alloys (SMA) on bearing supports for vibration damping [44]. Nonlinearities were then approached by the study of another rotor system, as shown in [37]. Structural Health Monitoring (SHM) techniques were then adapted to rotor systems in Prof. Cavalini Jr. studies [18], detecting incipient cracks via electromechanical impedance technique. Inovative bearings with embedded electromagnetic actuators were used to control and stabilise an experimental rotor test-rig [34]. Another application of SMA to bearing stiffness tuning and rotor control was then presented [1], followed by an investigation on magnetic bearings for supercritical rotors control [40]. This control technique for magnetic bearings was then improved by ensuing works [9], aiming at robustness and reliability. Composite shafts used on a complete test-rig were revisited, this time with a hollow composite shaft [19]. Continued efforts lead to Barbosa's MSc Thesis and associated publications, developed in tandem with the present work [2]. On a parallel line, onboard rotordynamics were studied by Souza Jr.'s MSc Thesis [54], also in cooperation with the present research work.

Contextualized in LMEst, and resulting of a line of previous research efforts, the present doctoral study aims at improving the current understanding of rotordynamics by the introduction of a fundamentally improved shaft model. The previous couple of MSc theses developed in partnership with this work, and the international cooperation with DTU Mekanik greatly enriched the research area of rotordynamics and its ensuing contributions.

1.2 Research goals

Considering the areas of interest presented in the previous sections, the current PhD Dissertation focus on model development of composite-shaft onboard rotor systems. The challenges faced by recent projects in this area demand high-fidelity models, capable of considering a number of characteristics of rotating system design, such as: a) orthotropic and multi-layer materials; b) complex cross-section geometries; c) thick and thin-walled shafts; d) membrane and plate-like wall deformations; e) onboard dynamics and rotor-mount interaction.

In this scenario, we hypothesize that a model capable of representing these characteristics of a rotor system is viable. Therefore, the main objective of the present Doctoral Dissertation is the development of a Finite Elements rotor model with extended damping and orthotropic material considerations, which is capable of accurately representing thick-walled composite shafts with onboard dynamics.

Secondary goals of this project include the development of other desirable model features, such as:

> comparatively low computational cost;
> layerwise or adequate equivalent layer material physics;
> aptitude for arbitrary cross-section geometry and wall thickness;
> detection of membrane and plate-like wall deformations, such as wrinkling, warping, etc.;
> proper representation of transient dynamic effects, such as shaft stiffening;
> shear stress representation;
> easily adaptable formulation.

Ideally, the final model would be easily adaptable with respect to rotor geometry, material and mechanical construction, producing 3D-like results with low computational cost. In this sense, any other achieved improvement or additional capacity brought to the model is considered beneficial to the present research end goal.

1.2.1 Proposed Models

The development of this work led to two major computational models, both being thoroughly experimentally validated. The first model meets the main research objectives, and the second covers also the secondary goals.

The initial approach to the problem was the modification of a Timoshenko beam SHBT model [51]. It had the addition of orthotropic and isotropic mechanical properties and internal material damping models, dynamic stiffening effects due to acceleration variations, onboard dynamics [35] considerations and associated time integrator solver development. This model was initially developed as two separate models, both based on the same Timoshenko rotor model, the first one to validade the onboard dynamics and the other to validate the composite SHBT physics, extra dynamic effects and material properties. These two models were later validated by using dedicated test-rigs. Once the validation was achieved for both models, they were merged into a single model, capable of representing moderately thick-walled composite onboard rotors. This model is already adequate for the vast majority of industrial applications, but still relies on a number of simplifications and approximations. The initial model development is justified by the extensive effort needed, which was helped by two MSc theses, elaborated in tandem with this PhD project. One of these theses was dedicated to onboard rotordynamics, developed by Marcelo S. Souza Jr., while the other has studied composite shaft rotors, elaborated by Paulo C. P de F. Barbosa. Having achieved the main research goals with this merged model, the secondary objectives were pursued.

All additional physics developed and validated with the initial models were great additions to the dynamic representation of rotors, and were carried out to the final model. This included the Onboard Dynamics, the Composite SHBT representation, the dynamic stiffening matrices and the internal material damping. After observing the limitations of the initial model, a radically different approach was pursued. The Carrera Unified Formulation (CUF) [13] model, adapted to rotordynamics [15] was used as the framework upon which this formulation was built. This model, from here on denominated *UFRotor*, carried on all the already validated advancements produced. The advantages of UF models over standard FEM models are numerous, but the biggest ones are the versatility and ease of modeling adaptation. The drawbacks are a considerably more generalistic coding and heavily modified post-processing operations, as compared with standard and well known FEM procedures. Since the UF allows for arbitrary shape functions, and no assumptions are made regarding both the beam cross-section geometry and material composition, this model flawlessly achieves all of the secondary goals of this research work.

1.2.2 Experimental Test-rigs

For model validations, three independent test-rigs were built and experimentally tested for relevant data gathering. The experimental data sets obtained were then compared to the numerical model results, ensuring an adequate prediction of the physical phenomena involved.

The first test-rig was designed to be operated as installed on a mechanical shaker, in a manner that the whole system is excited through the shaker baseplate movements, as seen in Figure 1.2.

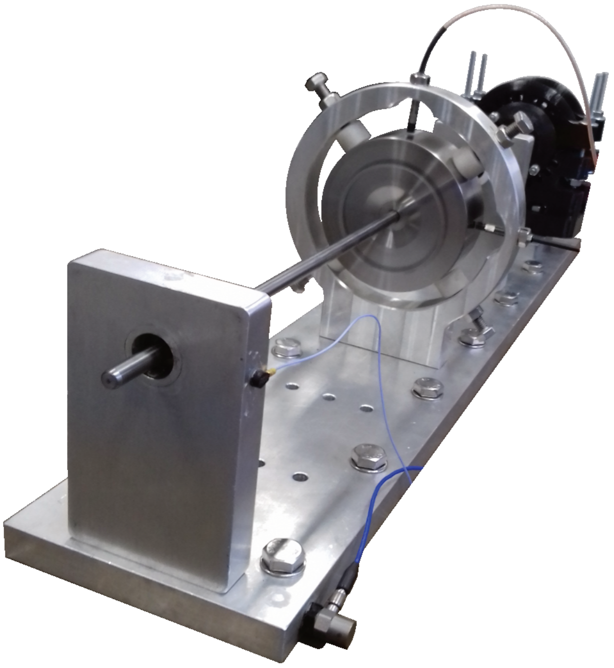

Figure 1.2: Onboard rotor test-rig overview

This test-rig design consisted of a simple slender shaft, with a heavy disc and two self aligning ball bearings, mounted on the top of an electromechanical shaker plate. The base movement was controllable, and a number of different entries were used as base movement parameters, thus simulating realistic situations. The data was captured in the disk *xz* plane, via a pair of proximeters. A couple of accelerometers were also used to detect the response of the baseplate and in the second bearing horizontal line.

Their responses were used to control the shaker in a feedback loop configuration, but also to check the base response and eventual unexpected bearing movements, relative to the baseplate. All experimental data obtained from this test-rig was naturally used for the onboard dynamics theory validation.

A second test-rig was dedicated to the SHBT theory validation, consisting of an overhung composite rotor with two disks. The system, as depicted in Figure 1.3, has a multilayered carbon-epoxy shaft, with two metallic disks and two self aligning ball bearings, mounted on an inertial base.

Figure 1.3: Composite rotor test-rig overview

A number of time and frequency-domain responses were acquired by means of the four available proximeters mounted on both disks planes. No additional accelerometer measurement was deemed necessary as due to the inertial base where the system was mounted upon. The goal of this test rig was to obtain a thick-walled composite shaft response to intense excitation with a relatively complex geometrical configuration. A thin-walled tubular shaft is defined by having a wall thickness smaller than 10% of the radius, a moderately thick one stays between 10 and 30%, and a thick walled one is above 30%. In this manner, the model capabilities were tested to their limits.

The third experimental test-rig fabricated was used for the validation of the secondary objectives. This rotor system is composed of a tripartite metallic shaft, mounted again on two self aligning ball bearings, with a flywheel mounted on the shaft, as seen in Figure 1.4.

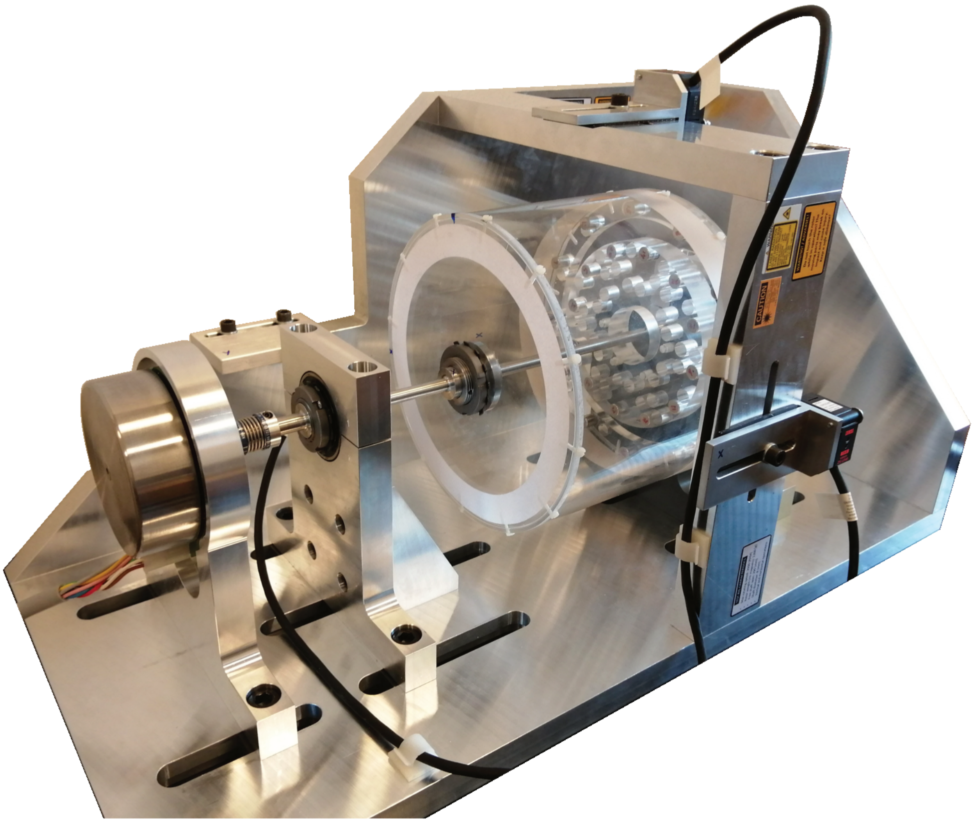

Figure 1.4: Flywheel rotor test-rig overview

The sensing system encompassed three laser proximeters, with a couple mounted on the flywheel end rotor plane along the *xz* direction, while the third one was mounted on the back, along the *y* direction. This rotor system was modeled by using the UFRotor model, via a number of different order formulations, in order to validate the model capacity to represent both the shaft and the flywheel itself, with UF beam elements. The main interest of these experiments was related to the coupled shaft-flywheel dynamics and their behavior at above critical speeds. Another interesting topic was the membrane deformations of the flywheel, which the model is capable of detecting. Some preliminary measurements of Experimental Modal Analysis (EMA) were conducted, by means of an accelerometer and an impact hammer, in order to obtain the Frequency Response Functions for multiple configurations of the system. This procedure permitted to identify which frequency was related to which mechanical component, and also to determine the mode shapes via modal reconstruction.

Counting on these three dedicated experiments, a considerable amount of comparison data was obtained and the theories proposed were tested accordingly.

1.3 Chapters Organization

This Doctoral Dissertation is organized according to a number of chapters, on a didactic manner, starting with the historical introduction and objectives definition presented above. The first chapter also presents a brief explanation about the computational models and how they were developed, followed by the test-rigs description.

Then, in Chapter 2 the fundamental mathemathical and computational developments made to achieve the primary research goals are presented. The mathematical formulation adopted for orthotropic material representation and SHBT equivalent layer theory are discussed. Internal damping equations either for isotropic or orthotropic material types, are presented via the Kelvin-Voight rheological model, adapted for the present methodology. Onboard rotordynamics is then approached, presenting the mathematical fundaments and numerical implementation of numerical integration solver algorithms. Finally, the Equation of Motion (EoM) for the initial Timoshenko beam FEM model is presented, thus achieving the primary objective of an onboard composite shaft rotor model. Associated bibliography, and publication results related to the first model and their two preliminary parts are is given to facilitate the understanding.

The Unified Formulation model is then presented in Chapter 3, starting with an explanation of the fundamental concepts and distinctions with respect to a standard FEM model. The arbitrary shape-functions and their resulting complications and capacities, along with the generalistic approach to the cross-section geometry and material properties are then described. Meshing and pre-integration procedures to generate the 3x3 Fundamental Nuclei (FN) are then thoroughly approached. Next, the many added physics terms are adapted and described so that they are included into the standard CUF FN assembly. These unfolded terms include disk-specific physics, unbalanced masses dynamics, bearings and boundary conditions application via penalty factors, transient stiffening due to acceleration terms and external forces considerations. Following with the UF model assembly, its computational part is then presented. The numerical procedure is covered from nodal to element to global-level terms, always for a linear behavior. Layerwise capacities are presented via an iterative loop covering each layer, and in a similar manner the onboard dynamics of the UFRotor is explained through an external iterative loop, for numerical integration convergence. The final UFRotor model is then presented in both its numerical and computational forms.

Next, the reader finds the experimental procedures and test-rigs description, in Chapter 4. One can find the mechanical and geometrical descriptions, electronics and data acquisition assembly and experimental tests performed. Detailed mechanical designs and blueprints for individual parts are presented as appended material. Initially, the onboard dynamics test-rig is presented in detail, seconded by the thick-walled composite rotor and finished by the flywheel dynamics test-rig description.

In Chapter 5, numerical and experimental results organization are exhibited and individual tests results are then presented and discussed based on their experimental origin order. The three test-rigs developed have their obtained datasets exposed, and comparisons with their corresponding numerical equivalents are depicted. Eventual numerical results comparisons are shown when a specific condition is to be highlighted. Arguments are presented over particular forms of results depiction, mainly for comparing the standard Campbell diagram with the Waterfall plot, which is more adapted to UF models. In this section a couple of numerical models is used: a) the preliminary model for composite onboard rotors based on Timoshenko beam theory; b) the final UFRotor model as developed over a heavily modified CUF beam framework. The preliminary models for onboard dynamics and SHBT composite validation are shown only for their merged form.

Concluding remarks and a thorough evaluation of the models and experiments developed along the study are presented in Chapter 6. The UFRotor capabilities and its performance comparison to a similar beam, plate/shell and solid element formulations is forwarded. An evaluation of the preliminary Timoshenko based model is made, exhibiting its range of applications and comparing its performance with the final UFRotor methodology. Thereafter, a brief comment over the test-rigs design, machining, their experimental results and usefulness is made. Lastly, future research perspectives and further scientific and technical challenges observed during the development of the present dissertation are brought to light.

Chapter 2

Mathematical Formulation

The mathematical formulation used in this research work was developed in two parts, as previously stated. Initially, a standard Timoshenko shaft model with a number of additions was used to validate some theoretical approaches. This will be denominated the "**CBT**" model, in reference to "Classical Beam Theory". This corresponds to the composite model, internal damping and onboard dynamics representations. A definitive UF model is then developed, including such previously validated theories. In the sequence, this will be denominated simply "**UF**" model, in reference to Carrera Unified Formulation and other generalized unified formulations. Their mathematical modeling is presented in the next sections, following a standard Lagrange formulation.

Since these preliminary theories and methods are used in both models, their explanation is presented in detail. Concerning the shaft and disc models, these components have clear distinctions in the CBT and UF theories. Being a classic approach, the CBT shaft model has been thoroughly studied and will not be further developed here. For additional references, please refer either to [5] in the case of composite modeling or to [54] in the case of onboard dynamics. Nevertheless, as the main contribution of this research is the UF model, this model is in-depth explored and explained in the following sections.

As a last introductory comment, the coordinate system adopted is the same for every case studied here. The x and z directions form the cross section plane of the considered reference frames, the first being horizontal and the latter vertical, with y being the axial direction.

2.1 Composite Modeling

Regarding the mechanical properties of the material that composes the shaft, both a traditional isotropic and an orthotropic composite formulation were implemented. The standard isotropic material model utilizes three mechanical properties in the generation of the mechanical properties matrix, namely the Young modulus (*E*), the Shear deformation modulus (*G*) and the Poisson coefficient (υ). For in depth description of this procedure, there are several mechanics of materials and finite elements fundamentals literature, such as [64]. Now, on the orthotropic composite material, five mechanical properties are used, defining an orthotropic but transversely isotropic material. These properties are then integrated in the composite layers by a Simplified Homogenized Beam Theory (SHBT), yielding an equivalent modulus for the shaft.

2.1.1 Orthotropic Materials Revisited

The mechanical properties matrix for an orthotropic material is presented in Equation 2.1,

$$C = \begin{bmatrix} C_{11} & C_{12} & C_{13} & 0 & 0 & 0 \\ C_{21} & C_{22} & C_{23} & 0 & 0 & 0 \\ C_{31} & C_{32} & C_{33} & 0 & 0 & 0 \\ 0 & 0 & 0 & C_{44} & 0 & 0 \\ 0 & 0 & 0 & 0 & C_{55} & 0 \\ 0 & 0 & 0 & 0 & 0 & C_{66} \end{bmatrix} \tag{2.1}$$

where the individual elements are given in Equation 2.2:

$$\begin{cases} C_{11} = (-\upsilon_{23} * \upsilon_{32} + 1)/(E_2 * E_3 * Delta) \\ C_{12} = C_{21} = (-\upsilon_{23} * \upsilon_{31} + \upsilon_{21})/(E_2 * E_3 * Delta) \\ C_{13} = C_{31} = (-\upsilon_{12} * \upsilon_{31} + \upsilon_{32})/(E_1 * E_3 * Delta) \\ C_{22} = (-\upsilon_{13} * \upsilon_{31} + 1)/(E_1 * E_3 * Delta) \\ C_{23} = C_{32} = (-\upsilon_{12} * \upsilon_{31} + \upsilon_{32})/(E_1 * E_3 * Delta) \\ C_{33} = (-\upsilon_{12} * \upsilon_{21} + 1)/(E_1 * E_2 * Delta) \\ C_{44} = G_{23} \\ C_{55} = G_{13} \\ C_{66} = G_{12} \\ Delta = \dfrac{(-2 * \upsilon_{13} * \upsilon_{21} * \upsilon_{32} - \upsilon_{12} * \upsilon_{21} - \upsilon_{13} * \upsilon_{31} - \upsilon_{23} * \upsilon_{32} + 1)}{(E_1 * E_2 * E_3)} \end{cases} \tag{2.2}$$

While this formulation is capable of modeling fully orthotropic materials, the ones used in this Thesis are transversely orthotropic, meaning that the terms with subindexes 12 and 13 are equal. A diagram featuring the variables and general disposition of the parameters is shown by Figure 2.1.

Such representation is sufficient for an uni or bi-directional fiber composite, covering most engineering materials used. Accounting now for the angular orientation of each individual ply, this base C matrix is rewritten in a new coordinate system, compensating for the relative orientation between the plies. The result is a full **C** matrix, where the individual terms are fully described in the Appendix B. The **C** coefficients are the ones used on the assembling of the FEM matrices and SHBT integration.

2.1.2 SHBT Integration Procedure

The previously developed coefficients are then subjected to a Simplified Homogenized Beam Theory integration (SHBT) procedure. It involves applying the full **C** matrix parameters for each layer, and integrating them into a single equivalent one. The equivalent properties are then introduced to the element or global-level matrices [51], depending on the formulation considered. This SHBT procedure represents any layer stacking sequence, also considering the distances of layers from the shaft center and

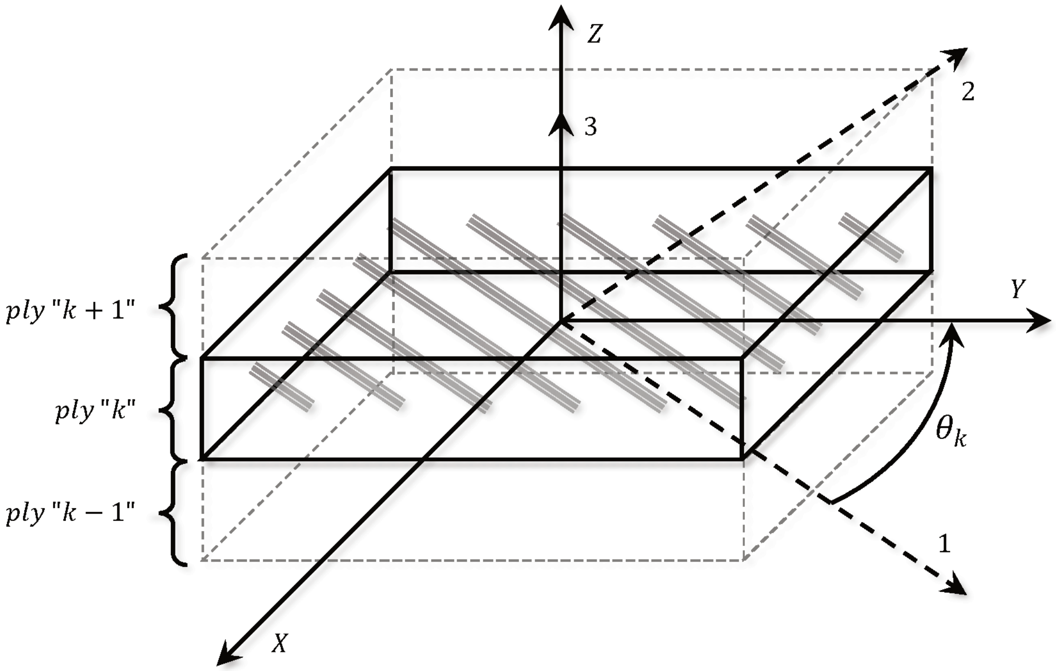

Figure 2.1: Composite multilayered material diagram

their order of stacking. The numeric procedure encompasses a summation of each mechanical property, compensating for the layer radius and fiber orientation.

As no assumptions are made regarding the shaft wall thickness to radius ratio, it is left as an arbitrary parameter. The cross-section geometry is however considered to be xz symmetric during the formulation of the internal damping, which is easily adaptable to other configurations, as necessary.

2.2 Internal Material Damping

The material internal damping is ruled by a Kelvin-Voight rheological model, as described by [51]. It is introduced to the ongoing formulation as additional stiffness and damping matrices due to the composite material influence. This model considers the energy dissipation as an equivalent viscous damping, modeled as a viscoelastic linear solid. The stress-strain relation for this model is adequately represented by a spring and damper mounted in parallel, as shown by Equation 2.3 and Figure 2.2.

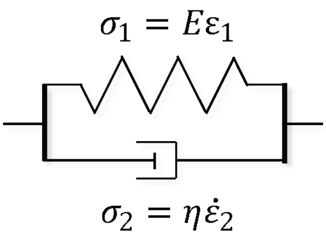

Figure 2.2: Kelvin-Voight internal damping model

$$\sigma = E\varepsilon + \eta\dot{\varepsilon} \tag{2.3}$$

In this equation, σ is the stress, ε the strain, and $E\varepsilon$ corresponds to the "spring" influence, while $\eta\dot{\varepsilon}$ is associated to the "damper" [60]. By applying a constant stress to the system, σ_0, the response behaves as a *fluence* effect, modeled by Equation 2.4.

$$\varepsilon(t) = \frac{\sigma_0}{E}(1 - e^{-(E/\eta)t}) \tag{2.4}$$

By applying the principle of virtual work to this formulation, one can obtain Equation 2.5:

$$\delta W = \int_0^L \int_S \sigma \delta\varepsilon dS dy \tag{2.5}$$

Later, by substituting the shape functions, $\mathbf{N}_1$ and $\mathbf{N}_2$, into Equation 2.5 and assuming that the shaft is symmetric relative to the x and z directions, we obtain:

$$\delta W = \alpha EI \int_0^L \left[\left(\frac{d^2\mathbf{N}_1{}^t}{dy^2}\frac{d^2\mathbf{N}_1}{dy^2} + \frac{d^2\mathbf{N}_2{}^t}{dy^2}\frac{d^2\mathbf{N}_2}{dy^2} \right)\dot{q} + \Omega\left(\frac{d^2\mathbf{N}_1{}^t}{dy^2}\frac{d^2\mathbf{N}_1}{dy^2} - \frac{d^2\mathbf{N}_2{}^t}{dy^2}\frac{d^2\mathbf{N}_2}{dy^2} \right) q \right] \delta q dy \tag{2.6}$$

Isolating the terms multiplied by q and $\dot{q}$ and rearranging the expression in matrix form, the additional composite stiffness and internal damping matrices are respectively obtained. These matrices are given by the Equations 2.7 and 2.8, for the CBT shaft element.

$$\mathbf{D}_i = K_L^{\alpha} \begin{bmatrix} 12 & 0 & 0 & -6L & -12 & 0 & 0 & -6L \\ 0 & 12 & 6L & 0 & 0 & -12 & 6L & 0 \\ 0 & 6L & (4+\vartheta_y)L^2 & 0 & 0 & -6L & (2-\vartheta_y)L^2 & 0 \\ -6L & 0 & 0 & (4+\vartheta_y)L^2 & 6L & 0 & 0 & (2-\vartheta_y)L^2 \\ -12 & 0 & 0 & 6L & 12 & 0 & 0 & 6L \\ 0 & -12 & -6L & 0 & 0 & 12 & -6L & 0 \\ 0 & 6L & (2-\vartheta_y)L^2 & 0 & 0 & -6L & (4+\vartheta_y)L^2 & 0 \\ -6L & 0 & 0 & (2-\vartheta_y)L^2 & 6L & 0 & 0 & (4+\vartheta_y)L^2 \end{bmatrix} \tag{2.7}$$

$$\mathbf{K}_i = K_L^{\alpha} \begin{bmatrix} 0 & -12 & -6L & 0 & 0 & 12 & -6L & 0 \\ 12 & 0 & 0 & -6L & -12 & 0 & 0 & -6L \\ 6L & 0 & 0 & -(4+\vartheta_y)L^2 & -6L & 0 & 0 & -(2-\vartheta_y)L^2 \\ 0 & 6L & (4+\vartheta_y)L^2 & 0 & 0 & -6L & (2-\vartheta_y)L^2 & 0 \\ 0 & 12 & 6L & 0 & 0 & -12 & 6L & 0 \\ -12 & 0 & 0 & 6L & 12 & 0 & 0 & 6L \\ 6L & 0 & 0 & -(2-\vartheta_y)L^2 & -6L & 0 & 0 & -(4+\vartheta_y)L^2 \\ 0 & 6L & (2-\vartheta_y)L^2 & 0 & 0 & -6L & (4+\vartheta_y)L^2 & 0 \end{bmatrix} \tag{2.8}$$

The additional constants utilized are defined by Equation 2.9

$$\alpha = \frac{\eta}{E} \ \mathit{and} \ K_L^{\alpha} = \frac{\alpha EI}{(1+\vartheta_y)L^3} \tag{2.9}$$

It is noteworthy that this methodology is presented in the framework of the first CBT model. As described, it considers a Timoshenko shaft model, with 4 DoFs per node and 2 nodes per element. The generalized coordinates found in the matrices of Equations 2.7 and 2.8 correspond to:

$$q = \{u_1,\ w_1,\ \theta_1,\ \phi_1,\ u_2,\ w_2,\ \theta_2,\ \phi_2\}^T \tag{2.10}$$

where u and θ are respectively translation and rotation along the x direction, while w and ϕ are the same, regarding the z direction. When transfering this formulation to an UF framework, one must change the generalized DoFs order accordingly. Should the

UF model have more DoFs per node, all additional lines (DoFs) should be completed with zeroes, matching the matrices size and DoFs order for the numerical assembling procedure. Eventhough the generalized UF considers different shape functions for the CBT, it is still valid to use this formulation for the internal damping matrices.

It is noteworthy that the DoFs reordering and resizing must be performed for the bearings and unbalanced mass formulations in a similar manner.

2.3 Discs Modeling

The discs, when included into the CBT model, have a traditional formulation considering their kinetic energy in the Lagrange's equation while ignoring their elastic deformation energy. This yields a mass, a gyroscopic and a transient stiffening matrix, which are all applied at a particular node [35]. Considering the generalized DoFs of a CBT node, Equation 2.11:

$$q_D = \{u,\ w,\ \theta,\ \phi\}^T \tag{2.11}$$

one can then write the kinetic energy of the disc following a Lagrange formulation, as in Equation 2.12. A physical diagram of these assumptions are found in Figure 2.3.

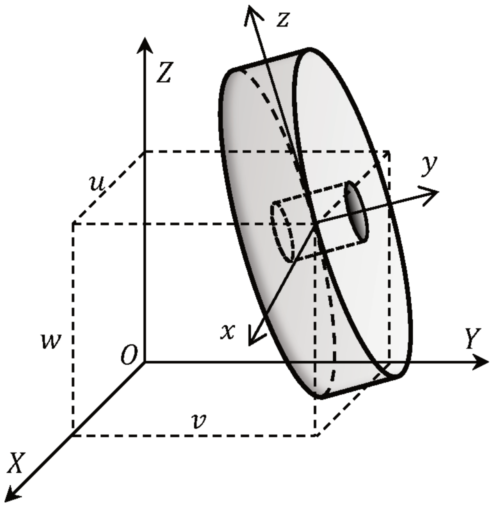

Figure 2.3: Disc dynamic model

$$T_D = \frac{1}{2}m_D\left(\dot{u}^2 + \dot{w}^2\right) + \frac{1}{2}\left(I_{Dx}\omega_x^2 + I_{Dy}\omega_y^2 + I_{Dz}\omega_z^2\right) \tag{2.12}$$

Here m_D is the disc mass, I_Di and ω_i, $i = x, y, z$, are the disc inertia and rotational speeds along the respective i directions. By assuming a symmetric disc with small rotation angles relative to the stationary position, Equation 2.12 can be further simplified into Equation 2.13. This form is distributed by the physical origin of its terms, which is indicated in the brackets under each of them.

$$T_D = \underbrace{\frac{1}{2}m_D\left(\dot{u}^2 + \dot{w}^2\right)}_{\text{Mass}} + \underbrace{\frac{1}{2}I_D\left(\dot{\theta}^2 + \dot{\phi}^2\right)}_{\text{Stiffening}} + \underbrace{\frac{1}{2}I_{Dy}\left(\Omega^2 + 2\Omega\dot{\phi}\theta\right)}_{\text{Gyroscopic}} \tag{2.13}$$

In this case, Ω is the shaft rotation speed. By applying this to a Lagrange formulation and isolating the yielded terms, one can produce the aforementioned matrices, presented in Equations 2.14 to 2.16.

$$\mathbf{M}_d = \begin{bmatrix} m_D & 0 & 0 & 0 \\ 0 & m_D & 0 & 0 \\ 0 & 0 & I_D & 0 \\ 0 & 0 & 0 & I_D \end{bmatrix} \tag{2.14}$$

$$\mathbf{D}_d = \Omega \begin{bmatrix} 0 & 0 & 0 & 0 \\ 0 & 0 & 0 & 0 \\ 0 & 0 & 0 & -I_{Dy} \\ 0 & 0 & I_{Dy} & 0 \end{bmatrix} \tag{2.15}$$

$$\mathbf{K}_{dt} = \dot{\Omega} \begin{bmatrix} 0 & 0 & 0 & 0 \\ 0 & 0 & 0 & 0 \\ 0 & 0 & 0 & 0 \\ 0 & 0 & I_{Dy} & 0 \end{bmatrix} \tag{2.16}$$

When considering the UF model however, more options are available. One can instead assemble the disc as a thick shaft element, considering the same shaft formulation, changing only the material and geometrical properties accordingly. In this case, the disc standard stiffness terms should be neglected to achieve a similar result as the one produced by the above formulation, in order to avoid unphysical localized stiffening. A clear difference is the higher order interpolation functions available by the UF and the gyroscopic, coriolis and stiffening effects already accounted for in the UF shaft formulation. This makes the implementation easier and more representative in the UF environment.

2.4 Unbalanced Masses

As for the unbalancing effects, it is possible to take into account the effect due to localized masses on the nodes. In both formulations considered, unbalanced masses are modeled by their kinectic energy only. It is assumed that the unbalanced mass effects act on the shaft cross section, with neither coupled directional terms on the axial direction nor rotations other than the one around the shaft itself. Therefore, all squared or non-linear terms resulting from the application of the Lagrange equation are neglected. The resulting forces are applied to x and z DoFs (Equation 2.17) on the nodes of the discs. The variables are presented in the Figure 2.4.

$$q_D = \{u,\ w\}^T \tag{2.17}$$

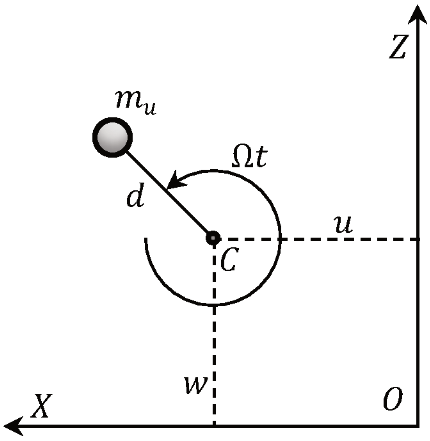

Figure 2.4: Unbalanced mass dynamic model

By developing the kinectic energy for a localized mass at a given radius, one can write Equation 2.18.

$$T_u = \frac{m_u}{2}\left(\dot{u}^2 + \dot{w}^2 + \Omega^2 d^2 + 2\Omega d\dot{u}\sin(\Omega t) - 2\Omega d^2 + 2\Omega d\dot{w}\sin(\Omega t)\right) \tag{2.18}$$

This mass influences the x and z directions only, meaning that the relevant generalized coordinates are u and w. The rotations are neglected from the equations and all constant and high-order terms are neglected. The resulting expression is given by Equation 2.19,

$$T_u \approx m_u \Omega d\big(\dot{u}\sin(\Omega t) - \dot{w}\cos(\Omega t)\big) \tag{2.19}$$

which in matrix form leads to the unbalanced forces vector as in Equation 2.20

$$\begin{Bmatrix} F_{unbx} \\ F_{unbz} \end{Bmatrix} = \begin{Bmatrix} -m_u d\dot{\Omega}\sin(\Omega t) - m_u d\Omega^2\cos(\Omega t) \\ -m_u d\dot{\Omega}\cos(\Omega t) + m_u d\Omega^2\sin(\Omega t) \end{Bmatrix} \tag{2.20}$$

Again, as in the previous cases, this vector needs to be expanded to the same size of the nodal matrices. This is done in order to assemble the system of equations automatically.

2.5 Bearing Modeling

Regarding the bearing supports, these are assumed to be radial only, with an elastic and a viscous damping components. A clear depiction of the physical model is given by Figure 2.5, similar to the one shown in [18].

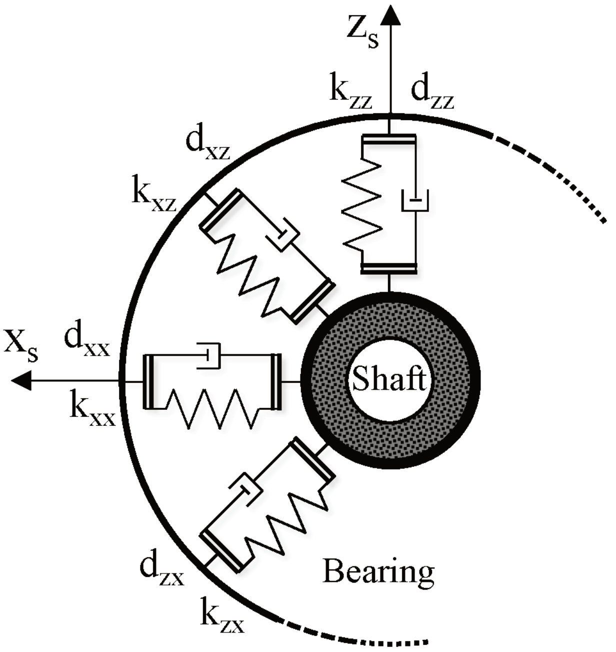

Figure 2.5: Bearings dynamic model representation

Mathematically, this is governed by the virtual work of the supporting forces, later yielding the bearing stiffness and damping matrices. By considering its effects on x and z directions only, the generalized coordinates vector is given by Equation 2.21.

$$q_D = \{u,\ w\}^T \tag{2.21}$$

By applying the principle of virtual forces on this system one obtains Equation 2.22, which can be further elaborated into a matrix form, as given by Equation 2.23.

$$\delta W = -k_{xx}u\delta u - k_{xz}w\delta u - k_{zx}u\delta w - k_{zz}w\delta w - d_{xx}\dot{u}\delta u - d_{xz}\dot{w}\delta u - d_{zx}\dot{u}\delta w - d_{zz}\dot{w}\delta w \tag{2.22}$$

$$\begin{Bmatrix} F_{bu} \\ F_{bw} \end{Bmatrix} = \begin{bmatrix} k_{xx} & k_{xz} \\ k_{zx} & k_{zz} \end{bmatrix} \begin{Bmatrix} u \\ w \end{Bmatrix} + \begin{bmatrix} c_{xx} & c_{xz} \\ c_{zx} & c_{zz} \end{bmatrix} \begin{Bmatrix} \dot{u} \\ \dot{w} \end{Bmatrix} \tag{2.23}$$

Similar to the previous systems, the bearings DoFs need to be expanded to the FEM model number of DoFs, filling the unused positions with zeroes. This two matrices are denominated as the bearing stiffness and damping matrices, respectively, and are either experimentally determined or optimized to adequate values via numerical procedures.

2.6 Onboard Dynamics

The onboard dynamics formulation is presented in the following through its condensed form, since it is applied to the CBT model only. Although it is possible to apply it on the UF model, the computational cost for its solution is prohibitively high to the current computational power available to the authors. Therefore, the formulation presented is the one introduced into the CBT model, which can be extended to the UF formulation, should the need arise.

Following the theory proposed by [24] and [25], three coordinate systems are defined to model the rotor base movement. A depiction of the system reference frames is given by Figure 2.6.

In this scheme, three coordinate systems are used to relate the stationary referential to the moving one attached to the FEM elements. R_0 is stationary referential, R_s is the

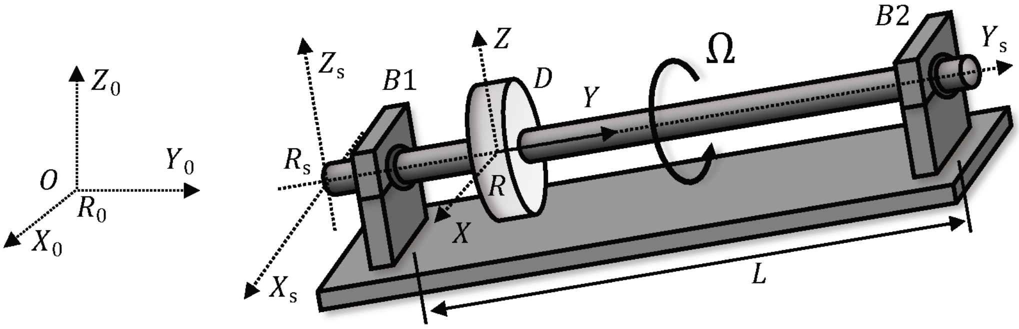

Figure 2.6: Onboard rotor coordinate systems (Adapted from [24])

one attached to the shaft origin and R is the reference frame linked to the elements. Starting from R, one determines a transfer matrix to R_s, followed by another one from R_s to R_0, as depicted in Figure 2.7.

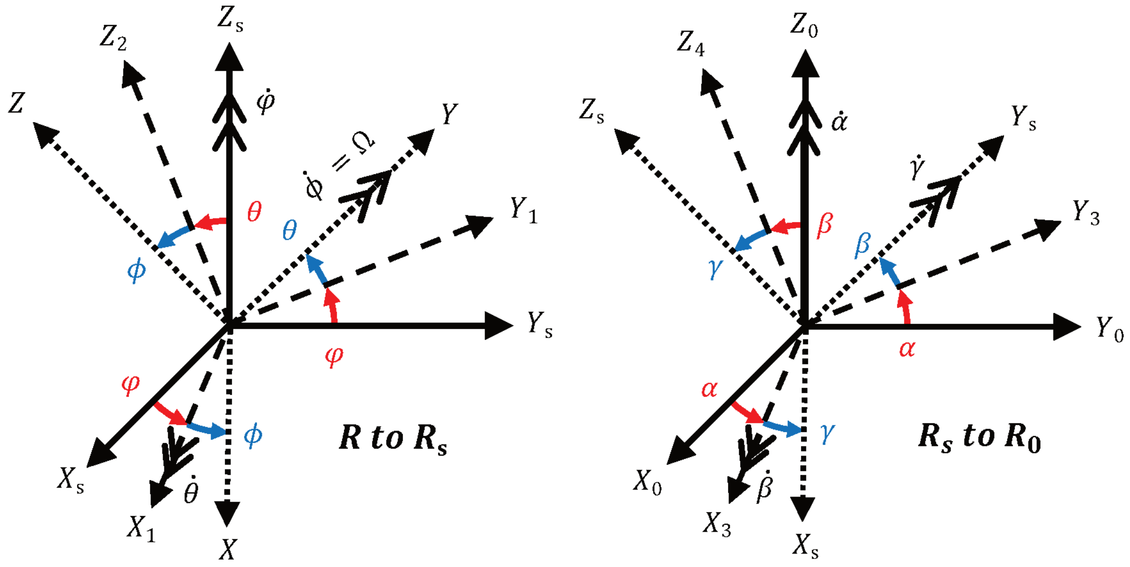

Figure 2.7: Coordinate transformations for the onboard rotor system. On the left: R to R_s, on the right: R_s to R_0. (Adapted from [54])

The result is a merged transfer function from the stationary system R_0 to the onboard moving system R, which is used to formulate the FEM problem. The condensed form of this problem is now presented, showing the transfer matrices themselves and the rotations required by the sequential transformations. For the intermediate steps of this formulation, please refer to the original work of [24] or to the preliminary formulation used on the CBT model presented here, as elaborated by [54].

One begins by expressing the angular velocity vector from R in relation to R_0 as given by Equation 2.24.

$$\overline{\Omega}_R^{R_0} = \begin{Bmatrix} (\dot{\alpha}_s \cos\psi + \dot{\beta}_s \sin\psi + \dot{\theta})\cos\phi - ((\dot{\alpha}_s \sin\psi - \dot{\beta}_s \cos\psi)\sin\theta + (\dot{\gamma}_s + \dot{\psi})\cos\theta)\sin\phi \\ -(\dot{\alpha}_s \sin\psi - \dot{\beta}_s \cos\psi)\cos\theta + (\dot{\gamma}_s + \dot{\psi})\sin\theta + \dot{\phi} \\ (\dot{\alpha}_s \cos\psi + \dot{\beta}_s \sin\psi + \dot{\theta})\sin\phi + ((\dot{\alpha}_s \sin\psi - \dot{\beta}_s \cos\psi)\sin\theta + (\dot{\gamma}_s + \dot{\psi})\cos\theta)\cos\phi \end{Bmatrix}_R \tag{2.24}$$

The definition of the position vector of R relative to O is given by Equation 2.25.

$$\overline{OC} = \begin{Bmatrix} [(x_A \cos\alpha + y_A \sin\alpha)\cos\gamma - (z_A \cos\beta + (x_A \sin\alpha - y_A \cos\alpha)\sin\beta)\sin\gamma] + u(y,t) \\ [z_A \sin\beta - (x_A \sin\alpha - y_A \cos\alpha)\cos\beta] + y \\ [(x_A \cos\alpha + y_A \sin\alpha)\sin\gamma + (z_A \cos\beta + (x_A \sin\alpha - y_A \cos\alpha)\sin\beta)\cos\gamma] + w(y,t) \end{Bmatrix}_{R_S} \tag{2.25}$$

The above coordinate transformations are then applied to the energy equations of the Lagrange formulation, altering the FEM models to account for the base displacement.

2.7 Unified Formulation

The UF utilized in the present work is based on the works of [16], [17] and [26], featuring a number of modifications and added functionalities described previously. By maintaining the interpolation order and element type as input parameters, the UF is not restricted to the limitations of standard FEM theories, making very accurate and easily adaptable structural models. The displacement field interpolation functions are also arbitrarily chosen, and no assumption for them is required beforehand. UF assemblies are made in different levels, starting at the Fundamental Nuclei (FN), then moving to the nodal level, later to the element level, and finally to the global stage. A schematic perspective of this procedure is shown in Figure 2.8.

2.7.1 CUF Shape and Interpolation Functions

The model construction begins by defining the nodal displacement vector as in Equation 2.26:

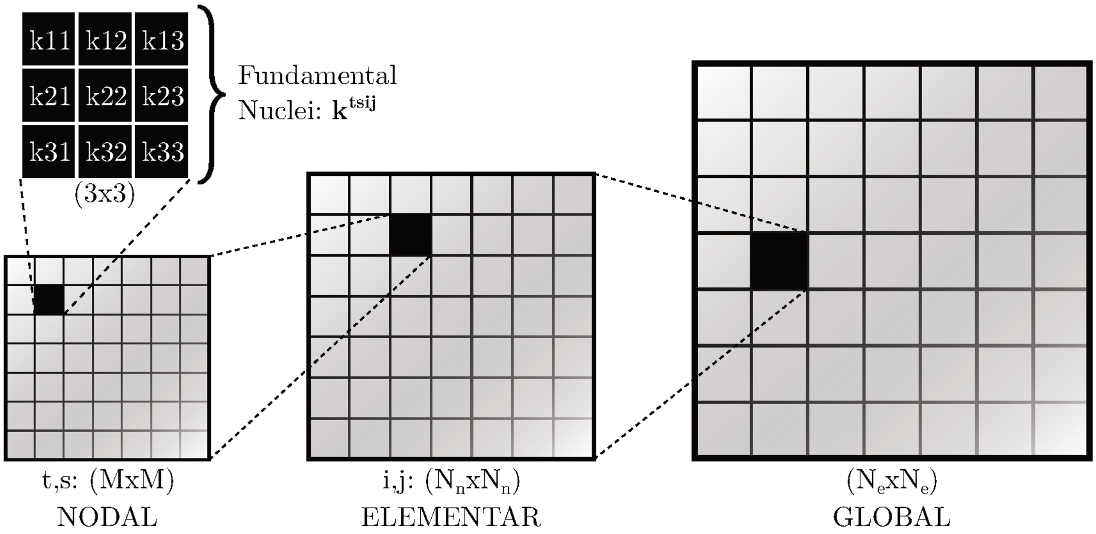

Figure 2.8: UF assembling procedure for a typical stiffness matrix (adapted from [63])

$$u(x,y,z) = \{u_x, u_y, u_z\}^T, \ where \ \ 0 \leqslant y \leqslant L \tag{2.26}$$

where L is the shaft length in the y direction and the x, z plane defines the cross-section geometry. Figure 2.9 presents a diagram illustrating these variables and the following shape functions.

Next, one can define the time dependent vector $u(x,y,z)$ as in Eq. (2.27):

$$u(x,y,z,t) = F_\tau(x,z)u_\tau(y,t), \quad \tau = 1,2,\cdots,N \tag{2.27}$$

expressing the cross-section interpolation by F_τ, Eq. (2.28), and the displacement vector is given by u_τ. The τ sub-index indicates Einstein summation notation. This yields the u_i $(i = x,y,z)$ terms of Eq. (2.29):

$$\begin{aligned}
0th\ order \Rightarrow F_1 = 1;\\
1st\ order \Rightarrow F_1 = 1;\ F_2 = x;\ F_3 = z;\\
2nd\ order \Rightarrow F_1 = 1;\ F_2 = x;\ F_3 = z;\ F_4 = x^2;\ F_5 = xz;\ F_6 = z^2;\\
3rd\ order \Rightarrow F_1 = 1;\ F_2 = x;\ F_3 = z;\ F_4 = x^2;\ F_5 = xz;\ F_6 = z^2;\\
F_7 = x^3;\ F_8 = x^2z;\ F_9 = xz^2;\ F_{10} = z^3;\\
\dots\\
Nth\ order \Rightarrow \{previous\ orders\}\ F_{(N^2+N+2)/2} = x^N;\ \{\cdots\};\ F_M = z^N.
\end{aligned} \tag{2.28}$$

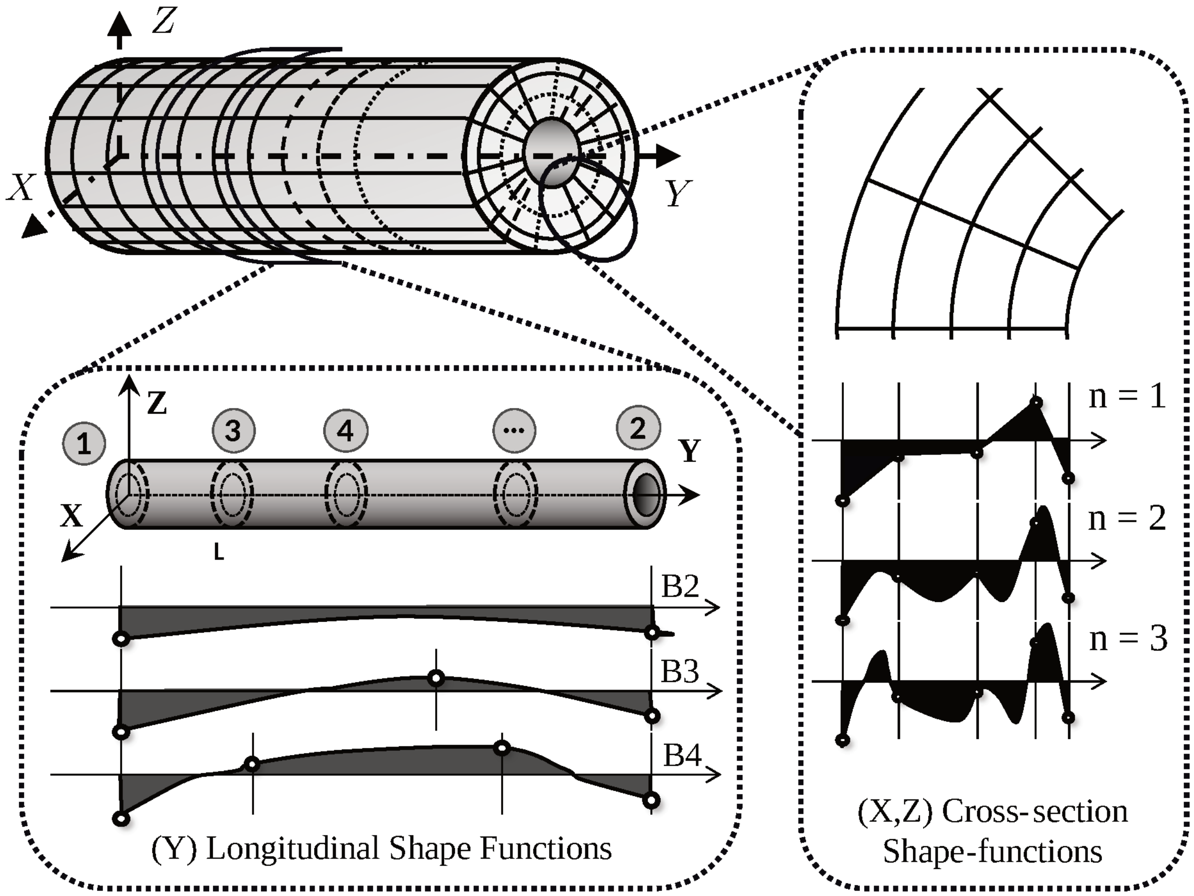

Figure 2.9: UF shaft model diagram. Circled in red, an *element* with its longitudinal interpolation, dependent on the number of *nodes per element*. In blue, the *element cross-section* stress field interpolation functions, dependent on the arbitrarily chosen polynomial order.

$$
\begin{aligned}
0th\ order &\Rightarrow u_i = F_1 u_{i1} \\
1st\ order &\Rightarrow u_i = F_1 u_{i1} + F_2 u_{i2} + F_3 u_{i3} \\
2nd\ order &\Rightarrow u_i = F_1 u_{i1} + F_2 u_{i2} + F_3 u_{i3} + F_4 u_{i4} + F_5 u_{i5} + F_6 u_{i6} \\
3rd\ order &\Rightarrow u_i = F_1 u_{i1} + F_2 u_{i2} + F_3 u_{i3} + F_4 u_{i4} + F_5 u_{i5} + F_6 u_{i6} + F_7 u_{i7} + \\
&\qquad + F_8 u_{i8} + F_9 u_{i9} + F_{10} u_{i10} \\
&\qquad \dots \\
Nth\ order &\Rightarrow u_i = \{previous\ orders\} + F_{(N^2+N+2)/2} u_{i(N+1)} + \cdots + F_M u_{iM}
\end{aligned}
\tag{2.29}
$$

where N is the interpolation order and M is the amount of generalized Degrees of Freedom (DoFs) per node, given by $M = (1/2)(N+1)(N+2)$. Making an analogy with the CBT, specifically regarding the Timoshenko model [64], u_{x1} and u_{z1} are equivalent to the translational DoFs x and z, while u_{y2} and u_{y3} correspond to the rotational DoFs θ and φ, respectively. Degenerating the UF into any classical model is a simple matter of eliminating selected terms in the formulation. For this Two-node Beam Element (B2), a simple interpolation is adopted in the longitudinal direction, such as explained by Eqs. (2.30) and (2.31). An expansion for third, fourth and higher orders is also possible, although not performed here, as presented by Eqs. (2.32) and (2.33). It is worth mentioning that these polynomials follow a Taylor-like expansion. However, Legendre-like and other polynomials are also usable.

$$u_{\tau}(y,t) = N_i(y)q_i(t),\ where\ \ q_i(t) = \{q_{ux\tau_i},\ q_{uy\tau_i},\ q_{uz\tau_i}\}^T,\ i = 1, \cdots, N_{nodes} \tag{2.30}$$

$$\begin{cases} N_1 = 1/2 * (1-r); \\ N_2 = 1/2 * (r+1); \\ r = \{-1,\ 1\}^T,\ for\ a\ B2\ element. \end{cases} \tag{2.31}$$

$$\begin{cases} N_1 = 1/2 * r * (1-r); \\ N_2 = 1/2 * r * (r+1); \\ N_3 = -(r+1) * (1-r); \\ r = \{-1,\ 1,\ 0\}^T,\ for\ a\ B3\ element. \end{cases} \tag{2.32}$$

$$\begin{cases} N_1 = -(9/16 * (r+1/3)) * (r+1/3) * (r-1); \\ N_2 = (9/16 * (r+1/3)) * (r+1/3) * (r-1); \\ N_3 = (27/16 * (r+1/3)) * (r+1/3) * (r-1); \\ N_4 = -(27/16 * (r+1/3)) * (r+1/3) * (r-1); \\ r = \{-1,\ 1,\ -1/3,\ 1/3\}^T,\ for\ a\ B4\ element. \end{cases} \tag{2.33}$$

As the number of nodes per element in the longitudinal direction increases, so the interpolation functions Ni increase both in number and complexity. An element with 3 nodes, named B3, would have a parabolic interpolation function, a B4 would be cubic and so on, while a simple B2 element has a linear interpolation. Although in this formulation no limitations have been imposed for the element order, the B2 elements are generally adequate for long shafts such as the ones considered in the present contribution, while higher order interpolations are recommended for thick-walls, flywheels or high diameter elements, depending on the problem dynamics [17]. By making use of high order elements, shell deformations and vibration modes are visible in the case of thin walled hollow shafts. These effects start to appear with B4 beam elements, and improve in precision by using even higher orders, allowing for obtaining accurate shell-like deformation results at a low cost, when compared to a full shell FEM model.

This UF framework has another advantage regarding Layer-wise formulations. If needed, an extra iterative loop can be introduced to the formulation instead of the SHBT equivalent layer approach. In this scenario, each layer should be considered as an independent shaft, which would yield associated global matrices that are then merged into a single equivalent matrix. While this procedure leads to more accurate results than equivalent layer approaches [63], it is nevertheless more costly and often unnecessary. When treating very thick walled composite sections, where accuracy is essential, this approach is recommended, while for most slender shafts an equivalent layer approach is sufficient. As a guideline, the Layer-wise approach should be used if accurate interlaminar shear strees calculations or delamination estimations are needed.

2.7.2 CUF Fundamental Nuclei Assembly

The FEM matrix operations for the UF are made iteratively, favoring numerical implementation. Once the shape functions have been defined, one can integrate them to the order needed and assemble the FN in a generic manner. By implementing the formulation through this method, the interpolation order and the number of nodes per element are left as arbitrary parameters, allowing for great modeling flexibility.

Regarding the numerical procedure itself, the FN matrices are developed from the Lagrange formulation in a more general way, automating the standard FEM procedure. For this aim, the interpolation functions are pre-integrated, producing a number of different auxiliary variables. Consequently the integrals, commonly seen in the FEM matrices, are replaced by pre-integrated terms. The global matrices assembling procedure is made through a number of iterative loops, where they cover: a) the two *node* indexes (τ,s); b) the two *element* indexes (i,j); c) the last index, representing the number of elements in the system. A pseudo-code depiction of this method is given in Figures 2.8 and 2.10.

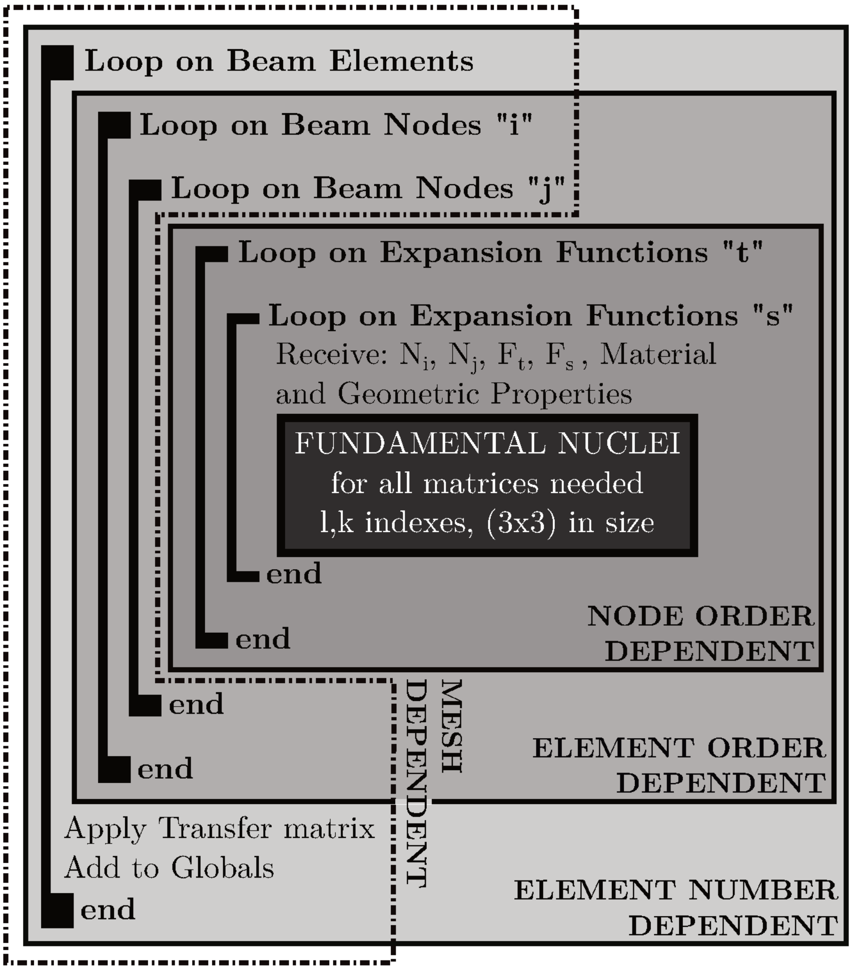

Figure 2.10: Numerical UF assembling procedure for the Fundamental Nuclei (FN) (adapted from [16])

Since the methodology has an arbitrary number of generalized DoFs and also arbitrary interpolation functions, an automated determination of the connectivity and node location matrices is necessary. Therefore, the location matrix gives the physical coordinates for each element node, where the element is identified by the array line number and the geometrical coordinates are explicitly given by the columns, one for each analogue node. This number of nodes per element is given by the first UF arbitrary variable, defining elements such as *B2*, with 2 nodes, *B3* with 3 nodes, and so on. This choice sets the framework for further developments, as demonstrated by Figure 2.11 for a simple model with 2 elements and different number of nodes per element. A suggested assembling rule for this matrices is given in [16], although different standards are also viable.

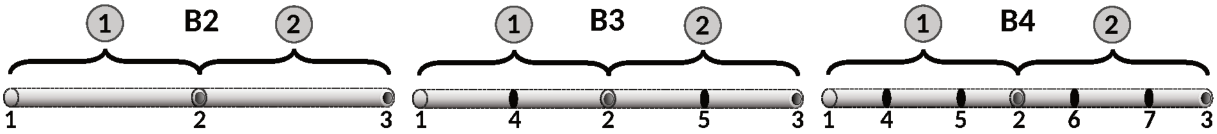

Figure 2.11: UF node and element numbering depending on the selected order of the model

As a side-note, the global number of DoFs is given by: $DoF_{total} = (DoFs\ per\ node) * [((nodes\ per\ element) - 1) * (number\ of\ elements) + 1]$. Moving on to the FN equations, they are developed from a Lagrange formulation in the generalized form. Initially, one determines the potential and kinetic energies for the shaft, discs, bearings, etc., and apply the principle of virtual work on the external forces and unbalanced masses. This procedure leads to the *Principle of Virtual Displacements* (PVD) equations for the necessary FEM matrices in the UF framework. For illustration purposes, this procedure is presented for the stiffness matrix, as in Equations (2.34) and (2.35), and is analogously repeated for the other matrices.

$$\delta L_{int} = \int_V (\delta \varepsilon_p^T \sigma_p + \delta \varepsilon_n^T \sigma_n) dV = \delta L_{ext} \tag{2.34}$$

$$\delta L_{int} = \delta \mathbf{q}_{\tau i}^T \, \mathbf{K}^{ij\tau s} \mathbf{q}_{sj} \tag{2.35}$$

The individual terms for the stiffness matrix are presented in Equation (2.36), before the pre-integration of the shape and interpolation functions as described below.

$$K_{xx}^{ij\tau s} = \tilde{C}_{22} \int_\Omega F_{\tau,x} F_{s,x} d\Omega \int_l N_i N_j dy + \tilde{C}_{66} \int_\Omega F_{\tau,z} F_{s,z} d\Omega \int_l N_i N_j dy +$$
$$\tilde{C}_{44} \int_\Omega F_\tau F_s d\Omega \int_l N_{i,y} N_{j,y} dy$$

$$K_{xy}^{ij\tau s} = \tilde{C}_{23} \int_\Omega F_{\tau,x} F_s d\Omega \int_l N_i N_{j,y} dy + \tilde{C}_{44} \int_\Omega F_\tau F_{s,x} d\Omega \int_l N_{i,y} N_j dy$$

$$K_{xz}^{ij\tau s} = \tilde{C}_{12} \int_\Omega F_{\tau,x} F_{s,z} d\Omega \int_l N_i N_j dy + \tilde{C}_{66} \int_\Omega F_{\tau,z} F_{s,x} d\Omega \int_l N_i N_j dy$$

$$K_{yx}^{ij\tau s} = \tilde{C}_{44} \int_\Omega F_{\tau,x} F_s d\Omega \int_l N_i N_{j,y} dy + \tilde{C}_{23} \int_\Omega F_\tau F_{s,x} d\Omega \int_l N_{i,y} N_j dy$$

$$K_{yy}^{ij\tau s} = \tilde{C}_{55}\int_\Omega F_{\tau,z}F_{s,z}d\Omega\int_l N_iN_jdy + \tilde{C}_{44}\int_\Omega F_{\tau,x}F_{s,x}d\Omega\int_l N_iN_jdy + \tilde{C}_{33}\int_\Omega F_\tau F_sd\Omega\int_l N_{i,y}N_{j,y}dy$$

$$K_{yz}^{ij\tau s} = \tilde{C}_{55}\int_\Omega F_{\tau,z}F_sd\Omega\int_l N_iN_{j,y}dy + \tilde{C}_{13}\int_\Omega F_\tau F_{s,z}d\Omega\int_l N_{i,y}N_jdy$$

$$K_{zx}^{ij\tau s} = \tilde{C}_{12}\int_\Omega F_{\tau,z}F_{s,x}d\Omega\int_l N_iN_jdy + \tilde{C}_{66}\int_\Omega F_{\tau,x}F_{s,z}d\Omega\int_l N_iN_jdy$$

$$K_{zy}^{ij\tau s} = \tilde{C}_{13}\int_\Omega F_{\tau,z}F_sd\Omega\int_l N_iN_{j,y}dy + \tilde{C}_{55}\int_\Omega F_\tau F_{s,z}d\Omega\int_l N_{i,y}N_jdy$$

$$K_{zz}^{ij\tau s} = \tilde{C}_{11}\int_\Omega F_{\tau,z}F_{s,z}d\Omega\int_l N_iN_jdy + \tilde{C}_{66}\int_\Omega F_{\tau,x}F_{s,x}d\Omega\int_l N_iN_jdy + \tilde{C}_{55}\int_\Omega F_\tau F_sd\Omega\int_l N_{i,y}N_{j,y}dy \tag{2.36}$$

It is worth mentioning that the integral terms in the FN can be pre-integrated in order to facilitate and optimize the coding. The solution of these terms can be made either numerically or via symbolic programming, with both having advantages and drawbacks. By solving numerically, the clear advantage is a much faster computational time, at the price of either: a) introducing the numerical values into the equations early in the formulation and losing flexibility or; b) pre-calculating every relevant case and storing them in a database. However, one can use a symbolic approach, which has a higher computational cost, but provides a didactic understanding of the physical phenomena involved in the dynamics of the system. Since this research is a scientific contribution to the understanding of rotordynamics, the analytic approach was adopted.

Moving on to the dynamic stiffening matrix, its individual terms are presented in Equation (2.37), before the pre-integration of the shape and interpolation functions, as described below. From the formulation of the composite material, one determines that this pre-stiffening is dependent on the squared rotation speed Ω^2.

$$Ko_{xx}^{ij\tau s} = -\Omega^2\rho\int_\Omega F_\tau F_sd\Omega\int_l N_iN_jdy$$

$$Ko_{xy}^{ij\tau s} = Ko_{xz}^{ij\tau s} = Ko_{yx}^{ij\tau s} = Ko_{yy}^{ij\tau s} = Ko_{yz}^{ij\tau s} = Ko_{zx}^{ij\tau s} = Ko_{zy}^{ij\tau s} = 0$$

$$Ko_{zz}^{ij\tau s} = \Omega^2\rho \int_\Omega F_\tau F_s d\Omega \int_l N_i N_j dy$$

(2.37)

An additional pre-stress stiffness matrix, originated from any form of internal stresses in the material, such as thermal and manufacturing stresses, is introduced. In this work it is left null, although the procedure was implemented in the algorithm.

The next FN term is the gyroscopic matrix, whose individual terms are given by Equation (2.38). These terms are linearly dependent on the rotation speed.

$$G_{xx}^{ij\tau s} = G_{xy}^{ij\tau s} = 0$$

$$G_{xz}^{ij\tau s} = -2\Omega\rho \int_\Omega F_\tau F_s d\Omega \int_l N_i N_j dy$$

$$G_{yx}^{ij\tau s} = G_{yy}^{ij\tau s} = G_{yz}^{ij\tau s} = 0$$

$$G_{zx}^{ij\tau s} = 2\Omega\rho \int_\Omega F_\tau F_s d\Omega \int_l N_i N_j dy$$

$$G_{zy}^{ij\tau s} = G_{zz}^{ij\tau s} = 0$$

(2.38)

The final UF FN term is the mass matrix, given by Equation (2.39). This is a very standard matrix, with a full main diagonal with the other terms being zeroes..

$$M_{xx}^{ij\tau s} = \rho \int_\Omega F_\tau F_s d\Omega \int_l N_i N_j dy$$

$$M_{xy}^{ij\tau s} = M_{xz}^{ij\tau s} = M_{yx}^{ij\tau s} = 0$$

$$M_{yy}^{ij\tau s} = \rho \int_\Omega F_\tau F_s d\Omega \int_l N_i N_j dy$$

$$M_{yz}^{ij\tau s} = M_{zx}^{ij\tau s} = M_{zy}^{ij\tau s} = 0$$

$$M_{zz}^{ij\tau s} = \rho \int_\Omega F_\tau F_s d\Omega \int_l N_i N_j dy$$

(2.39)

The second member of the Equation of Motion (EoM), namely the vector of external applied forces is provided by Equation (2.40).

$$F_{ext}^{p\alpha\beta} = \rho\Omega^2 \int_\Omega F_\tau d\Omega \int_l N_i dy$$

$$F_{ext}^{p\alpha\beta} = 0$$

$$F_{ext}^{p\alpha\beta} = -\rho\Omega^2 \int_\Omega F_\tau d\Omega \int_l N_i dy$$

(2.40)

2.7.3 CUF Order Choice and Best Theory Determination

The order of the UF model chosen for the representation of the rotor systems considered in this work is of major importance. As an analogy, CBT models such Euler-Bernoulli's are equivalent to a simplified 0_{th} order UF model, while a Timoshenko's is equivalent to a 1_{st} order UF model. To properly represent a thick-walled composite shaft or Flywheel Energy Storage Systems (FESS), a higher order model is needed. This necessity depends on the mode shapes analysed, the amplitude of shear stresses and laminated composite complexity and symmetry. As presented in the results section of this dissertation, a second order model is sufficiently accurate to predict the dynamics of the thick-walled shafts studied here. By comparison, a third order model is hardly necessary to analyze the dynamic response of most engineering shafts. Should the system be made out of composite materials and/or have extremely thick walls, such as in a FESS, higher order models are recommended to represent detailed deformation and wrinkling of these elements walls. Nevertheless, the "rigid body" modes and rough shape deformations of even FESS systems are still properly perceived and modeled by second and third order UF models. A description of the cross-section strain distribution depending on the interpolation model order (N) is given by Table 2.1, for the sake of clarity.

Another interesting feature enabled by the UF is the determination of a *best theory* [17] for each given application. When modeling via UF, one uses arrays of generalized coordinates and shape functions. Here, the individual terms can be enabled or disabled

	ε_{xx}	ε_{yy}	ε_{zz}	ε_{xy}	ε_{xz}	ε_{yz}
Euler-Bernoulli	0^*	1_{st}	0^*	0	0	0
Timoshenko.	0^*	1_{st}	0^*	cte	0	cte
UF N_1	cte*	1_{st}	cte*	1_{st}	cte	1_{st}
UF N_2	1_{st}	2_{nd}	1_{st}	2_{nd}	1_{st}	2_{nd}
UF N_3	2_{nd}	3_{rd}	2_{nd}	3_{rd}	2_{nd}	3_{rd}
⋮	⋮	⋮	⋮	⋮	⋮	⋮
UF N_n	*N-1*	*N*	*N-1*	*N*	*N-1*	*N*

Table 2.1: Order of the strain distribution representation for the shaft cross-section, depending on the model order. (*) terms indicate that the formulation is susceptible to Poisson locking, requiring correction terms to be added. The number of nodes per element is independent of this cross-section interpolation order. Adapted from [16].

arbitrarily, therefore modifying the physical representation of the problem conveyed. This feature is remarkably useful in situations where the physics of a problem is not fully understood. One may begin modeling with a high order UF model, gradually reducing its order via *best theory* application, until the minimum representative model - the "*best*" one - is determined. Taking the second order B2 model as an example, one can obtain Equation (2.41).

$$\begin{cases} u_x = u_{x1} + xu_{x2} + zu_{x3} + x^2u_{x4} + xzu_{x5} + z^2u_{x6} \\ u_y = u_{y1} + xu_{y2} + zu_{y3} + x^2u_{y4} + xzu_{y5} + z^2u_{y6} \\ u_z = \underbrace{u_{z1}}_{\text{N=0}} + \underbrace{xu_{z2} + zu_{z3}}_{\text{N=1}} + \underbrace{x^2u_{z4} + xzu_{z5} + z^2u_{z6}}_{\text{N=2}} \end{cases} \tag{2.41}$$

From this stage of the formulation, one can determine a Boolean matrix and apply the *Axiomatic approach*, as introduced by [16]. This methodology consists of a few stages, as proposed by the original UF author:

a) The problem is set and defined;
b) A relevant output is chosen as a reference (*i.e.* cross-section stresses, vibration amplitude, natural frequency values, etc.);
c) The problem is solved and the relevant output is obtained for the complete case,

which is used as a baseline;

d) Each of the shape function terms are then deactivated, one at a time, and the responses are compared to the baseline;

e) Terms that do not change the chosen response significantly are discarded, leaving only the relevant ones;

f) The final model, containing only relevant variables, is selected as the *best theory* formulation.

It is worth remembering that this *best theory* model is developed for the selected response of the problem, and therefore might be unreliable when analyzing different outputs. As an example, when modeling a slender shaft with a B2 second order UF theory one may utilize the following Boolean matrix to achieve an adequate theory, as given by Table 2.2

0_{th}	1_{st}		2_{nd}		
1	1	1	0	0	0
1	1	1	1	1	1
1	1	1	0	0	0

Table 2.2: Boolean matrix to apply an example theory to a second order B2 UF model, where the "$1's$" terms correspond to relevant terms, and 0 to the irrelevant ones. In the formulation of the problem, this matrix should multiply the one given by Equation (2.41) in matrix form, nullifying a number of unnecessary terms for a given application.

The material presented above is an useful tool for optimizing the algorithm processing speed, while keeping the formulation phisically representative. In this research effort the "full" formulations will be used, mainly the 2_{nd} order B2 UF model.

2.8 Equation of Motion

After the assembling of global matrices for stiffness, gyroscopic effect, damping and mass, with their shaft, disc, bearing and orthotropic material additions, the system EoM can be obtained. This is presented in the following with the individual matrices split according to their physical origin, as in Equation (2.42):

$$[\mathbf{M}+\mathbf{M_d}]\ddot{q}+[\mathbf{C}+\mathbf{C_b}+\Omega(\mathbf{G}+\mathbf{G_d})]\dot{q}+[\mathbf{K}+\mathbf{K_b}+\mathbf{K_d}+\mathbf{Ks}+\mathbf{Ks_d}+\Omega^2(\mathbf{Ko}+\mathbf{Ko_d})+\mathbf{Kt}]q=\mathbf{W}+\mathbf{F_{unb}} \tag{2.42}$$

The individual matrices presented below.

$\mathbf{M}$	Shaft standard mass matrix;
$\mathbf{M_d}$	Discs mass matrix;
$\mathbf{C}$	Shaft Kelvin-Voight damping matrix;
$\mathbf{C_b}$	Bearings damping matrix;
$\mathbf{G}$	Shaft gyroscopic effect matrix;
$\mathbf{G_d}$	Discs gyroscopic effect matrix;
$\mathbf{K}$	Shaft standard (or composite) stiffness matrix;
$\mathbf{K_b}$	Bearings stiffness matrix;
$\mathbf{K_d}$	Discs stiffness matrix;
$\mathbf{Ks}$	Shaft dynamic stiffening matrix;
$\mathbf{Ks_d}$	Disc dynamic stiffening matrix;
$\mathbf{Ko}$	Shaft centrifugal stiffening matrix;
$\mathbf{Ko_d}$	Disc centrifugal stiffening matrix;
$\mathbf{Kt}$	Shaft additional stiffness due to torque;
$\mathbf{W}$	System weight forces;
$\mathbf{F_{unb}}$	Unbalanced masses forces.

During the algorithm implementation, these matrices may be constructed either didactly as individual terms, such as made here, or grouped together for a slight increase on the evaluation speed.

Chapter 3

Experimental Procedures

In this section, the various designs of the test-rigs developed for the present dissertation are presented. Their mechanical design and electrical diagram with Data Acquisition Systems (DAQS) are displayed in detailed in the annex documents, while the overall geometries are depicted in the main text, in the following. The experimental procedures are described and the tests performed are also explained.

3.1 Experiments Layout

This dissertation included the design, manufacture and experimentation of three different experimental test-rigs, each one designed to test and validate specific parts of the formulation developed.

Initially, a test-rig was produced in partnership with a Master's Thesis [54], and targeted the onboard dynamics model physics. It included a bi-supported rotor, with two self-aligning ball bearings and a heavy disc at 1/3 of the shaft length. This whole system was assembled on top of a shaker table, which was then excited to different degrees and displacements, producing interesting onboard experimental data.

The second experimental setup developed was made in parallel with another Master's research [2], and aimed at studying the composite shaft dynamics. A secondary goal of this model was to include shear stresses and dynamic stiffening on the model. This rotor design includes two self-aligning ball bearings and two mettalic discs, in an overhung configuration. The shaft itself is a carbon-epoxy composite beam, with twenty layers of pre-impregnated fibers of a proprietary material. Both this one and the first test-rig have two proximity probes mounted in each disc, one being mounted along the *x* direction and another in the *z* direction, always perpendicular to the shaft.

Lastly, a flywheel design was developed and manufactured, upon which the UF theory was tested and validated. This system is also mounted on two self-aligning ball bearings, having a Polycarbonate (PC) flywheel attached to it. The proximity probes used on this system are reflective laser sensors, applied to the *x* and *z* directions close to the flywheel free open end, and a third sensor is mounted on the flywheel backplate, measuring the *y* direction displacement.

3.2 Metallic Onboard Test-Rig

The first experimental setup, designed as an onboard rotor, aim at the experimental representation of onboard dynamics and its interaction with the dynamics of the rotor. It represents the loads and efforts to which aircraft turbines, onboard compressors, pumps and any other moving-base rotor is subjected to, having a number of industrial analogues. Its conception focus on design simplicity, while clearly representing the onboard dynamics phenomena to validate the models.

3.2.1 Mechanical Design

The mechanical assembly of this rotor consists on two self-aligning ball bearing supports, holding a simple AISI 1040 steel shaft with an AISI 1020 steel disc mounted on it. The motor is positioned on a separate finned base, made of 3D-printed Acrylonitrile Butadiene Styrene (ABS) plastic, in order to keep it cool and isolated from the rotor dynamics. Both shafts are linked by an aluminium mechanical coupling, effectively transmitting torque and isolating other forces. As previously stated, the disc has two induction proximity probes mounted on the *x* and *z* directions, which are assembled on an aluminium ring mount around the disc. This encircling structure doubles as a sensor mount and safety device, both to protect the sensor heads and to avoid damage in the event of a sudden shaft fracture. The rotor system design is presented in Figure 3.1, with its identified components. A second depiction, featuring a longitudinal cut of the assembled system, presents also the dimensions of relevant components, and can be seen at Figure 3.2.

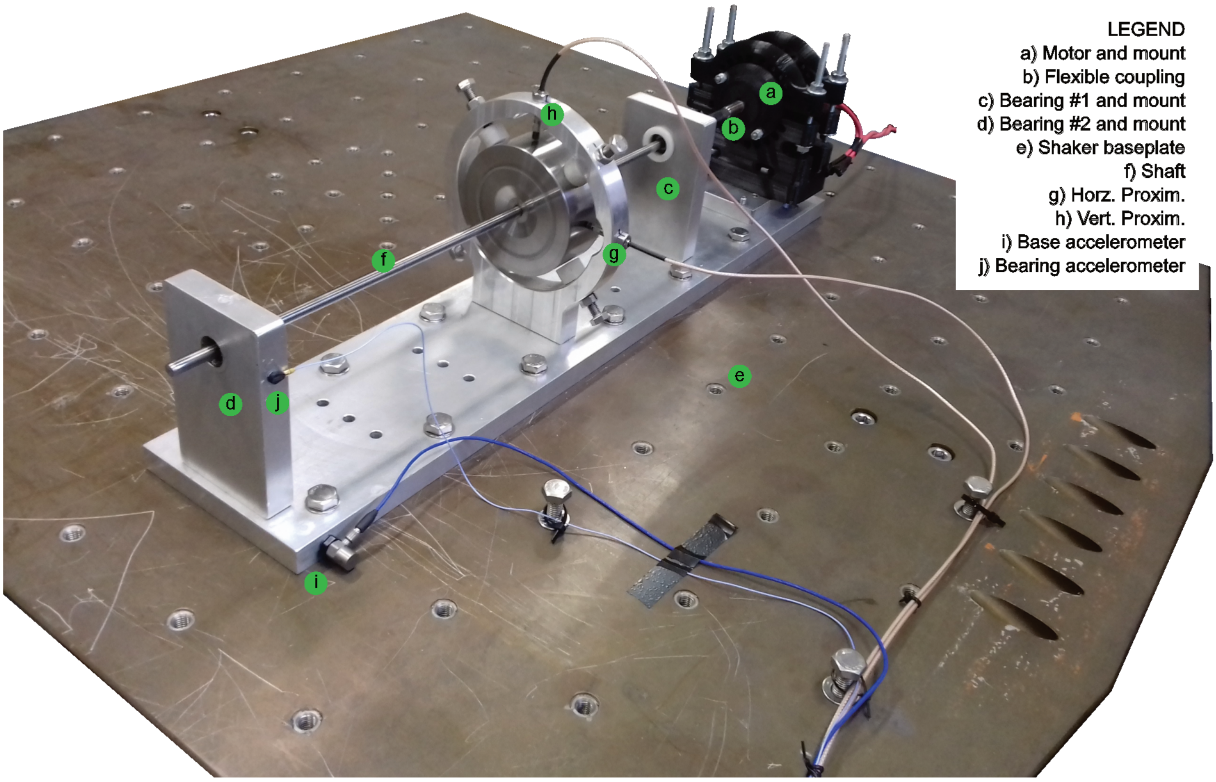

Figure 3.1: Onboard rotor test-rig mechanical system, with its indicated elements

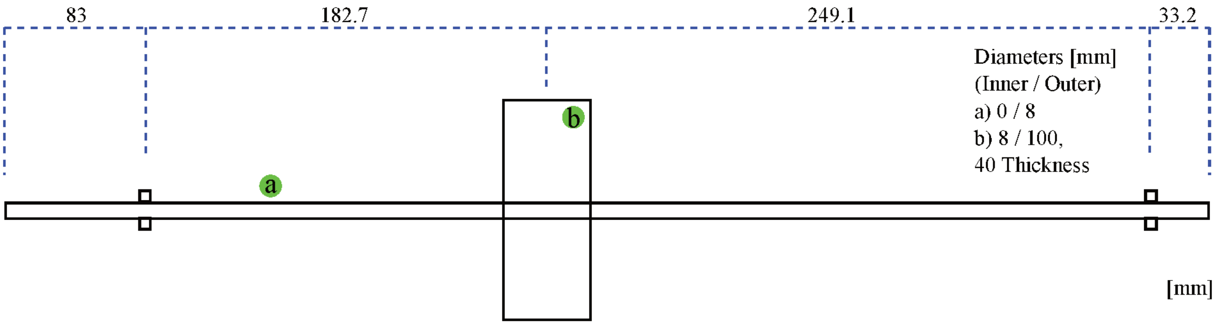

Figure 3.2: Onboard rotor test-rig scheme, detailing the cross-section dimensions. The motor and coupling are positioned the left hand side of the diagram, and the shaft has an overall length of 548 mm

3.2.2 Electronics and Sensors

The DAQ system developed for this rotor includes a pair of proximity probes on the disk cross-section, as well as two accelerometers, one being mounted on the shaker base and another on the bearings mount, leveled with the bearing, both along the x direction. The first accelerometer is used to close the shaker control loop, while the second one determines if the bearing mount suffers from any displacement relative to the base movement, which would affect the onboard dynamics. All data acquired from the accelerometers was sent via feedback loop to the shaker controller and to the DAQ System (signal analyzer model Agilent 35670A). The proximeters data is transmitted to the amplifiers and later to the signal analyzer, where it is processed and stored. Rotating speed data and monitoring was made through a handheld laser tachometer, ensuring the speed stability during the experimentation time.

3.2.3 Experiments Performed

A number of experimental procedures were performed on this system, acquiring useful model validation data from the proximeters. A checking for discrepancies is made by comparing the acceleration signal from two accelerometers, one in the shaker base and another in a bearing mounting structure. FRFs were obtained by applying hammer impacts on the shaft and acquiring data from the accelerometers installed close to the disc. Regarding operating analysis, the system was tested at 900 and 1600 RPM, with and without base excitation. Different displacement signals were applied by the shaker table, such as sinusoidal waves, impacts with varying amplitudes and experimentally obtained flight displacement data. A complete experimental design description can be found at the correlated research [54], while only the results relevant to the present study will be further discussed here.

3.3 Composite Shaft Test-Rig

An experimental design aimed at validating the composite rotor formulation, as well as the intrinsic material damping and shear stresses was approached with this second test-rig. It features a composite material shaft, with twenty layers of pre-impregnated carbon-epoxy, with a [0 0 0 0 90 90 45 -45 0 0 0 45 -45 90 90 0 0 0 0 0/90] degrees stacking sequence, from inner to outer layers. As for the other test-rigs, this system is also supported by two self-aligning ball bearings, this time mounted on conical sleeves with locking nuts. It also features two aluminium discs and coupling.

3.3.1 Mechanical Design

The objective of this test-rig was to obtain experimental data for thick-walled composite shafts, subjected to dynamic loads and possessing considerable internal damping. Therefore, it features a configuration that favors high loads and dynamic stresses, presenting a thick-walled (32% wall to radius ratio) composite shaft. Another interesting characteristic is the high asymmetry of the bearings, due to the mechanical design of the supporting structure where the bearings are mounted upon. The overhung configuration favors high loads along the shaft, due to an amplification of any misalignment, shaft warping or unbalanced masses influences. The mechanical assembly and its main dimensions are presented by Figures 3.3 and 3.4, respectively.

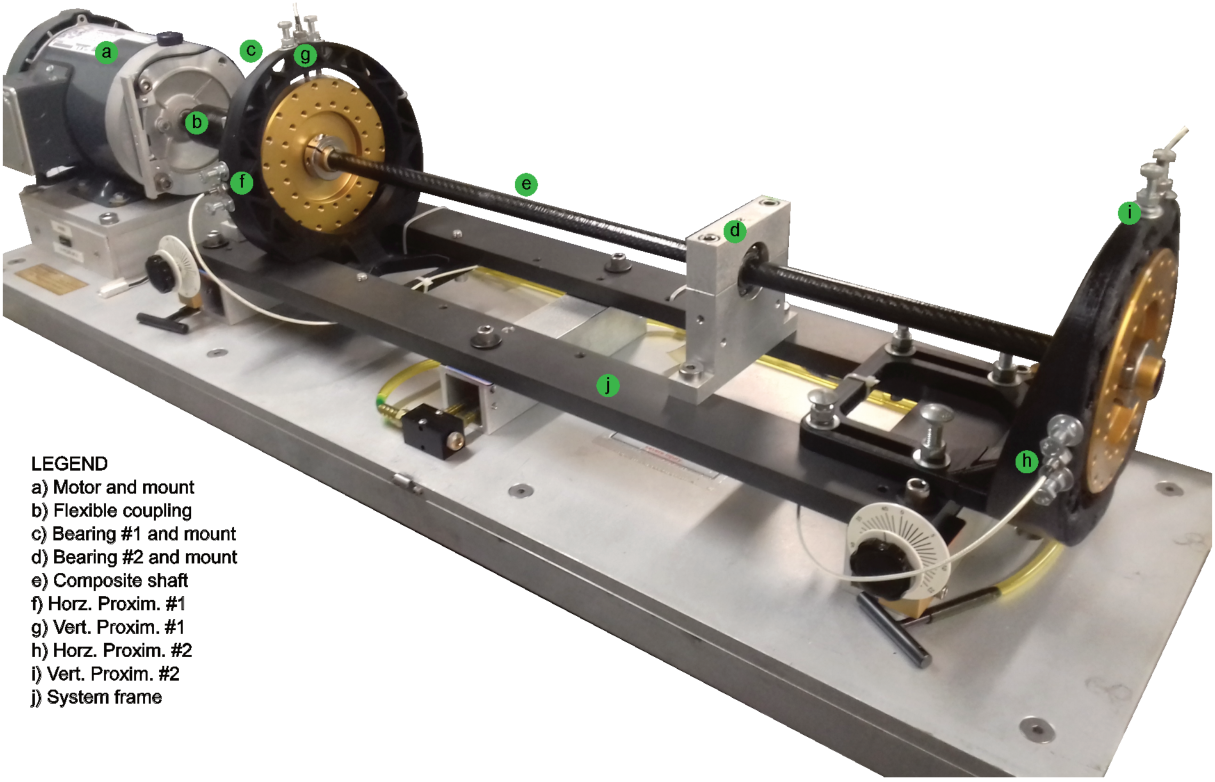

Figure 3.3: Composite rotor test-rig mechanical design overview, with indicated elements

3.3.2 Electronics and Sensors

This experimental setup counts with two pairs of induction proximity probes, mounted on each disc along the *x* and *z* directions. The drive motor assembly features a digital

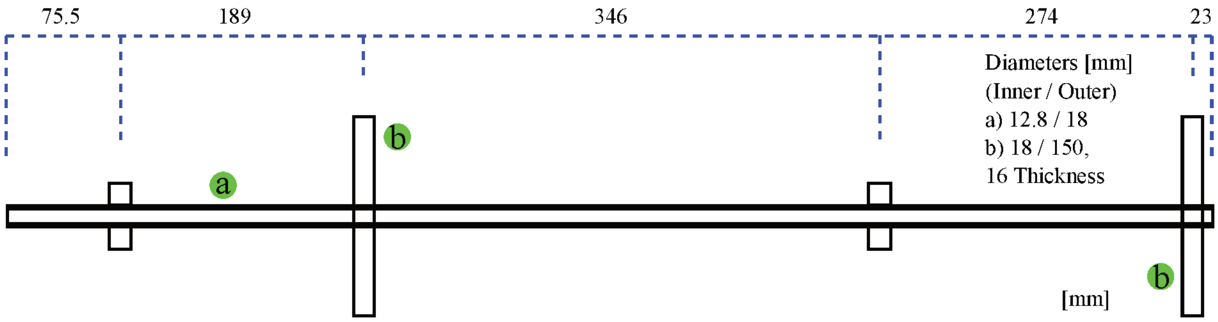

Figure 3.4: Composite rotor test-rig scheme, detailing the cross-section dimensions. The motor and coupling are positioned on the left hand side of the diagram, and the shaft has an overall length of 907 mm

speed control and a laser tachometer, mounted on the motor shaft, which constantly measures and regulates the system speed via feedback loop. The DAQ system used on the proximity probes is the same used on the previous test-rig, consisting of amplifier units for each sensor and a signal analyzer. Micro accelerometers available also provided additional information on the natural frequencies.

3.3.3 Experiments Performed

Both theoretically and experimentally, the system was analyzed using modal analysis techniques. In this way, it was possible to determine the dynamic behavior of the system. Experimental modal analysis was performed by using accelerometers and a force transducer mounted upon an impact hammer, with all data acquisition being handled by the signal analyzer. Similarly, using this instrumentation paired with the proximeters, running experiments were made at different speeds. Time signals were acquired and order analyses were performed, determining the rotor orbits at the discs positions.

3.4 Flywheel Dynamics Test-Rig

Finally, a flywheel rotor system was manufactured and tested. This system most evident element is a PC plastic flywheel mounted on a steel shaft. The purpose of this setup is to obtain experimental data on flywheel-shaft dynamic interaction and on membrane vibration modes of thin high radius cylindrical walls. An additional functionality that was explored on this design is the operation of the system on the vertical direction, which considerably modifies the dynamic behavior of the system.

3.4.1 Mechanical Design

The present system consists of a thin AISI 4340 steel shaft, supported by a couple of self aliginig ball bearings mounted on conical sleeves. The flywheel itself is positioned on a custom cylindrical mounting sleeve, kept in place by a locking washer and nut. Torque is produced by an electrical motor and transmitted by a low stiffness "*bellows-type*" mechanical coupling. The system and its technical drawing are presented on Figures 3.5 and 3.6. Since this test-rig is self-supported, not being mechanically clamped to an inertial base as the others, its base must be relatively rigid and considerably heavier than the moving parts. As a noise reduction and mechanical insulating measure, a rubber mattress is placed under the test-rig. Also, as vertical operation is required, specialized axial reinforcements were designed and applied to the bearing pillows. A structural reinforcement and safety structure encircles the flywheel, thus allowing for precise sensor positioning.

As can be seen in the rotor blueprint, the flywheel is composed of three individual parts: a) one being a bottom piece similar to a disc, linking the shaft coupling to the outer wall; b) the second being the flywheel cylindrical body itself, manufactured by extrusion with tight dimension tolerances; c) and the third is a reinforcement ring, mounted on the open end. These parts were assembled with nylon bolts, maintaining a similar stiffness and symmetric mass distribution on all the components. A technical blueprint for the flywheel test-rig with identified external components is found at Appendix A.

3.4.2 Electronics and Sensors

As the centerpiece of this setup is polymeric, and consequently not adequate for inductive proximity sensors, alternate sensing methods were considered. Given the vibration amplitude and relatively high surface speed estimated for the measuring regions, reflective laser position sensors were chosen as a viable option. OMROM^{TM}

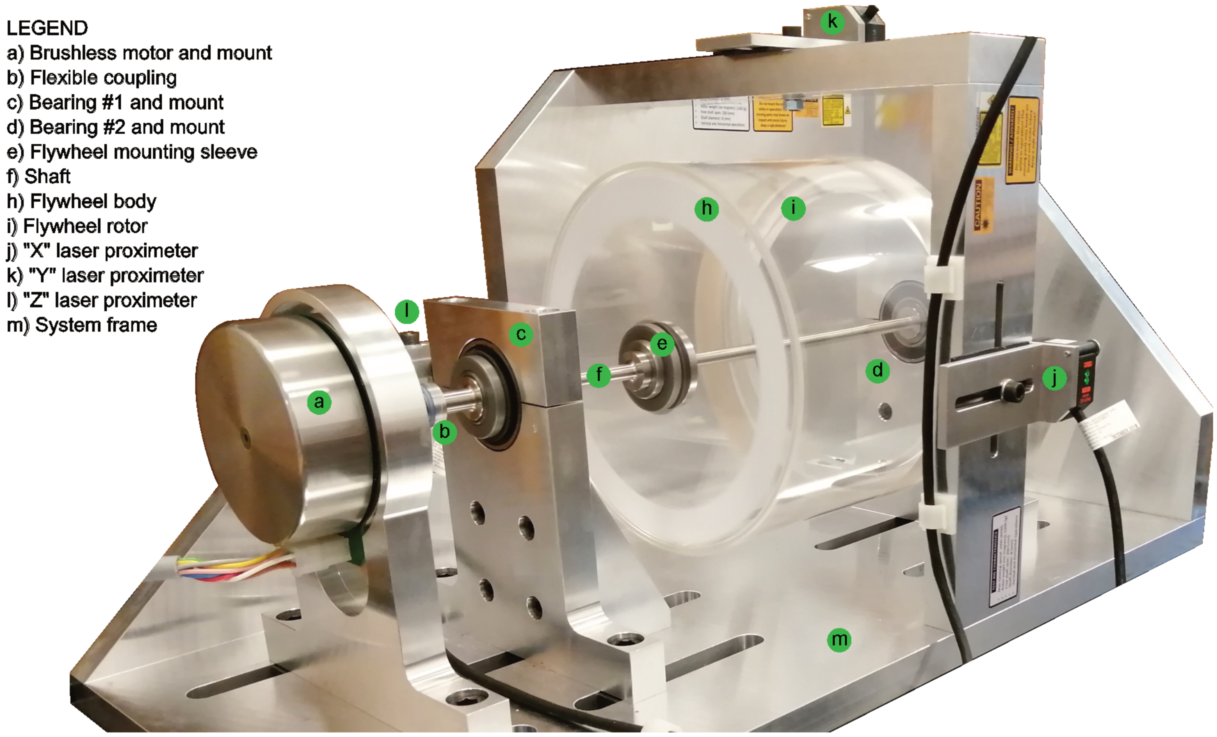

Figure 3.5: Flywheel test-rig mechanical design overview, with indicated elements

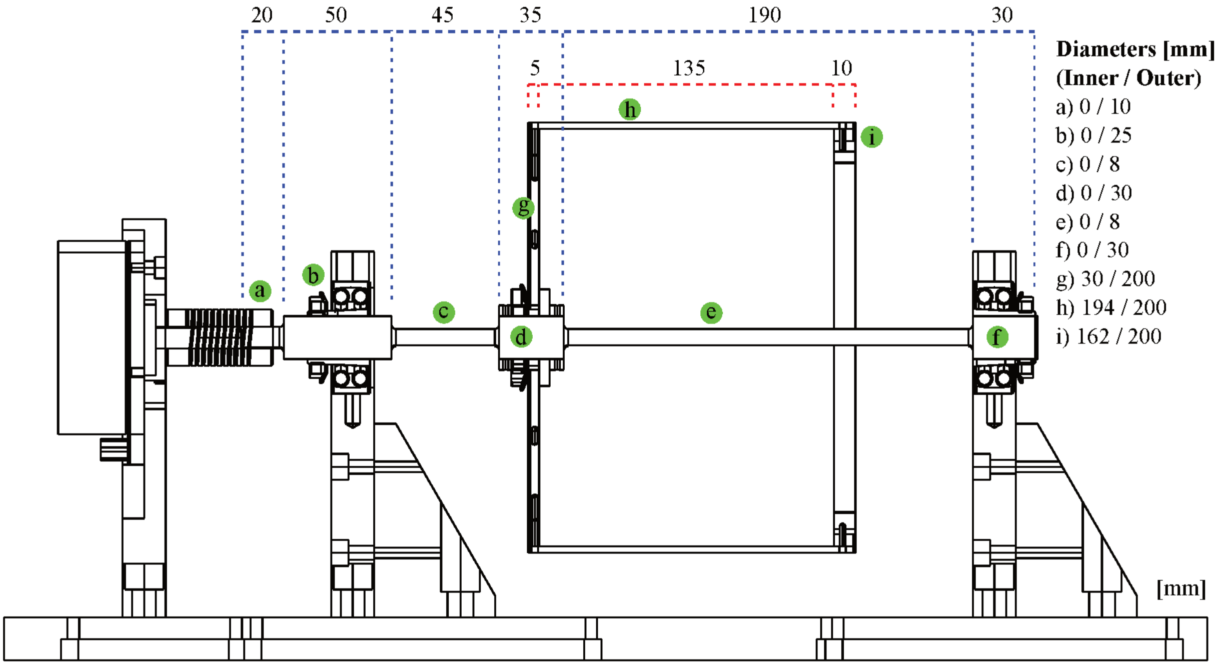

Figure 3.6: Flywheel test-rig scheme, in cross-section view, with its main dimensions indicated

model ZX-LD40 reflective laser sensors, with associated amplifiers were selected. Three of them were mounted on the system, measuring the displacement on the flywheel opening cross section along the *x* and *z* directions ("top" and "side" sensors, respectively), and the third one reads the axial displacement of the flywheel, *y* direction, at a 100 mm radius on its back. This configuration allows for measuring the tilting movement, orbits and wrinkling measurement. Due to hardware limitations, the background noise on the sensors readings range between 40 and 50 μm. Each individual laser sensor has its associated amplifier, and no induction sensors were used on the steel shaft.

Accelerometers and force transducers for EMA were available, and a number of tests were performed, analogous to those for the previous test-rigs. The motor is controlled by a proprietary Printed Circuit Board (PCB) electronic module, linked to a National Instruments$^{\text{TM}}$ (NI) 1950 myRIO board. The latter has been programmed via LabView$^{\text{TM}}$ code, functioning as a DAQ board and permitting a number of different analyses. The motor control and safety operations were performed by the same myRIO board. During acquisition, both the accelerometers and force transducer or the laser proximeters and motor data were linked to the myRIO board, allowing for the same DAQ system to be used for different applications.

Separated power supplies were used for the "power" and "control" circuits, with physically isolated external power sources and grounding, thus avoiding electrical interference within the system. The detailed electronic diagram of the DAQ and control systems can be seen on Figure 3.7.

3.4.3 Experiments Performed

Experimental FRFs and EMA were performed for the system under different configurations, with and without the flywheel mounted and both on free-free condition as well as assembled system configuration. Extra static analyses were made for the system without the flywheel stiffening ring, similarly for both configurations, always on the vertical position. Mode shapes were reconstructed by positioning the accelerometers on strategically located positions, and the associated natural frequencies were identified. Running tests were performed for the system on the vertical and on the horizontal configurations, for the system with and without the stiffening ring. Orbit plots for a set of different rotation speeds and FRFs plotted as a waterfall diagrams were obtained for the system.

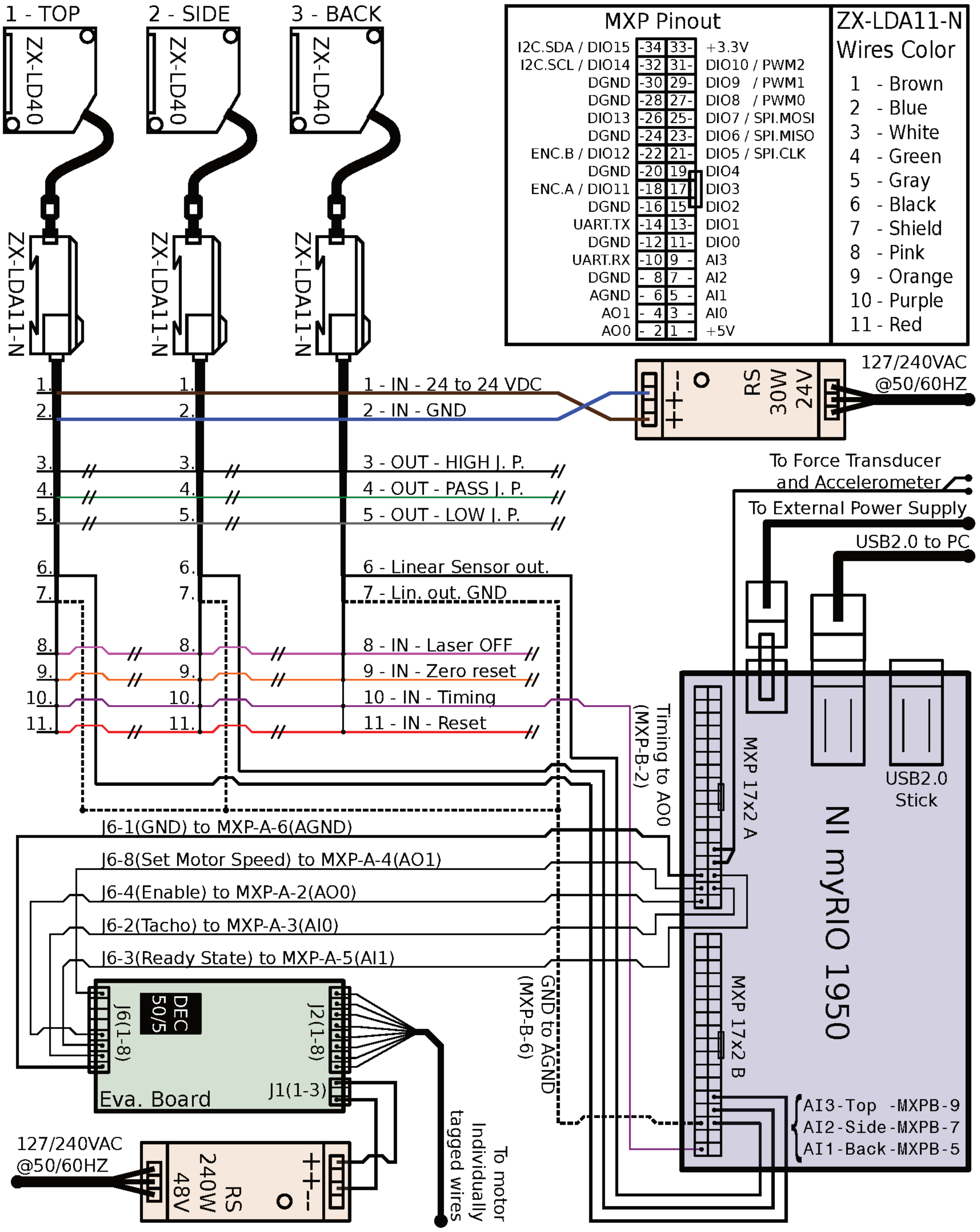

Figure 3.7: Electronic diagram for the flywheel test-rig, with indicated components

Chapter 4

Results and Discussions

According to the theoretical and experimental studies presented in the previous chapters, a number of results were obtained. As previously stated, three experimental rotor systems (*"Onboard"*, *"Composite"* and *"Flywheel"*) and two complete theories (*"Composite Onboard SHBT"* and *"Unified Formulation"*) were developed and tested in this work. The results presented here are organized according to the primary and secondary stages of the study. The first is based on the Onboard and Composite shaft test-rigs, for the validation of the composite-onboard formulation additions on the *Composite Onboard CBT* model. The second group of results are based on the flywheel test-rig results regarding the proof of concept of the *Unified Formulation* approach.

4.1 Results Overview

Since the amount of experimental and numerical data generated is extensive, emphasis will be given to the relevant results for the conceptual validation. The goal is to prove the viability and accuracy of the proposed theories through experimental validation of numerical results.

Objectively, the CBT model with composite materials, onboard dynamics and SHBT additions, is used as a *baseline* reference, since it encompasses the classical theory currently used in most rotordynamics models. Besides, it also considers the additional effects for shear stresses, composite orthotropy with directional coupling, onboard dynamics, dynamic stiffening and gravity load. This first model will be referred to simply as *COCBT*. While this model predicts most of the amplitude-relevant phenomena of the rotor behavior, there are some minor higher order effects that are not adequately represented, as compared to experimental results. The study performed will focus on supplementing these shortcomings via the complete 2_{nd} order B2 UF model, improved with the aforementioned additions. For the sake of brevity, this second model will be referred to as *UF2*.

4.2 COCBT Model Validation

The COCBT model is based on a number of classical theories, including many additions. Therefore, the focus of the following experiments is the validation of the methodology proposed, focusing mostly on the specific innovations introduced.

For the validation of the additional formulations included in the COCBT model, a number of experimental procedures were performed for both the onboard rotor and composite shaft test-rigs. These are divided into the two following subsections, initially discussing the one related to the "Onboard" test-rig dynamics, in partnership with Souza's Master thesis and subsequent works ([54], [56] and [55]). The second subsection presents the advancements associated to the "Composite-shaft" test-rig, resulting from the partnership with Barbosa's Master thesis and its correlated works ([3], [2], [5] and [4]).

For validation purposes a didactic and adaptable software design was preferred, making use of symbolic programming. Therefore, the onboard and composite-shaft results are not compared to the UF2 model, since the numerical integration demanded by the onboard dynamics simulations on the UF2 framework proved to be cost-prohibitive. However, the UF model can be completely numerically implemented, significantly increasing its computational performance. This has not been approached in the present doctorate work since a different focus was aimed at. Besides, lengthy experimental and numerical procedures would require additional time and effort.

4.2.1 Experimental Validation of the COCBT Onboard Formulation

The first experimental design tested is the metallic-shaft onboard dynamics test-rig (Figures 3.1 and 3.2). Its goal is the proof of concept of the onboard dynamics theory, as implemented in the COCBT model. A secondary objective is the validation of the

Timoshenko shear stress correction applied to the model, and the evaluation of any unexpected dynamic behavior.

Then, an initial study was performed with the stationary system, aiming at matching the model mechanical parameters to those of the physical machine. This consists of a FRFs obtained from accelerometers installed at the disc position, impacting the shaft with an instrumented hammer immediately next to the disc attachment point, as Figure 4.1 shows.

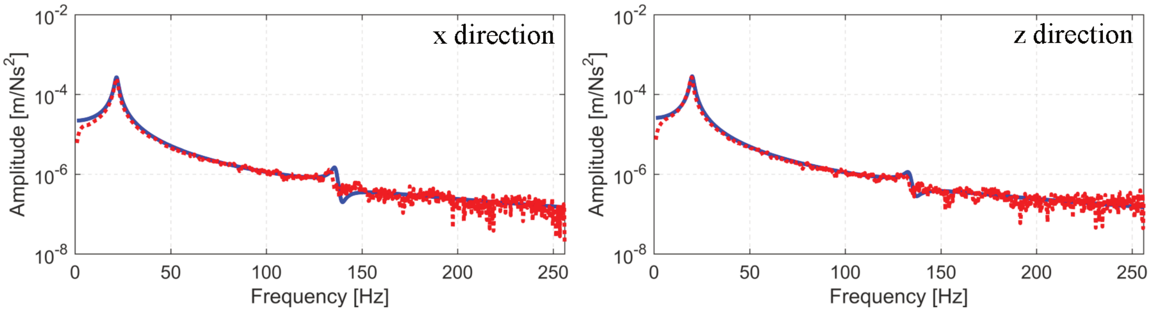

Figure 4.1: FRFs adjustment of the COCBT model with the experimental data, via optimization procedure. The red curve shows the experimental data, while the blue one stands for the numerical simulation

This experiment allowed for the determination of the model bearings stiffness and the system modal damping parameters, enabling the model to predict the experimental results with sufficient accuracy. Since the *forward* and *backward* critical speeds of the first mode were not expected to change significantly from the static case, this stationary system parameters were used on the subsequent running simulations. As can be seen in the graphics, the available accelerometer sensitivity limits the data acquisition below amplitudes of 10^{-6} $m/(Ns^2)$. Since that is the case, the second natural frequency numerically determined as $\omega_{n2} \approx 135$ Hz is disregarded in the following analyses.

Next, a numerical Campbell diagram was determined by using the adjusted COCBT model, as given by Figure 4.2.

From Fig. 4.2 it was possible to numerically determine the critical speeds as given by 1177 RPM and 1375 RPM, respectively the first backward (BW) and forward (FW) critical speeds.

In order to test the COCBT model accuracy in predicting the dynamic and transient response behaviors of the onboard rotor system, two particular test batteries were

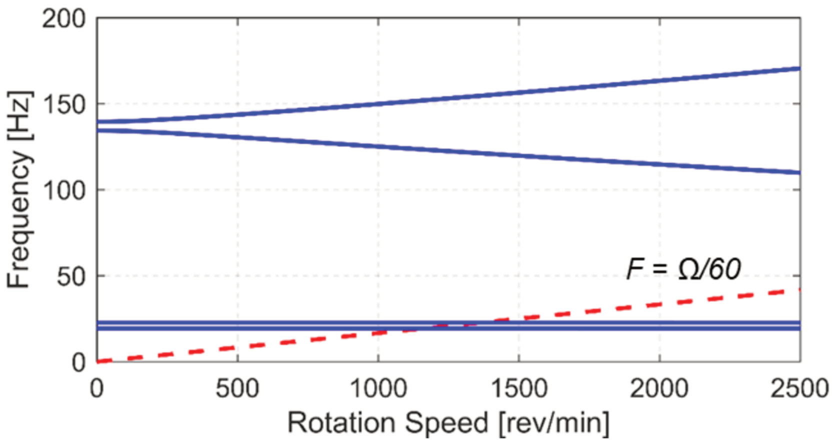

Figure 4.2: Numerical Campbell diagram for the onboard test-rig, as determined by the COCBT formulation

performed. Therefore, the steady state response of the rotor subjected to a base excitation was experimentally obtained. The results were then compared to numerically generated data by using the the COCBT model, applying the same experimental base excitation data, resulting in Figure 4.3. For these tests, the rotor system was maintained at the given rotation speed and base excitation during 5 minutes for each test, after which the data was acquired during 10 seconds. This intended to eliminate any transient phenomena from the results.

As expected, one can note that the dynamic response of the system radically changes when crossing the critical speed. The corresponding system responses were obtained by exciting the rotor base with a sinusoidal force at sub-multiples of the rotating speed. The chosen excitation frequencies were $1/2$ and $1/3$ of the experimental Ω speed, always with the same peak-to-peak amplitude of $a = 5\ m/s^2$ ($\pm 2.5\ m/s^2$, relative to the shaker equilibrium position).

It is important to mention the slight differences between the experimental and numerical responses, which are attributed to a number of factors. Namely, one can point out: a) the model linearity and linear behavior assumptions; b) the small displacements assumption; c) the model uncoupled stress-strain relations between the cross-section and axial directions; d) the physical construction of the system and; e) eventual large bearing clearances or bearing support flexibility. Nevertheless, these results are considered satisfactory since they are under a 5% error margin as compared to experi-

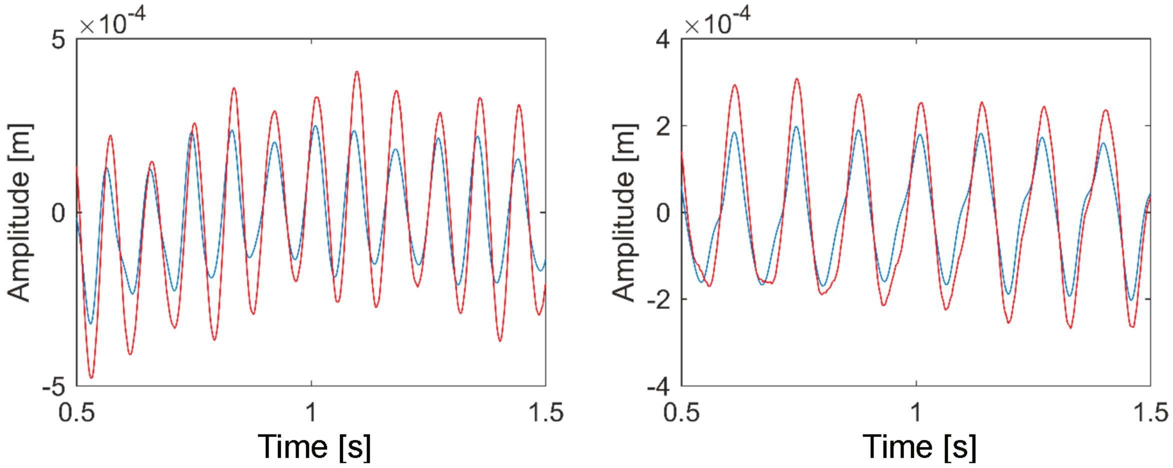

(a) Shaft rotating speed of $\Omega = 900\ RPM$. Operation below the first critical speed

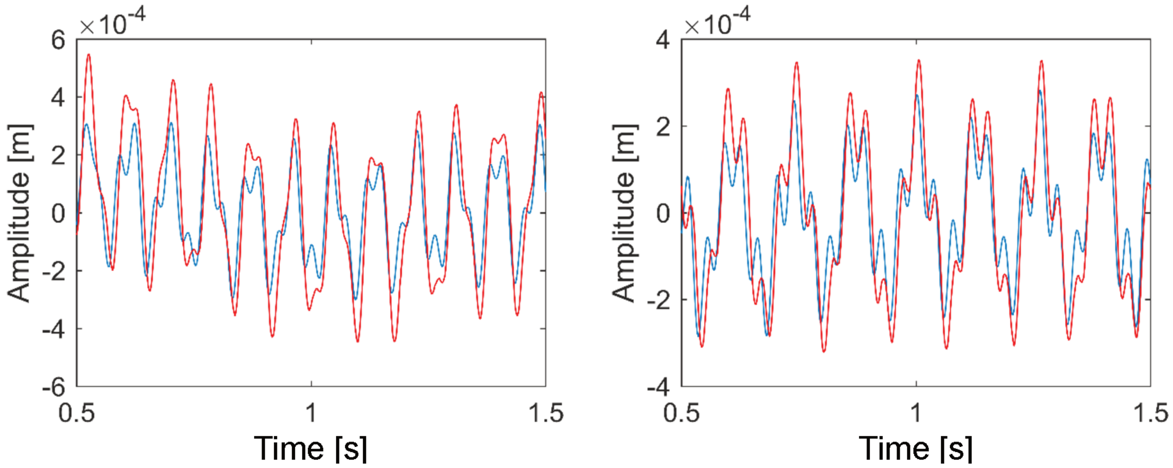

(b) Shaft rotating speed of $\Omega = 1600\ RPM$. Operation above the first critical speed

Figure 4.3: Steady-state time response with sinusoidal base excitation at the disc position on the x direction, at 1/2 (left hand side plots) and 1/3 (right hand side plots) of the shaft rotation speed. The red curves show the experimental data, while the blue one stands for the numerical simulation estimate. Thee base acceleration amplitude is kept at $a = 2.5\ m/s^2$ for all cases

mental tests.

An additional test was also performed, this time focusing on determining the transient behavior of the system and the model capacity of predicting it. It consisted of an impact test, where the shaker submitted the rotor base to an imposed impulsive acceleration. Similarly to the previous test, the base acceleration data was collected and used into the COCBT model, being adjusted and introduced as its imposed base displacement. The two different acceleration amplitude responses are depicted in Figure 4.4. It is possible to observe the proximeter data on the x direction, measured at the disc position, both experimentally and numerically as shown in the left hand side plots. On the right hand side plots the acceleration measured at the shaker baseplate, where the whole rotor system is mounted upon, is displayed.

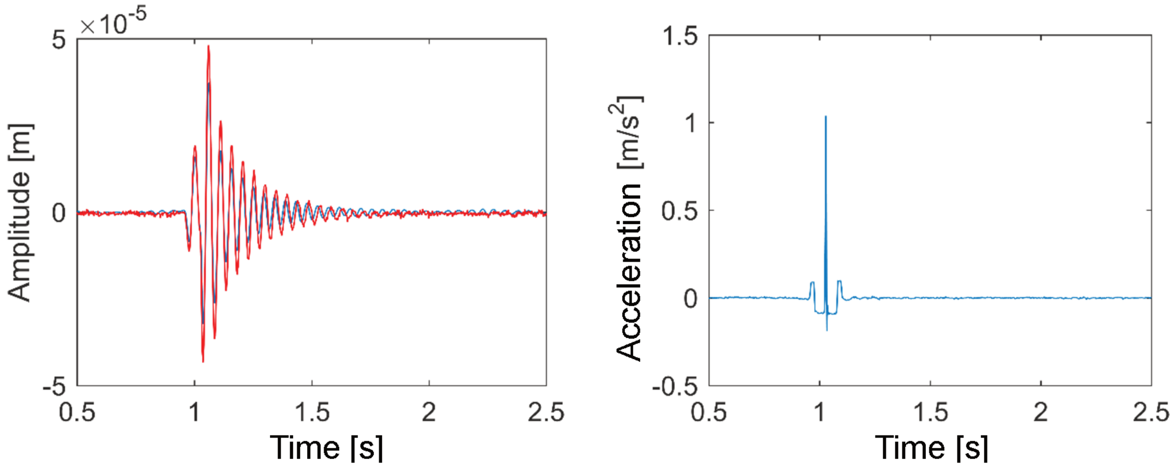

(a) Acceleration amplitude $a = 1\ m/s^2$

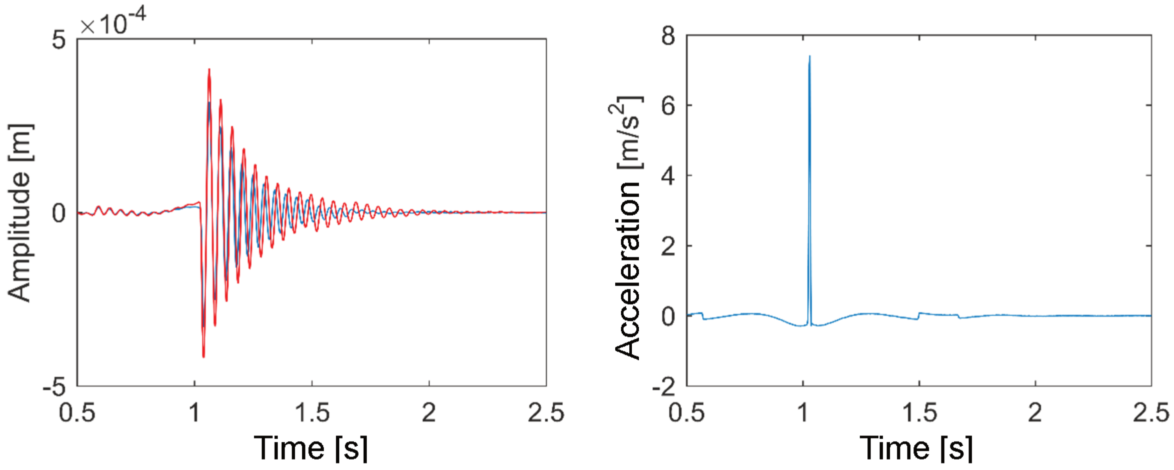

(b) Acceleration amplitude $a = 9\ m/s^2$

Figure 4.4: Transient impact response at the disc position on the x direction. On the left hand side plot, the red curve shows the experimental transient time displacement signal, while the blue one stands for the numerical simulation equivalent. On the right hand side plots are the baseplate imposed acceleration, measured at the plate via accelerometer. In this experiments, the shaft is at rest, $\Omega = 0\ RPM$, and subjected to variable base acceleration amplitudes

While for the first test (Fig. 4.4a) the shaker was able to accurately deliver the defined $a = 1\ m/s^2$ peak amplitude, it produced only about $a = 7.7\ m/s^2$ for the second one (Fig. 4.4b). Consequently, the use of the measured signal as the numerical imposed base acceleration is fully justified. As previously announced for every experimental test performed in this work, the system was operating in a "steady-state" condition before the test was initialized. In the present case, the rotor was kept stationary and time was given to settle the condition for which the impulsive accelerations were imposed. A trigger was set for the acquisition system to initiate the data capture roughly $1.0\ sec$ before the impulsive acceleration peak was applied.

4.2.2 Experimental Validation for the COCBT Formulation

The second test-rig for experimental tests used in this Dissertation was the composite shaft test-rig. Its mechanical configuration is depicted on Figures 3.3 and 3.4 (in the previous chapter), accompanied by its sensors and data acquisition systems description. This test rig is dedicated to the validation of the previously developed COCBT theory, mostly the SHBT approach with its directional coupling capabilities, considering its thick-walled composite shaft and overhung configuration as added complexities.

In this experimental procedure, an additional step was included. During the FRF characterization phase, the system was tested for two conditions: a) free-free configuration - shaft with assembled bearings and discs, with respective mounting sleeves, suspended by elastic Nylon® wires; b) fully assembled system on the bearing pillows, bolted to the supporting structure. These results are given by Figure 4.5, for both configurations, along the x and z directions, also showing the numerical results.

As a cautionary measure, the system was operated at varying subcritical operation speeds for two hours before the FRFs were obtained for the assembled condition, so that any pre-stress influence remaining from the system assembling was dissipated.

The intention of the tests was the identification of any identifiable difference between the readings on the x and z directions. As done for the previous test-rig, the mechanical parameters of the bearings (stiffness and damping) and modal damping factors for the first two modes were determined by an optimization procedure, matching the numerical FRFs to the experimental ones. The relevant curves used for this process are those from the fully assembled system, resulting in a slightly mismatched damping ratio for the prediction of the free-free system.

Highlighted by the experiment, a noticeable difference between the amplitudes of

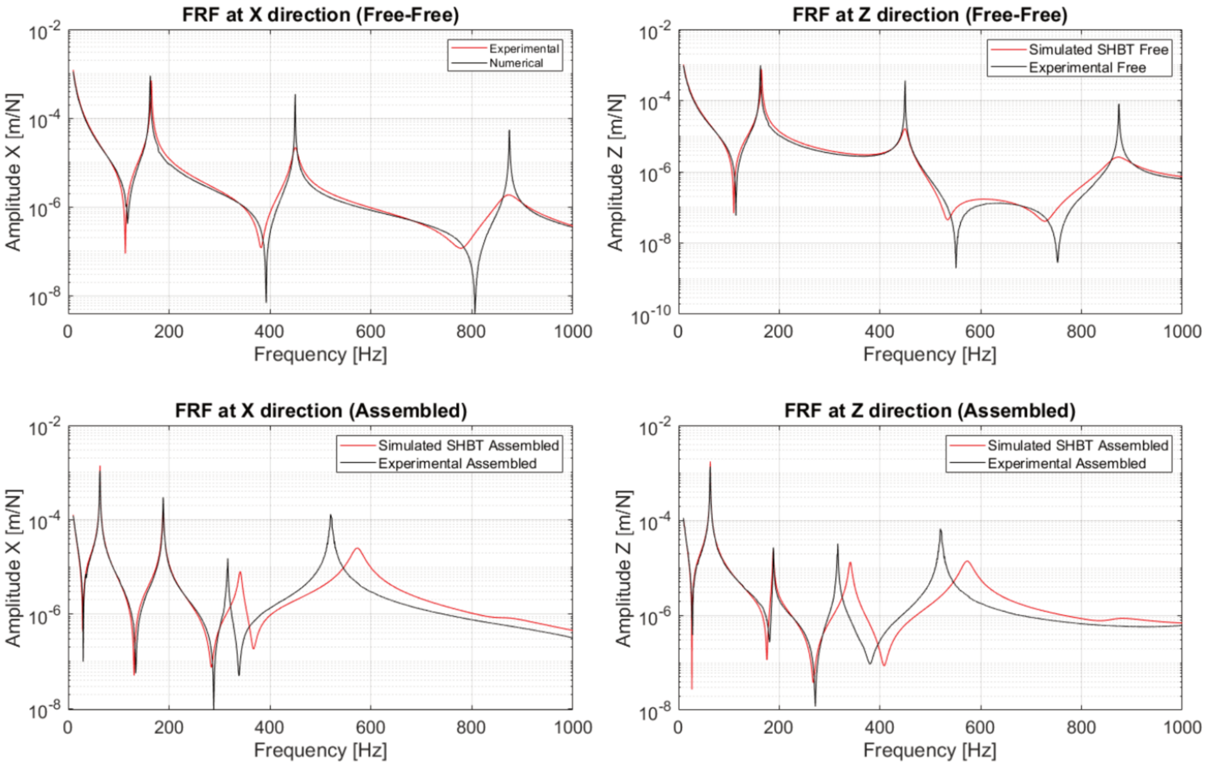

Figure 4.5: Frequency response function for the composite shaft test-rig, for both the free shaft and the fully assembled system configurations

the second natural frequency is visible for the assembled system, depending on the direction analyzed. This is attributed to the bearing supports difference regarding the stiffness between the horizontal and vertical directions. As previously observed (section 3.3), the bearing pillows are mounted on cantilevered aluminum beams, which reduces the bearings effective stiffness determined by the model optimization. Another side effect of this mounting position is the induced asymmetry introduced to the bearings, since the supporting beams have a flat cross-section, making the horizontal direction stiffer than the vertical direction.

Afterwards, a numerical Campbell diagram was determined for the system, by using the adjusted COCBT model, as seen in Figure 4.6.

The resulting numerically determined critical speeds are $1618\ RPM$ and $1638\ RPM$, respectively the first backward (BW) and forward (FW) rotation speeds. These results were corroborated by experimental observations, although not being exactly pinpointed due to hardware limitations. The test-rig was operated below the first critical speed, and tests were made up to a set $1400\ RPM$ threshold, after which the discs rim displace-

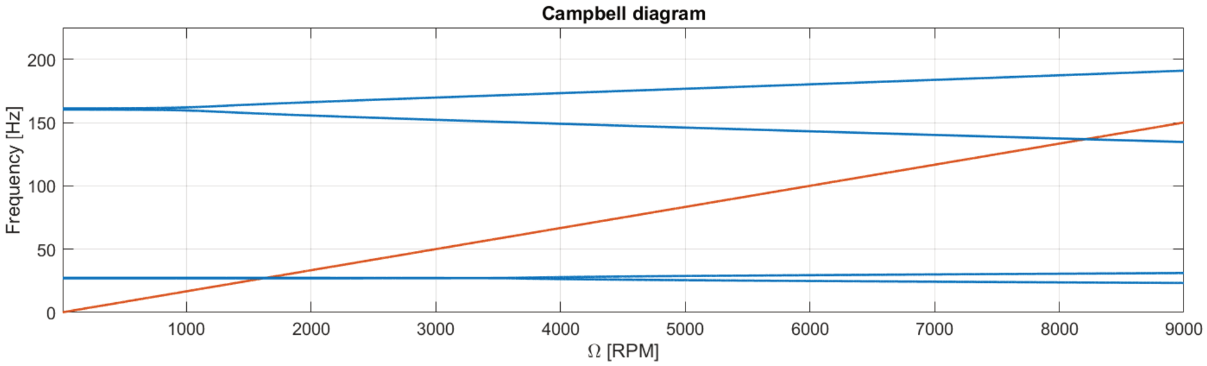

Figure 4.6: Numerical Campbell diagram for the overhung composite shaft test-rig, as determined by the COCBT formulation

ment induced rubbing between the latter and the sensors protective pieces. Therefore, due to sensor range limitations and safety concerns, this system was not tested for supercritical speeds.

The orbit responses of the system (both simulated and experimentally obtained) are presented below by Figure 4.7.

Keeping the experimental procedure, these signals were also acquired after the machine operation during two hours, thus avoiding any transient behavior that might have existed in the system.

It can be noted that the model is able to predict the amplitudes related to the first natural frequency with good accuracy, but fails to identify the higher order harmonic components seen in the experiment. These phenomena are visible on the elliptical numerically predicted orbits, while the experimental ones exhibit visible 2Ω and 3Ω components disturbing the orbits shape.

Another view on these results is presented by Figure 4.8, which shows the same orbits data now simplified into an order analysis for the two discs.

These plots make evident that there are small still present 2Ω and 3Ω harmonics, mostly in the vertical direction. These effects are supposed to be originated from the following possible reasons: a) the composite shaft orthotropic nature, transferring effects from one direction to the other via mechanical coupling; b) the composite material internal damping, which accentuates nonlinear behaviors; c) the system complex foundation, which may have introduced unexpected dynamics on the vertical direction. Since there are a number of possible root causes for these effects, and the model itself

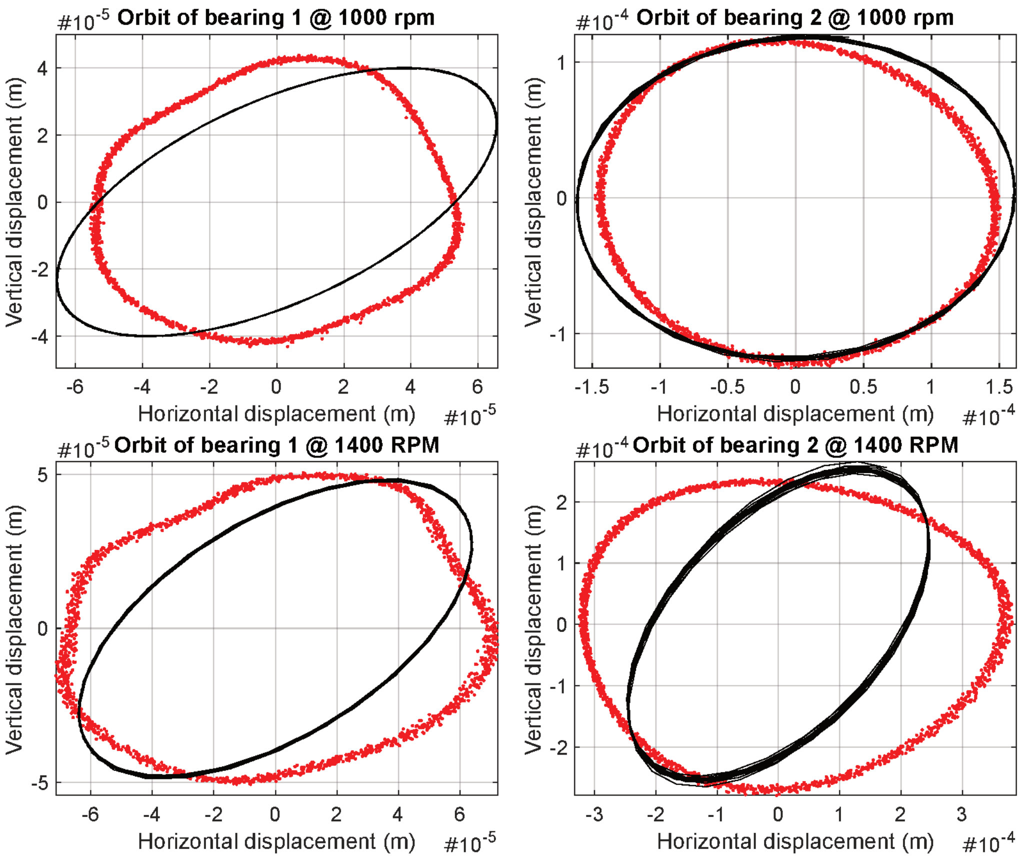

Figure 4.7: Steady-state orbits for the composite shaft test-rig. The sensors are mounted on the discs rims, aiming at the cross-section, in the xz plane, with rotating speeds of $\Omega = 1000\ RPM$ (top graphics) and $\Omega = 1400\ RPM$ (bottom graphics). The axes are normalized

is a linear representation of an intrinsically nonlinear system, the real origins of the mismatch are yet undetermined. Even so, the COCBT model predicted the orbit and displacement amplitudes for the system to a satisfactory degree, staying under 5% of error on the average.

4.3 COCBT Model Performance Evaluation and Usability

In the previous sections, the initial Classical Beam Theory formulation, improved by a Simplified Homogenized Beam Theory equivalent layer integration for composite materials and Onboard Dynamics physics addition was evaluated. An extensive

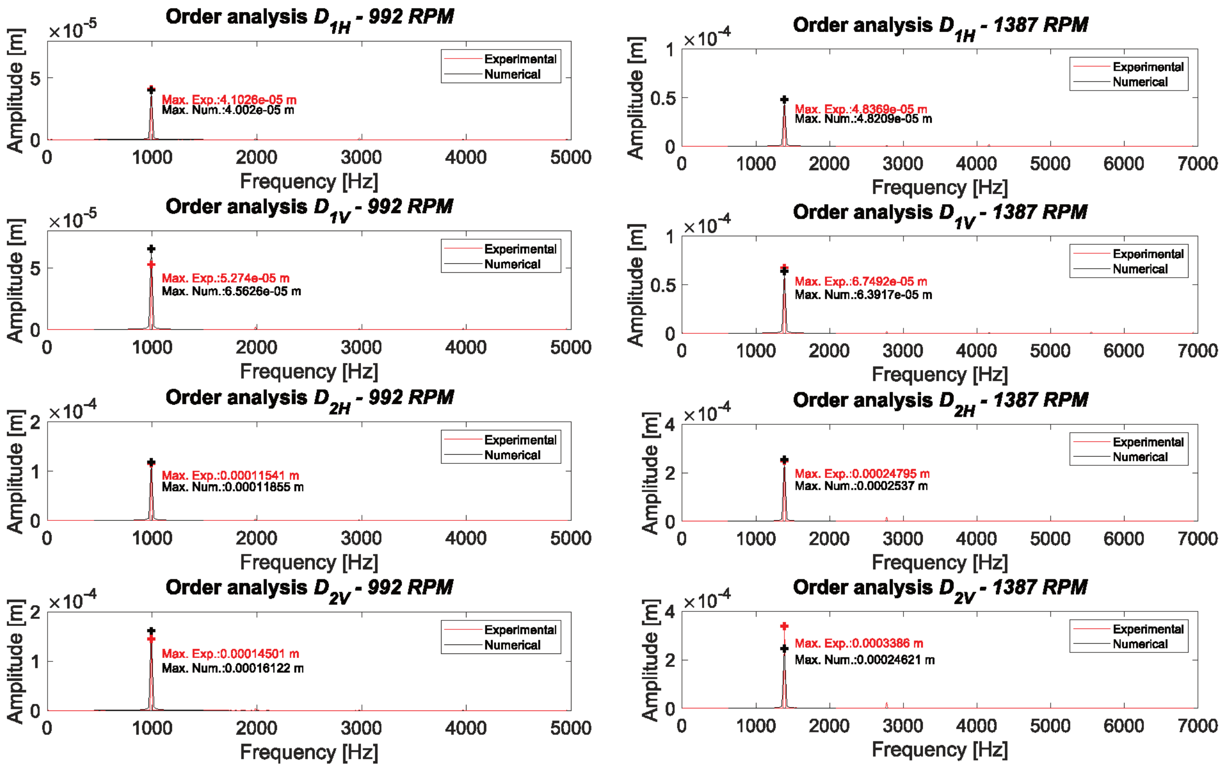

(a) Motor set to $\Omega = 1000\ RPM$ (b) Motor set to $\Omega = 1400\ RPM$

Figure 4.8: Order analysis for the composite test-rig in its steady state operation, comparing experimental and numerical results for two different rotating speeds. The signals were measured in the horizontal x and vertical z directions of the discs cross sections, as identified by the graphics boldfaced subtitles

set of experimental tests were performed on two different test-rigs, for evaluating the presented formulation accuracy on various scenarios.

The COCBT model led to results that follow the suggested error threshold when adjusted to the experimental designs as proposed in the present study. A number of high order effects and unexpected phenomena were perceived on the experimental results, most evidently on the composite shaft data. These effects were not included in the model characteristics and although the model is limited to its linearity it produced acceptable responses, sufficiently accurate for most practical applications. One must highlight that the intended purpose of the performed experiments was to check for the methodology limits and precision in extreme scenarios, hardly found in practical situations.

Another relevant points when analyzing numerical simulations is related to the computational cost and implementation complexity. In the case of the COCBT, the computational cost is affordable, being on par with simple Euler-Bernoulli methods without any additional feature. The most demanding operation is the determination of transient responses, which make use of the Newmark numerical integration scheme.

Therefore, one can enumerate the advantages and disadvantages of the COCBT methodology, as compared with other similar FEM formulations and rotordynamics modeling techniques. The most advantageous features are:

> accurate for dealing with thick-walled cross-section geometries, depending on the mode shape evaluated;
> onboard dynamics physics;
> composite material with orthotropic layers consideration;
> proper representation of transient dynamic effects;
> correct shear stress modeling, via Timoshenko's formulation;
> directional coupling of dynamic efforts;
> low computational cost;
> simple implementation.

and some of its limitations are:

> restricted to circular and tubular cross-section geometries;
> linear model;
> not adequate for extremely thick-walled rotors (such as flywheels).

Consequently, the COCBT formulation as proposed in this work is a broadly applicable tool, which can solve most common industrial problems. The added functionalities enable the technique to accurately cover onboard machines and composite shafts, even above the first critical speed.

4.4 UF Model Validation

The Unified Formulation approach is an ideal framework for FEM modeling of complex systems, being directed to rotordynamics problems in the present contribution. It features arbitrarily and independently expansible interpolation orders, and consequently its physical representation capacities are limited by precious few constraints.

Being the UF an arbitrarily expansible method, a preliminary numerical study on rotor systems was performed [23], in order to determine a sufficient cross-section interpolation order and number of nodes per element. Making use of a UF FEM model for a system configured similarly to the composite shaft test-rig described in the previous section, a number of optimum strategies were determined and evaluated. This trials focused on determining some important UF features to be set for general rotor analyses, namely: a) the ideal number of nodes per element in the axial direction; b) the ideal order of the interpolation functions for the cross-section stress-strain relations; c) the best form or diagrams to display the model responses. These goals were pursued methodically, using a known system as its study subject.

4.4.1 Pre-evaluation of the UF Theory

From the bibliographical review on the UF and other FEM methods, a 2-node shaft element is determined to be sufficient for almost all slender shaft problems. A requisite for it is that a sufficient longitudinal discretization is made, and no large-scale deformations are present. Such large-scale deformations refer to those found in metal forming manufacturing processes, being a few orders of magnitude greater than those found in rotating shafts during even extreme operating conditions. Therefore, the first question has been answered.

As a simple case study, a composite rotor shaft, very similar to the one of the previous test-rig, was modeled by using 39 UF B2 elements, with cross-section interpolation functions of 1st, 2nd and 3rd orders. Its main components are depicted by Figure 4.9.

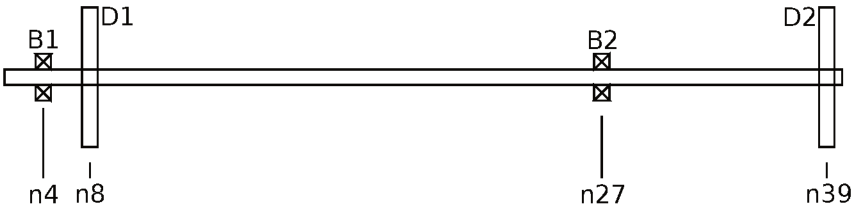

Figure 4.9: Numerical case study; rotor shaft FEM representation

The different model orders are then compared via:

> displacement time-signal generation for run-up operations of the machine;

> natural frequencies determination via modal analysis, covering the same frequency range of $0 \sim 45\ Hz$;

> FRF response comparison, determined at the discs for various rotating speeds.

The system displacement response, produced on the disks nodes along the horizontal and vertical directions, is presented by Figure 4.10.

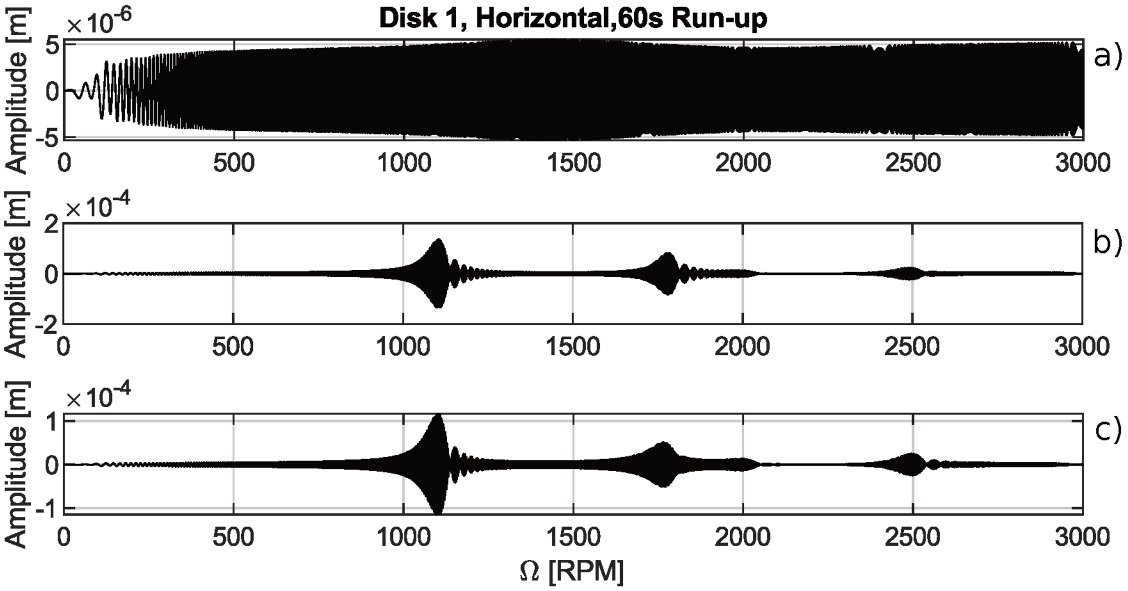

Figure 4.10: Numerical case study rotor system displacement response during run-up operation from 0 to $3000\ RPM$. Obtained at the first disc, in the horizontal direction, for the three model orders considered: a) 1_{st} order; b) 2_{nd} order; c) 3_{rd} order

Modal analysis provides the natural frequency values for the different models proposed, and also for the previous COCBT model, as comparative data, as presented in Table 4.1.

Table 4.1: Natural frequencies (Hz) detected from the different model orders for the numerical case study, at $\Omega = 0$.

CBT	44.71	44.71	-	26.12	26.12	23.80	-	-	5.76	5.80
UF1	44.71	44.71	-	26.12	26.12	23.31	-	-	5.80	5.80
UF2	41.58	41.28	39.73	26.46	26.34	23.57	11.83	11.83	5.67	5.67
UF3	41.61	41.29	39.74	-	-	24.89	11.84	11.84	5.67	5.67

In the following, a Campbell diagram is obtained for each formulation order, by using the same method as the one of the COCBT model. A comparative waterfall diagram is determined, covering the same frequency and operating speed ranges as the Campbell diagram. This waterfall plot is akin to an experimental Campbell diagram, but obtained from the UF FEM model. It consists of a series of FRF responses of the rotor system, obtained at the position of the discs along both the x and z directions for a number of discrete rotating speeds. These FRFs are assembled in a numerical 3D array, where the axes correspond to the systems rotating speed Ω, to the natural frequencies ω_n and the corresponding displacement amplitudes $x(y, t, \Omega)$ or $z(y, t, \Omega)$. The resulting image is presented by an isometric representation as a 2D plot, as shown by Figure 4.11.

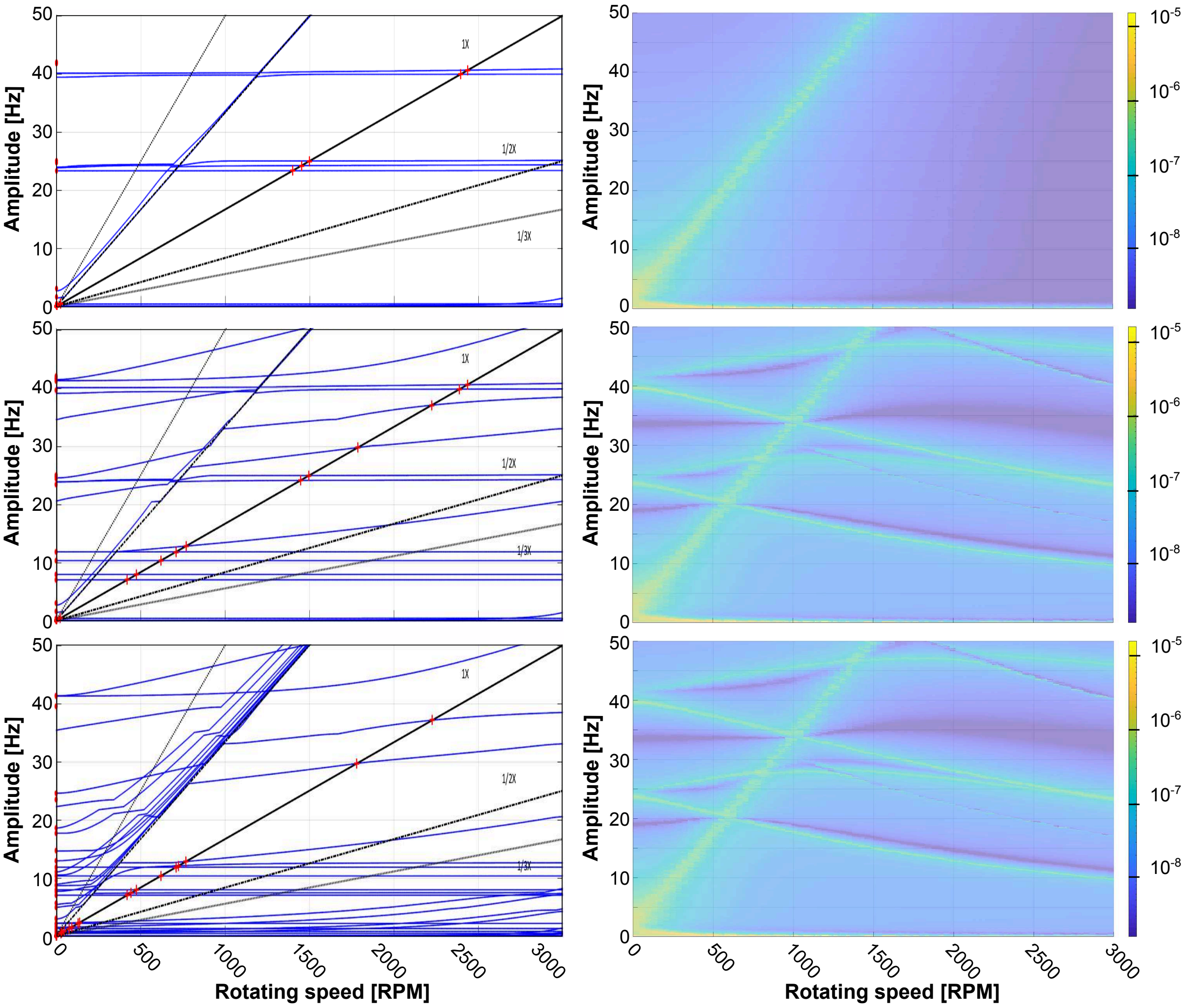

Figure 4.11: Campbell and waterfall diagrams for the numerical case study. The left hand side group shows present the standard Campbell diagrams, while the right hand side group the waterfall diagrams. The pair of diagrams on the top of the figure corresponds to the Full UF1 model; then, the Full UF2 results are presented; and the final pair of plots correspond to the Full UF3 model.

Given the nature of the UF model, a number of additional frequencies and phenomena were expected to be detected by higher order models. However, it is observed that not all of the modes have considerable vibration amplitude, nor any relevant effect on the rotor operation appears. Consequently, two possible solutions can be explored: the first is the application of the *Best Theory* procedure, as explained in [17]; the second is the use of the waterfall plot and amplitude-dependent analyses. By choosing a response that is amplitude-dependent, one can observe the proper system behavior through the full UF model, without neglecting any factor that might be relevant in further developments. Nevertheless, by using full UF formulations, one generates a "polluted" Campbell diagram. In addition, the waterfall plots leads to the response of a given node of the system, allowing for a more focused analysis.

Considering the other diagrams and response types generated for the UF framework, they might necessitate some adaptations regarding their standard implementations. These changes have to do with the coding, which require a similar generalization process as the one applied to the UF architecture. Obviously, a common FEM response with standard physical interpretation are expected.

By observing the above numerical results, one can conclude that a Full UF1 model is insufficient to provide all the insight on the studied systems, while a Full UF2 model provides an accurate and concise representation. The Full UF3 model brings the same useful information as the UF2 but polluted by irrelevant data. The straightforward conclusion is that the Full UF2 model is the ideal approach to handle the present problem successfully.

4.4.2 Experimental Results for the Flywheel Test-rig

Since the goal of the UF2 formulation is the representation of the systems that the COCBT model fails to represent, an additional test-rig was designed and constructed. Referred to as the flywheel dynamics test-rig, it features a polycarbonate flywheel, which favors complex dynamic interactions involving the rotor thin metallic shaft and the flywheel. Such phenomena are not accurately predictable by CBT models, such as the COCBT. A clear description of the dimensions and features of this new test-rig is found in the previous chapter, Figures 3.5 and 3.6, while its data acquisition systems and sensing instrumentation is shown by Figure 3.7.

Given the complexity of this system, it was thoroughly studied by performing a bat-

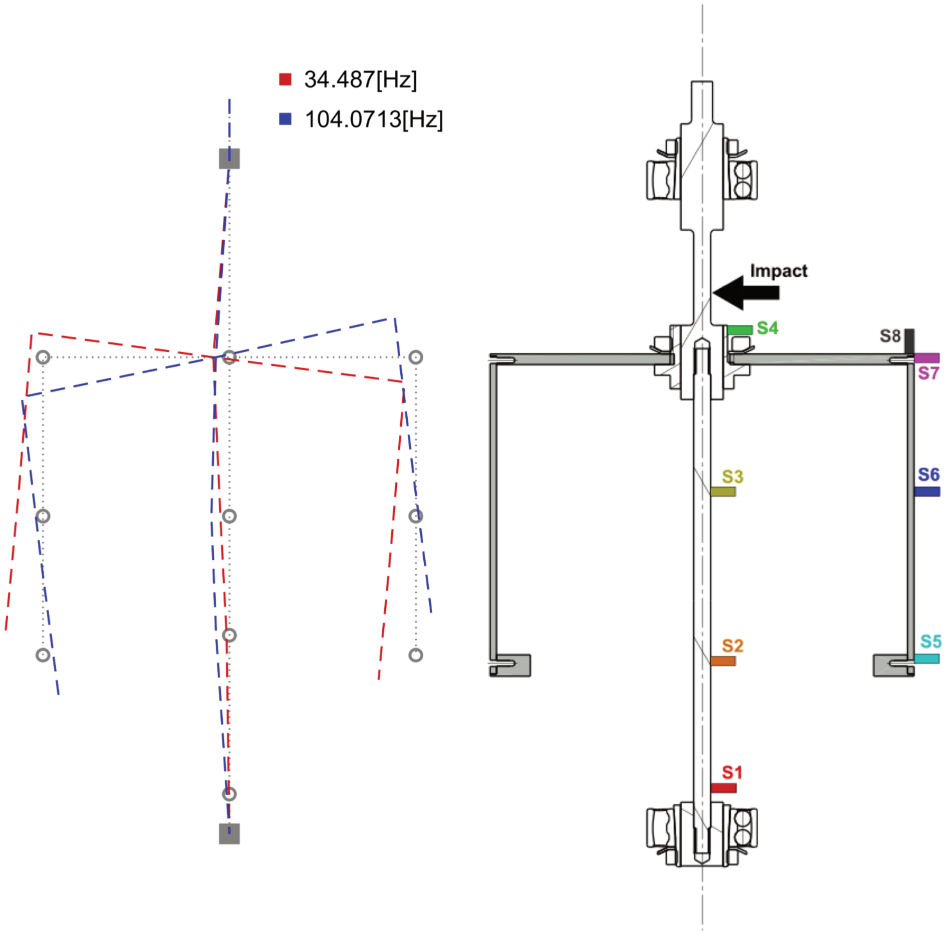

Figure 4.12: First two mode shapes for the flywheel test-rig, covering the utilized frequency range

tery of tests and monitored operating conditions. An experimental reconstruction of the mode shapes, followed by the Bode diagram containing the original FRFs were obtained for the stationary rotor, as given by Figures 4.12 and 4.13, respectively.

One can note that the system is heavily damped, mostly due to the polycarbonate plastic material composing the flywheel and the rubber shielding found in the bearings. This resulted in flattened resonance peaks on the Bode diagram, and in some loss of coherence for the low frequency range. Another reason for this behavior is the accelerometer operating frequency range, which goes from 20 to $20k\ RPM$, limiting its sensing capacities. The experimental procedure was performed with the system mounted on its vertical configuration, with the open end of the flywheel facing the ground.

The first two natural frequencies, for the stationary condition, were also determined

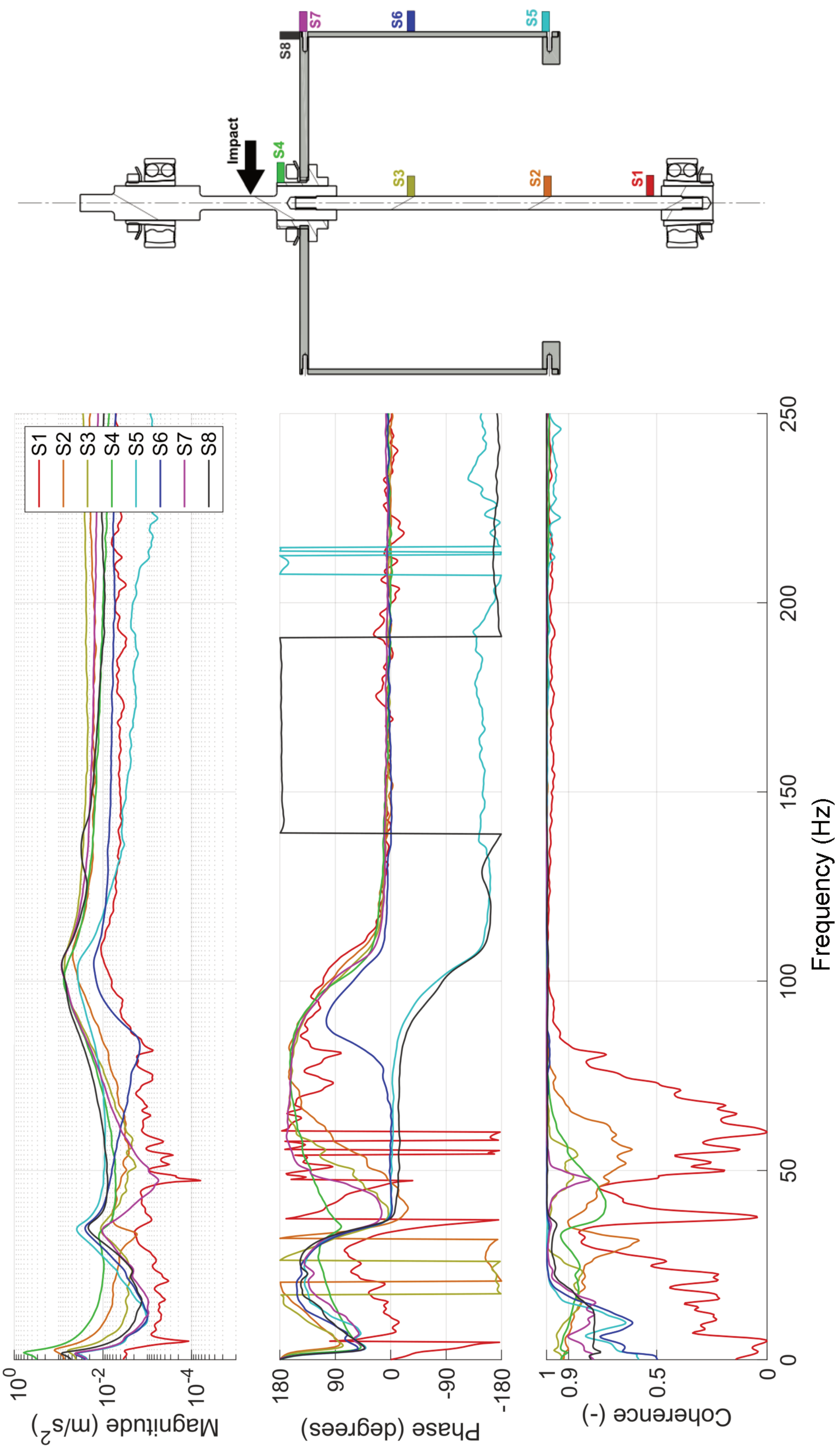

Figure 4.13: Bode diagram for the flywheel test-rig, indicating the sensor positions and their respective experimental acceleration responses

for the system, namely $\omega_1 \cong 34.5$ and $\omega_2 \cong 104.1\ Hz$. It is also remarked that for systems with considerable rotating inertia, the effect of BW and FW frequencies separation on the pairs of modes of the Campbell diagram will be accentuated. This phenomena is directly dependent on the rotary inertia, and therefore on cannot make the assumption that the stationary values represent the dynamic behavior of the rotating rotor.

Regarding the tests performed with the machine in operation, the orbits were determined for the system for a number of rotating speeds, for both x and z directions. A FFT map of the system response was also obtained for the same discrete frequency range. The corresponding results are presented in Figures 4.14 and 4.15.

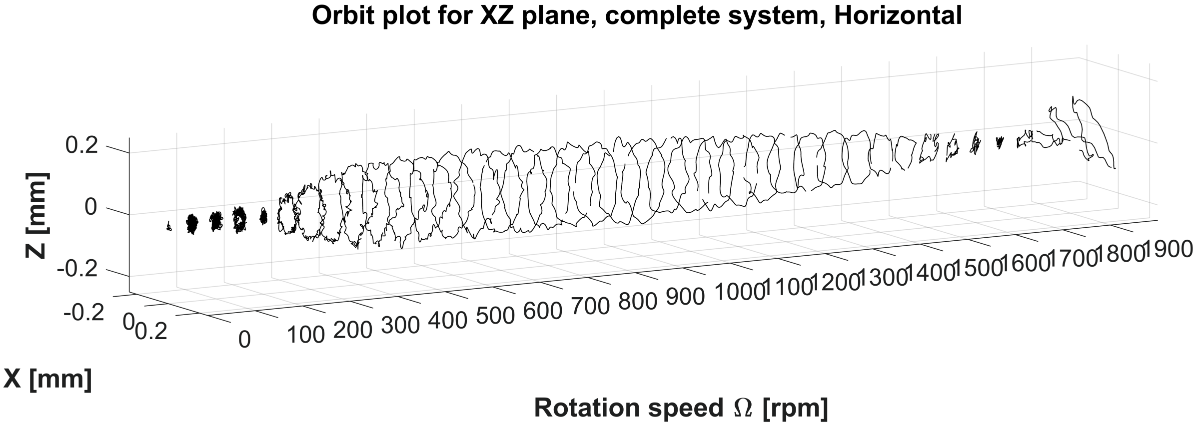

(a) Orbits acquired for the steady-state condition along the horizontal direction

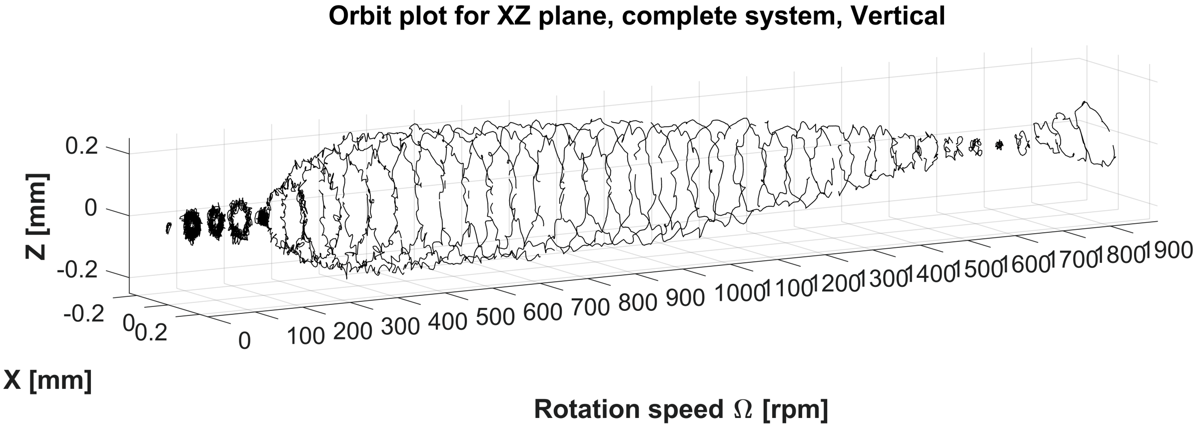

(b) Orbits acquired for the steady-state condition along the vertical direction

Figure 4.14: Run-up orbits for the flywheel test-rig. (a) horizontal configuration; (b) vertical configuration.

It is recalled that the three sensors are mounted on the flywheel, a pair on the open-ended rim measuring the cross-section displacement (x and z), while a third one

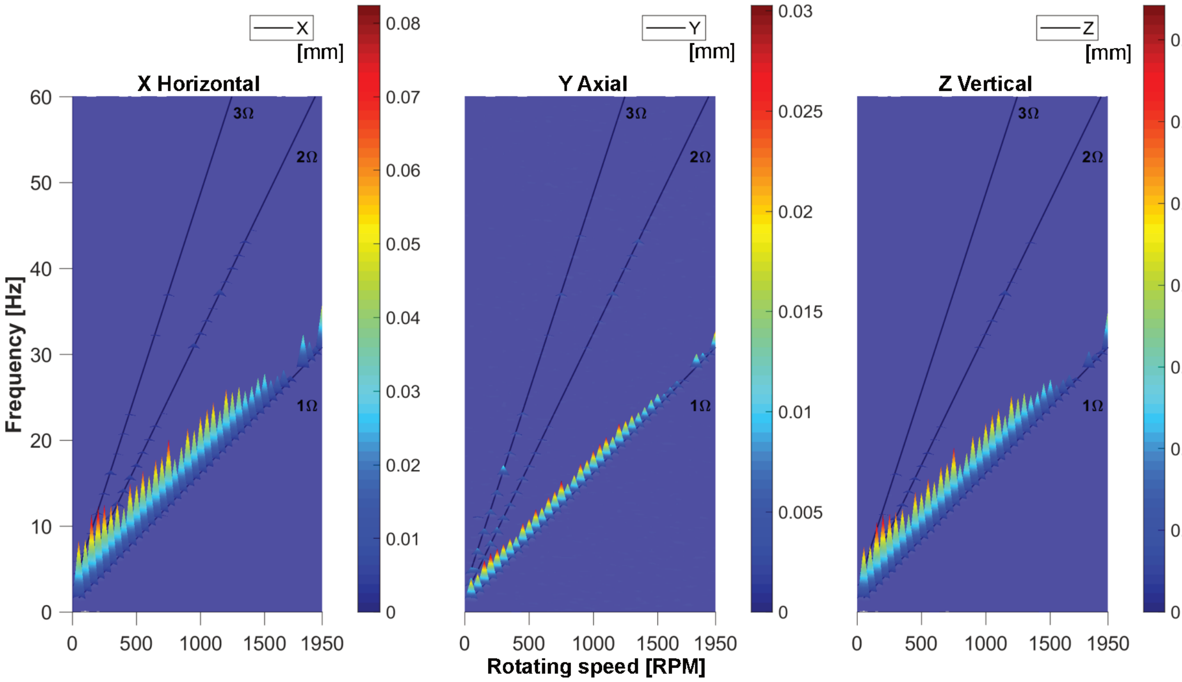

Figure 4.15: FFT mapping of the displacement response of the three sensors mounted on the flywheel, measuring its frequency-domain response along its full operating range. This operation was performed for the vertical configuration

is mounted on its back, measuring the bottom plate edge axial movement (y). The amplitude scales are the same and the response along the x and z axes are normalized, thus facilitating the visual comparison for different conditions and operating speeds. It is worth mentioning that the system was allowed 5 minutes of undisturbed and stable operation at every discrete rotating speed imposed, before the data acquisition was initiated. Therefore, it is expected that no transient effects are significantly found on the signal.

In both response types it is evident that the synchronous 1Ω harmonic is very pronounced, while the super harmonics 2 and 3Ω are only minimally identified in some frequencies. There is also an interesting phenomena at about $1750\ RPM$, as the orbits amplitude reach a minimum, both on the horizontal and the vertical operating configurations.

4.4.3 UF Experimental Validation

Having completed the experimental testing for the third test-rig and chosen the ideal theory to apply to the UF method, the numerical validation of the technique was performed. The physical system was modeled by using an UF2 model, containing 105 finite elements, measuring $5\ mm$ each, with varying radii. The mesh is split into two connected shafts, one for the actual metallic shaft (ranging from nodes 1 to 74) and another for the flywheel (from nodes 75 to 105). The meshing and geometry considered are given by Figure 4.16.

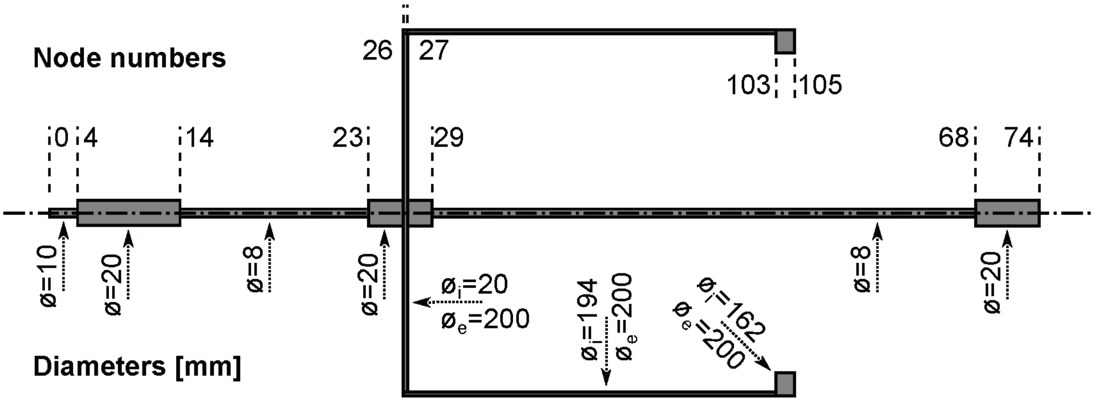

Figure 4.16: FEM meshing and diameters considered for the flywheel rotor model. Above the shaft center line the mesh nodesis presented

From this model the natural frequencies were determined for the rotor system, as presented in the histogram of Figure 4.17.

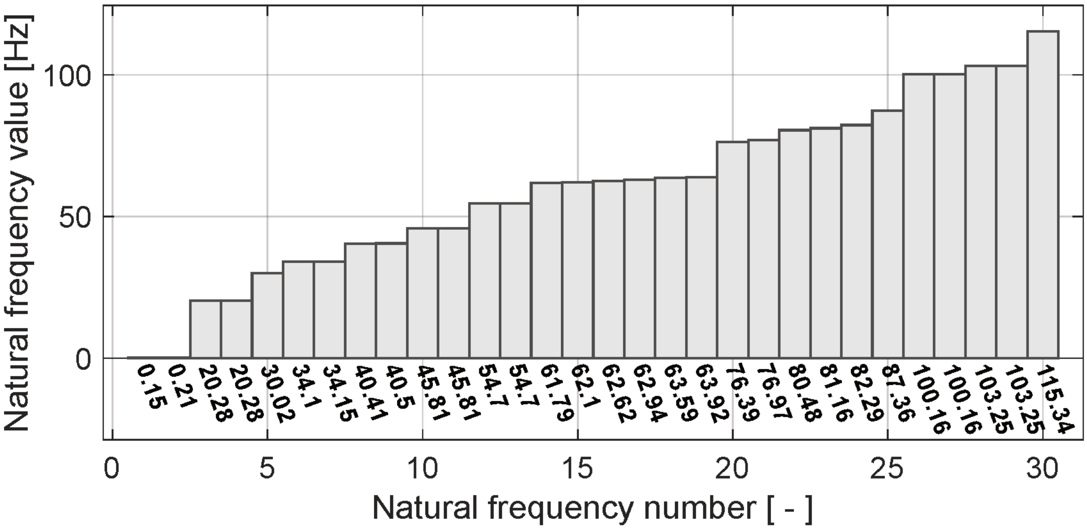

Figure 4.17: Flywheel rotor natural frequencies, covering the rotor operational range

Again, as seen before on the composite shaft rotor test-rig, there are a number of unimportant natural frequencies detected by the modal analysis. A Campbell diagram for the system, covering the full frequency range utilized is shown Figure 4.18.

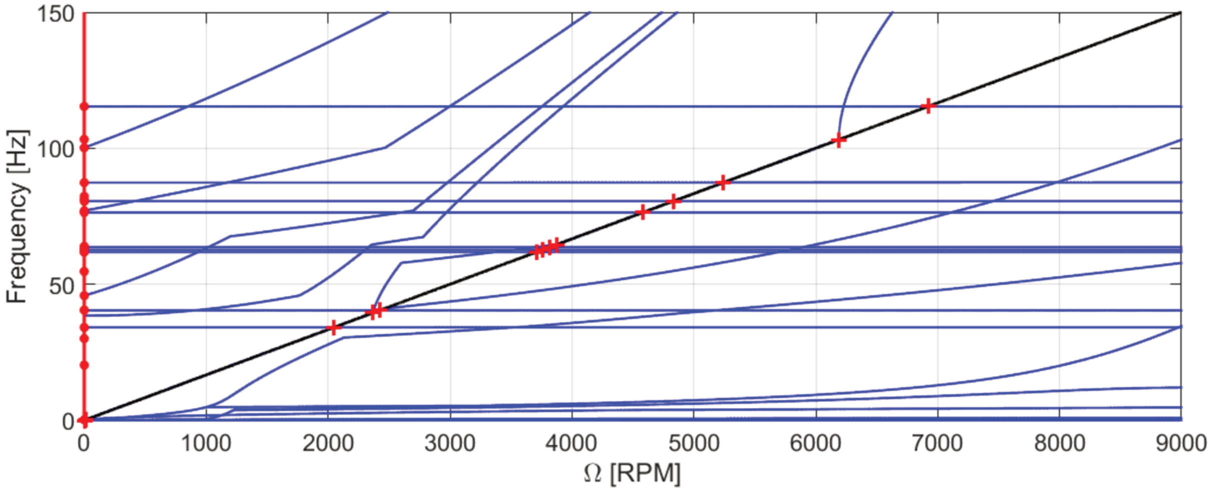

Figure 4.18: Campbell diagram, obtained by using the UF2 model for the flywheel test-rig

Similarly to the previous test-rig and to the natural frequencies determination, a number of irrelevant modes are found. Nevertheless, the frequencies determined by modal analysis for $\Omega = 0$ corresponds correctly to the results. As a side note, the discontinuities present in the Campbell diagram are a common occurrence, but they do not indicate errors. They are simply due to the methodology inability to track modes individually, since they switch orders in the sorting procedure. Therefore, observing the results on an amplitude-dependent analysis, a waterfall plot is generated for a node at the flywheel open ended rim, corresponding to the horizontal proximeter position, as shown by Figure 4.19.

Achieving the goal of presenting a clean and correct result, the waterfall diagram shows the relevant phenomena in terms of amplitude. It can be seen that there are three main modes for $\Omega = 0$, from which the first two match the pairs numbered $6-7$ and $28-29$, on the modal analysis results depicted in Figure 4.17. The measured error is of $0.3\ Hz$ for the first pair and $0.8\ Hz$ for the second symmetric mode, as compared to the values obtained from the experimental modal analysis.

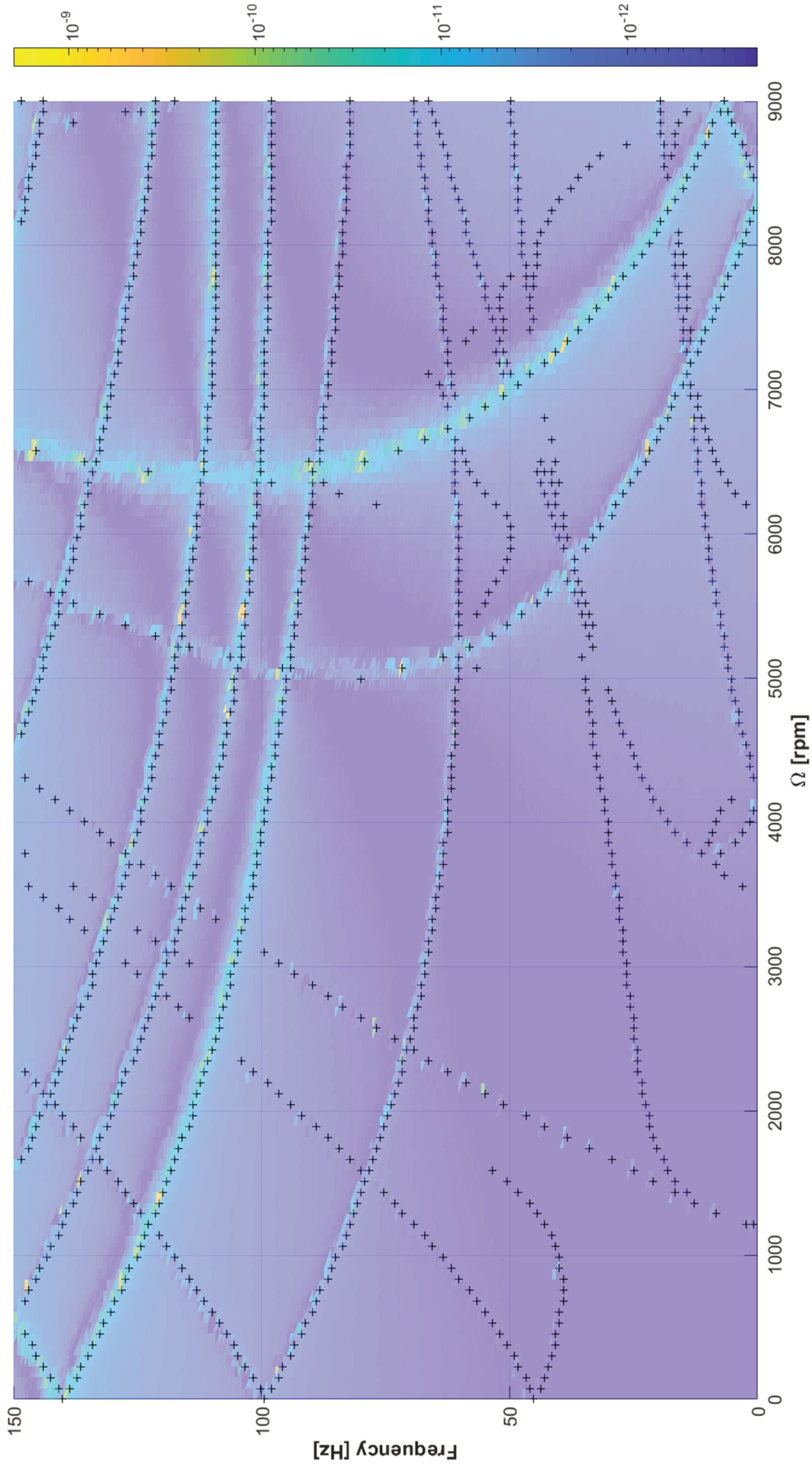

Figure 4.19: Waterfall diagram for the flywheel test-rig, featuring a peak detecting algorithm to identify the relevant points with "+" markers

4.5 UF2 Model Performance Evaluation and Usability

From the presented results, it can be concluded that the UF2 formulation is capable of representing the flywheel test-rig, going as far as modeling the flywheel as a shaft element. Not only that, but also its connection to the metallic shaft and associated dynamic interactions.

A noteworthy point is that the UF2 mode is not optimized to adjust mechanical properties to those stemming from experimentation and, regardless of that, produced quite close matching results. This raises two relevant points to observe about the formulation conveyed:

- 1_{st} the analytical methodology is computationally costly, making optimization procedures unnafordable;
- 2_{nd} the formulation represent the physical phenomena correctly, being able to obtain even irrelevant terms that would have been otherwise neglected.

A solution to the first problem corresponds to a simple modification on the algorithm nature, changing it from the current "didactic" and analytical form to a much faster numerical one. This would potentially reduce its time by a few orders of magnitude, thus allowing for even heuristic optimization methods to be applied.

Regarding the second point, the same observation made for the composite shaft test-rig analysis is made. While it may be unnecessary to consider all the physical terms all the time, they do not considerably increase the execution time and the disturbances can be smoothed via adapted amplitude based analyses. On the other hand, while some terms may seem irrelevant at a given operation condition they may as well be dominant in others or even interact with other modes in unexpected ways.

Chapter 5

Conclusions

Initially, the contributions of the current research effort to further understanding composite shaft rotordynamics are presented, with emphasys on the primary objectives of the present dissertation. Later, the mathematical formulation and its nuances are taken into account, followed by comments and suggestions regarding their implementation. Simultaneously, the two developed algorithms - COCBT and UF - are evaluated on their overall features and applicability, with a few suggestions for future directions on how to improve their performance and usage. Next, a recap regardinag the experimental test-rigs is presented, covering their manufacturing processes, features and noteworthy details on the tests performed. Finally, some future works are suggested and the final remarks are made.

5.1 Contributions to the State-of-the-art

A number of different formulations and methodologies for the study and modeling of rotating systems were evaluated on this dissertation. Some detailed phenomena were given special attention, and a few FEM methodologies were evaluated and compared with respect to their capabilities. These were then tested and validated against experimental results, by using dedicated test-rigs. Further on, the detailed formulations were appended to the proposed FEM models, resulting in two final methodologies. These two have different goals and functionalities, but both achieve the research initial goals.

Considering the final COCBT and UF models, they feature the required primary capacities detailed as requisites:

> (COCBT and UF) extended damping and orthotropic material considerations;
> (COCBT and UF) capable of accurately representing moderately thick-walled composite shafts;
> (COCBT) capable of accurately representing onboard dynamics.

In addition, the secondary goals were also achieved by the proposed models:

> (COCBT) comparatively low computational cost;
> (COCBT and UF) layerwise or adequate equivalent layer material physics;
> (UF) aptitude for arbitrary cross-section geometry and wall thickness;
> (UF) detection of membrane and plate-like wall deformations, such as wrinkling, warping, etc.;
> (COCBT and UF) proper representation of transient dynamic effects, such as shaft stiffening;
> (COCBT and UF) shear stress representation;
> (UF) easily adaptable formulation.

Therefore, the contributions of this research to the literature are related to the two models presented together with the thorough evaluation of their associated numerical methods and experimental procedures, for validation purposes.

5.2 COCBT and UF2 Models Outcomes and Appraisal

Initially, regarding the physical phenomena represented by both models, it was found that they encompass the vast majority of practical situations where rotating machines are employed. Composite shafts, orthotropic materials and damping effects, thick-walled tubular cross sections, onboard dynamics, shear stress effects, directionally coupled stresses, dynamic stiffening and gyroscopic effect were all considered in both the COCBT and UF models. The resulting methodologies have been both improved by these dedicated formulations, which have been incorporated to the respective FEM methods.

Regarding the COCBT model, it appears as a broadly applicable and lightweight model. It is capable of representing either composite or metallic shafts with tubular of solid cross-sections, featuring discs, bearings, unbalanced masses and gyroscopic effect, with all the above mentioned capacities. The implemented algorithm itself a running speed on par with the most basic Euler-Bernoulli models, in a way that it is usable for mechanical design purposes and any design context where optimization procedures are required. While the resulting model capabilities are still linear, these are already sufficient for most cases and still very much applicable for current industrial machinery.

Regarding the UF framework, a much more sophisticated methodology is developed. Its main characteristic is its arbitrary nature, allowing for the whole formulation to be remade and adapted at will, via a simple order and element type choice. With this capacity comes the drawback of having the necessity of specializing the analyses applied to it and/or to "filter" the formulation for its relevant terms, by considering the "best theory" procedure. Regarding its adaptability, the UF model can be degenerated through the "best theory" approach to be simplified into providing the same physical model as the one provided COCBT. Being an emergent technology, only very recently applied to rotordynamics, these situations are expected to be improved in the near future. Simpler alternatives are expected in this area of research. Nevertheless, solutions to both problems are already available, as described in this dissertation, should this methodology be required by a specific complex problem.

As a last analysis, both models are viable and applicable to practical situations. The choice between them, or if another strategy should be sought, depends on the model complexity and the engineers understanding of the problem. For a relatively simple and well understood problem, the COCBT approach should prove to be sufficient. On the other hand, the UF framework can be implemented into an adaptable tool, resulting in a completely numeric and optimized algorithm, covering situations where the COCBT would be used and those where it would require a more sophisticated approach. As an example, for the complex flywheel system studied in this dissertation a relatively simple UF2 model was able to represent the relevant physical features (including a number of irrelevant terms).

Regarding the scientific contributions of the present dissertation to the state-of-the-art of rotordynamics, some publications were developed. Most of the preliminary results, directly related to the first model approached, are already published in journal papers and conferences, such as [4], [56], [3], [47], [5], [2] and [55]. These are linked to the work developed with the first model and first two test-rigs, in partnership with Msc. M. S. Sousa Jr. and Msc. P. C. P. F. Barbosa. Additional contributions are ongoing, now featuring the UF model and the flywheel test-rig, as published in [23] and [22]. Supplementary manuscripts are being developed for periodic journal publications, focusing on the: a) UF modeling of the flywheel system, regarding the algorithm and its *best theory*; b) UF modeling of the flywheel system, analysing the instability origins on the flywheel system; c) conparative studies with the UF and CBT models and; d) sensibility and uncertainty analyses on a UF rotor model. These are expected to be submitted within the next two years.

5.3 Experimental Test-rigs Overlook

One of the relevant features of the present research work is the design, manufacture, assembling and testing of the three independent test-rigs utilized. They allowed for a very broad spectrum of mechanical behaviors to be observerd, evaluated and tested in a controlled environment, providing significant insight into many industrially relevant effects.

Initially, the onboard rotor test-rig supplied the first practical onboard dynamics data for the validation of simulation models. The controllable base movement provided by a shaker proved to be an important tool for the experimentation, permitting practical situations to be simulated in the laboratory. The composite-shaft test rig, featuring complex orthotropic material with considerable internal damping provided the next insight, this time on the material model itself. It allowed for the directional coupling and shear effects to be studied and for the SHBT material integration procedure to be analyzed and validated. Lastly, on the flywheel test-rig there were relevant phenomena observed and studied. The intentionally slender shaft with relatively massive flywheel attachment produced accentuated coupled dynamics, which in turn allowed for the validation and appraisal of the UF model capacities.

5.4 Future Perspectives

As a continuation of this research, the UF framework should be further expanded. The simple time constraints, necessary for the dissertation, limited the amount of work that could be dedicated to the problem and in turn how adaptable the UF methodology is. Should this work be continued, the author suggests two main issues:

1_{st} expanding the capabilities of the UF formulation for rotordynamics applications in a scientific manner. Focusing for example on: a) nonlinear models for the interpolation functions; b) dedicated elements to represent multi-part shafts and connections on a practical way, or; c) include the capacity to model greater deformations. This may improve the current understanding of the complex behavior of such machines;

2_{nd} developing the UF algorithm into a fully automated and numerical architecture for adaptable modeling and easy implementation for industrial applications. This may be achieved either via a standalone and independent software platform, or via integration with existing frameworks, in order to accelerate the development.

References

[1] M T S Alves. *Controle de Vibrações em Rotores Flexíveis usando Liga com Memória de Forma*. PhD thesis, Universidade Federal de Uberlândia, Uberlândia, Brasil, 2015.

[2] P C P F Barbosa, A A Cavalini Jr., and V Steffen Jr. *Analysis of the dynamic behavior of composite shafts on rotating machines*. PhD thesis, Universidade Federal de Uberlândia, Uberlândia, Brasil, 2018.

[3] P C P F Barbosa, V T S Del Claro, A A Cavalini Jr., and V Steffen Jr. A comparison between composite rotordynamics modeling theories. In *Proceedings of the 24th ABCM COBEM*, Curitiba, Brazil, 2017.

[4] P C P F Barbosa, V T S Del Claro, A A Cavalini Jr., and V Steffen Jr. Experimental analysis of the shbt approach for the dynamic modeling of a composite hollow shaft. *Composite Structures*, 236:111892, 2020. `doi:10.1016/j.compstruct.2020.111892`.

[5] P C P F Barbosa, V T S Del Claro, M S Sousa Jr., A A Cavalini Jr., and V Steffen Jr. Shbt based modeling of a composite hollow shaft regarding its dynamic behavior prediction. In *Proceedings of SIRM 2019 – 13th International Conference on Dynamics of Rotating Machines*, Copenhagen, Denmark, 2019.

[6] R E D Bishop. The vibration and balancing of an unbalanced flexible rotor. *J. Mech. Eng. Sci*, pages 66–77, 1959.

[7] R E D Bishop. Vibration of rotating shafts. *J. Mech. Eng. Sci*, pages 50–65, 1959.

[8] H F Black. Interaction of a whirling rotor with a vibration stator across a clearance. *J. Mech. Eng. Sci.*, pages 1–11, 1968.

[9] A S Borges. *Controle Modal de Rotores com Mancais Magnéticos – Projeto robusto*. PhD thesis, Universidade Federal de Uberlândia, Uberlândia, Brasil, 2016.

[10] S H Brosens and S H Crandall. Whirling of unsymmetrical rotors. *Trans. ASME, J. Appl. Mech.*, page 355–362, 1961.

[11] M Brush. Still spinning after all these years: A profile of the ultracentrifuge. *The Scientist*, 13:16–18, 1999.

[12] L L Bucciarelli. On the instability of rotating shafts due to internal damping. *Journal of Applied Mechanics*, 49:425–428, 1982. `doi:doi.org/10.1115/1.3162104`.

[13] E Carrera. Reissner-mindlin multilayered plate elements including zig-zag and interlaminar stresses continuity. *International Journal for Numerical Methods in Engineering*, pages 1797–1820, 1996. `doi:doi.org/10.1002/(SICI)1097-0207(19960615)39:11<1797::AID-NME928>3.0.CO;2-W`.

[14] E Carrera and M Filippi. Vibration analysis of thin/thick, composites/metallic spinning cylindrical shells by refined beam models. *ASME. J. Vib. Acoust*, 137:031020–1, 2015. `doi:10.1115/1.4029688`.

[15] E Carrera, M Filippi, and E Zappino. Free vibration analysis of rotating composite blades via carrera unified formulation. *Composite Structures*, 106:317–325, 2013. `doi:doi.org/10.1016/j.compstruct.2013.05.055`.

[16] E Carrera, G Giunta, and M Petrolo. *Beam Structures: Classical and Advanced Theories*. John Wiley & Sons, New Jersey, 1st edition edition, 2011.

[17] E Carrera, G Giunta, M Petrolo, and E Zappino. *Finite Element Analyses of Structures Through Unified Formulation*. John Wiley & Sons, New Jersey, 1st edition edition, 2014.

[18] A A Cavalini Jr. *Detection and Identification of Incipient Transversal Cracks in Flexible and Horizontal Shafts of Rotating Machines*. PhD thesis, Universidade Federal de Uberlândia, Uberlândia, Brasil, 2013.

[19] A A Cavalini Jr., T Guimarães, B R M G Da Silva, and V Steffen Jr. Analysis of the dynamic behavior of a rotating composite hollow shaft. *Latin American Journal of Solids and Structures*, 14:1–16, 2017. `doi:doi.org/10.1590/1679-78253168`.

[20] N A Dagnaes-Hansen and I F Santos. Magnetically suspended flywheel in gimbal mount - test bench design and experimental validation. *Journal of Sound and Vibration*, pages 197–210, 2019. `doi:10.1016/j.jsv.2019.01.023`.

[21] N A Dagnaes-Hansen and I F Santos. Permanent magnet thrust bearings for flywheel energy storage systems: Analytical, numerical, and experimental comparisons. *Proceedings of the Institution of Mechanical Engineers, Part C: Journal of Mechanical Engineering Science*, pages 5280–5293, 2019. `doi:10.1177/0954406219843952`.

[22] V T S Del Claro, P C P F Barbosa, A A Cavalini Jr., and V Steffen Jr. A shell based fem model for thick walled composite rotors. In *Proceedings of the 24th ABCM COBEM*, Curitiba, Brazil, 2017.

[23] V T S Del Claro, A A Cavalini Jr., I F Santos, and V Steffen Jr. N-th order unified formulation model for rotordynamics. *Proc. of COBEM, 25th ABCM International Congress of Mechanical Engineering*, pages 1048–1058, 2019.

[24] M Duchemin. *Contribuition A L'etude Du Comportement Dynamic D'un Rotor Embarque.* PhD thesis, Insa Lyon, Lyon, France, 2003.

[25] M Duchemin, A Berlioz, and G Ferraris. Dynamic behavior and stability of a rotor under base excitation. *Asme Journal of Vibration and Acoustics*, pages 128–576, 2006. `doi:doi.org/10.1115/1.2202159`.

[26] M Filippi. *A variable kinematic one-dimensional model for aeroelasticity and dynamic analysis of multi-layered rotors*. PhD thesis, Politecnico di Torino, Turin, Italy, 2015.

[27] R Gasch. Dynamic behaviour of a simple rotor with a cross-sectional crack. *Proceedings of the International Conference on Vibrations in Rotating Machinery*, page 123–128, 1976.

[28] H B H Gubran and K Gupta. The effect of stacking sequence and coupling mechanisms on the natural frequencies of composite shafts. *Journal of Sound and Vibrations*, pages 231–248, 2005. `doi:10.1016/j.jsv.2004.02.022`.

[29] K Gupta. Composite shaft rotor dynamics: An overview. In *Proceedings of Vibration Engineering and Technology of Machinery - Vetomac X*, Manchester, England, 2015.

[30] H H Jeffcott. The lateral vibration of loaded shafts in the neighborhood of a whirling speed: The effect of want of balance. *Philosophical Magazine*, pages 304–315, 1919.

[31] V Steffen Jr. Estudo analítico e experimental de dinâmica de rotores. *Revista Brasileira de Ciências Mecânicas*, pages 3–8, 1981.

[32] A L Kimball. Internal friction theory of shaft whirling. *General Electric Company*, pages 244–251, 1924.

[33] J A Kirk. Flywheel energy storage—i: Basic concepts. *International Journal of Mechanical Sciences*, pages 223–231, 1977. `doi:1977IJMeS..19..223K`.

[34] E H Koroishi. *Controle de Vibrações em Máquinas Rotativas utilizando Atuadores Eletromagnéticos*. PhD thesis, Universidade Federal de Uberlândia, Uberlândia, Brasil, 2013.

[35] M Lalanne and G Ferraris. *Rotordynamics Prediction in Engineering*. John Wiley and Sons, New York, 1st edition edition, 1998.

[36] W R P Mendonça, E Medeiros, A L R Pereira, and M H Mathias. The dynamic analysis of rotors mounted on composite shafts with internal damping. *Composite Structures*, pages 50–62, 2017. `doi:doi.org/10.1016/j.compstruct.2017.01.078`.

[37] T S Morais. *Contribuição ao Estudo de Máquinas Rotativas contendo não Linearidades*. PhD thesis, Universidade Federal de Uberlândia, Uberlândia, Brasil, 2010.

[38] B L Newkirk and H D Taylor. Shaft whirling due to oil action in journal bearings. *General Electric Company*, pages 559–568, 1924.

[39] K Nonami. Vibration control of a rotor by active bearings. *Trans. JSME*, page 2463–2472, 1985.

[40] M V F Oliveira. *Caracterização Numérica e Experimental de uma Bancada de Rotor Flexível Suportada por Mancais Magnéticos Ativos*. PhD thesis, Universidade Federal de Uberlândia, Uberlândia, Brasil, 2015.

[41] M A Prohl. A general method for calculating critical speeds of flexible rotors. *Journal of Applied Mechanics*, pages 142–148, 1945.

[42] W J M Rankine. On the centrifugal force of rotating shafts. *The Engineer, 27th Edition*, pages 249–249, 1869.

[43] R L Ruhl and J F Booker. A finite element model for distributed parameter turbo rotor system. *Trans. ASME, J. Eng. Ind.*, page 126–132, 1972.

[44] M V Saldarriaga. *Atenuação de Vibrações em Máquinas Rotativas Flexíveis usando Materiais Viscoelásticos nos Suportes*. PhD thesis, Universidade Federal de Uberlândia, Uberlândia, Brasil, 2007.

[45] I F Santos and F Y Watanabe. Lateral dynamics and stability of a gas compressor supported by hybrid and active lubricated multirecess journal bearings. *Journal of the Brazilian Society of Mechanical Science and Engineering*, pages 486–496, 2006. `doi:dx.doi.org/10.1590/S1678-58782006000400014`.

[46] G Schweitzer. Stabilization of self-excited rotor vibrations by active dampers. *Dynamics of Rotors*, page 472–493, 1975.

[47] L S Silva, P C P F Barbosa, A A Cavalini Jr., V Steffen Jr., and F A Lara-Molina. Analysis of the dynamic behavior of a composite hollow shaft considering uncertain and sensitivity information. *Proc. of COBEM, 25th ABCM International Congress of Mechanical Engineering*, 2019.

[48] M E Silveira. *Analise Do Comportamento Dinamico De Rotores Em Eixos Bobinados*. PhD thesis, Federal University of Santa Catarina, Florianopolis, Brazil, 2001.

[49] R C Simões. *Controle Modal Ótimo de um Rotor Flexível Utilizando Atuadores Piezelétricos do Tipo Pilha*. PhD thesis, Universidade Federal de Uberlândia, Uberlândia, Brasil, 2006.

[50] S P Singh and K Gupta. Composite shaft rotordynamic analysis using a layerwise theory. *Journal of Sound and Vibration*, pages 739–756, 1996. `doi:10.1006/jsvi.1996.0153`.

[51] R Sino. *Comportement Dynamique Et Stabilite Des Rotors: Application Aux Rotors Composites*. PhD thesis, Insa Lyon, Lyon, France, 2007.

[52] R Sino, A B Baranger, and A G Jacquet. Dynamic analysis of a rotating composite shaft. *Composites Science and Technology*, page 337–345, 2008. `doi:10.1016/j.compscitech.2007.06.019`.

[53] D M Smith. The motion of a rotor carried by a flexible shaft in flexible bearings. *Proceedings of the Royal Society of London*, pages 92–118, 1933.

[54] M S Sousa Jr. *Analysis of the Dynamic Behavior of Onboard Rotor*. PhD thesis, Universidade Federal de Uberlândia, Uberlândia, Brasil, 2017a.

[55] M S Sousa Jr., V T S Del Claro, A A Cavalini Jr., and V Steffen Jr. Experimental validation of an onboard rotor fem model. In *Proceedings of COBEM 2017 – 24th International Congress of Mechanical Engineering*, Curitiba, Brazil, 2017.

[56] M S Sousa Jr., V T S Del Claro, A A Cavalini Jr., and V Steffen Jr. Numerical investigation on the dynamic behavior of an onboard rotor system by using the fem approach. *Journal of the Brazilian Society for Mechanical Sciences and Engineering*, pages 2447–2458, 2017b. `doi:doi.org/10.1007/s40430-016-0640-5`.

[57] A Stodola. Dampf und gas-turbinen. *Verlag von Julius Springer*, 1924.

[58] E L Thearle. Dynamic balancing in the field. *Transactions of the ASME Journal of Applied Mechanics*, pages 745–753, 1934.

[59] S W Tsai. *Composites Design*. Dayton, Ohio, USA, 4th edition edition, 1998.

[60] C M Wasilkoski. *Mechanical Behavior of Composite Materials*. PhD thesis, UFPR, Curitiba, Brasil, 2006.

[61] T Yamamoto. On the critical speed of a shaft of sub-harmonic oscillation. *Trans. JSME*, pages 853–858, 1955.

[62] T Yamamoto and Y Ishida. *Linear and Nonlinear Rotordynamics, A Modern Treatment with Applications*. Wiley-VCH Verlag & Company, Weinheim, Germany, 2nd edition edition, 2012.

[63] E Zappino. *Variable kinematic 1D, 2D and 3D models for the Analysis of Aerospace Structures*. PhD thesis, Politecnico di Torino, Turin, Italy, 2014.

[64] O C Zienkiewicz and R L Taylor. *The Finite Element Method for Solid and Structural Mechanics*. Elsevier, New York, 5th edition edition, 2005.

Appendix A

Schematics for the flywheel test-rig

The detailed mechanical design of the flywheel test-rig is now presented. This is the final manufacture design, as produced by the Mechanical Workshop staff at DTU Mekanik. The external components, such as bearings, sleeves, bolts, etc. are identified and listed in the following.

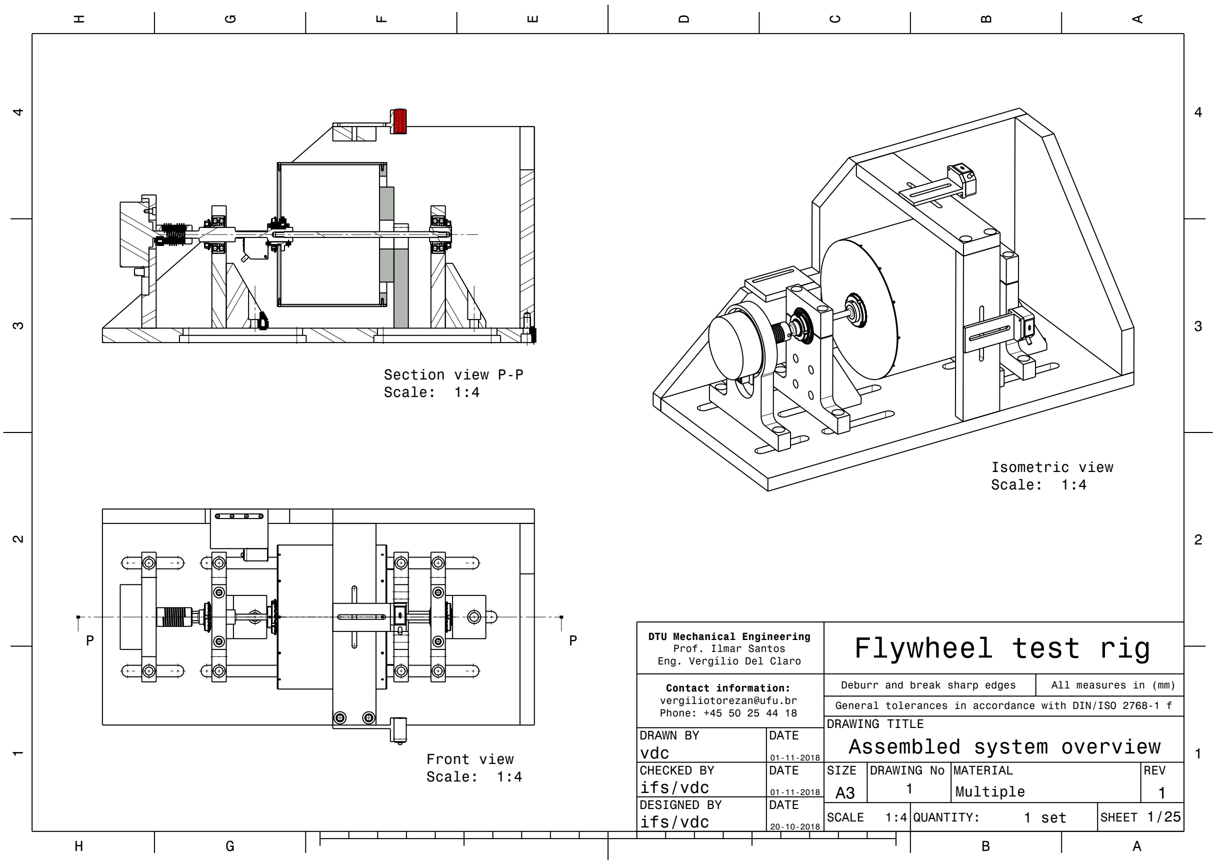

DTU Mechanical Engineering
Prof. Ilmar Santos
Eng. Vergílio Del Claro

Contact information:
vergiliotorezan@ufu.br
Phone: +45 50 25 44 18

Flywheel test rig

Deburr and break sharp edges | All measures in (mm)
General tolerances in accordance with DIN/ISO 2768-1 f

DRAWN BY vdc	DATE 01-11-2018	DRAWING TITLE Assembled system overview			
CHECKED BY ifs/vdc	DATE 01-11-2018	SIZE A3	DRAWING No 1	MATERIAL Multiple	REV 1
DESIGNED BY ifs/vdc	DATE 20-10-2018	SCALE 1:4	QUANTITY: 1 set		SHEET 1/25

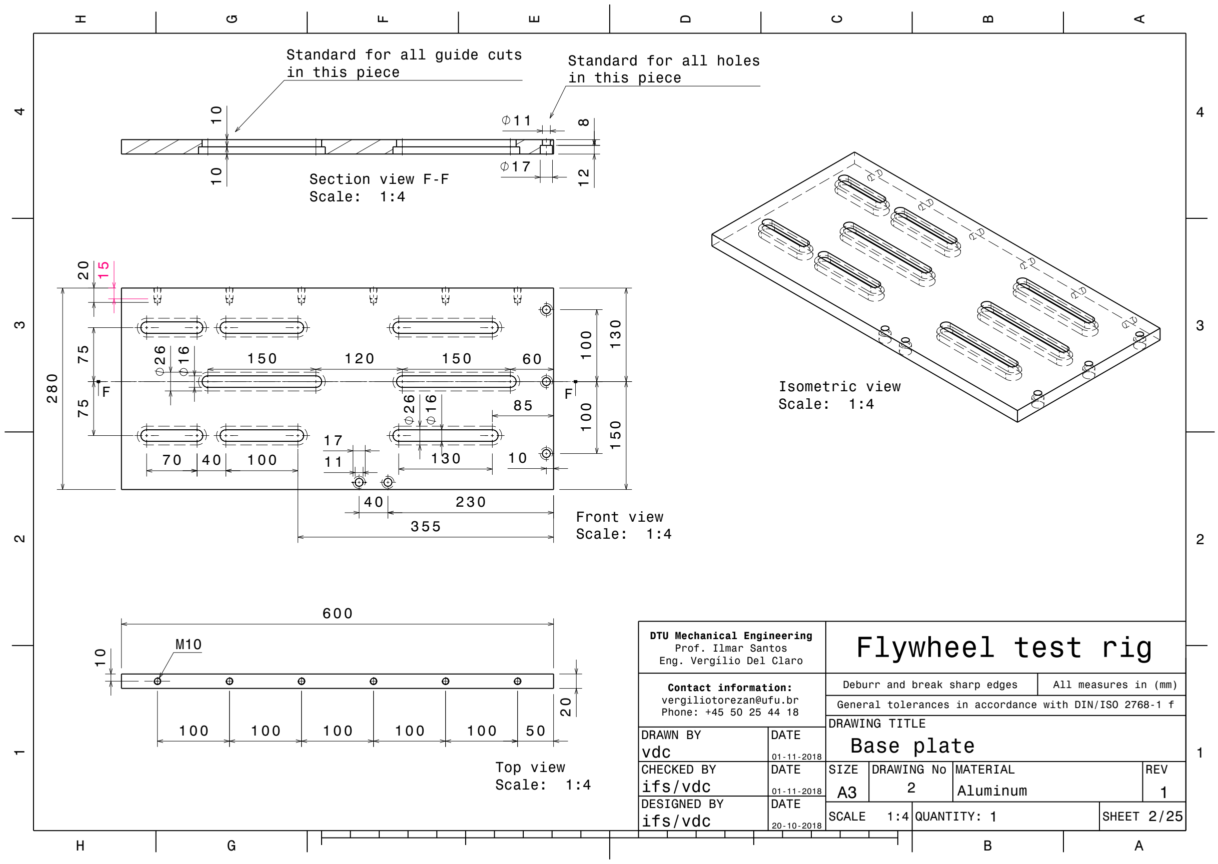
Standard for all guide cuts in this piece
Standard for all holes in this piece
Ø11
Ø17
8
12
10
10
Section view F-F
Scale: 1:4
Isometric view
Scale: 1:4
20
15
280
75
75
F
F
Ø26
Ø16
150
120
150
60
100
130
100
150
85
17
11
70
40
100
130
10
40
230
355
Front view
Scale: 1:4
600
M10
10
20
100
100
100
100
100
50
Top view
Scale: 1:4
DTU Mechanical Engineering
Prof. Ilmar Santos
Eng. Vergilio Del Claro
Flywheel test rig
Contact information:
vergiliotorezan@ufu.br
Phone: +45 50 25 44 18
Deburr and break sharp edges
All measures in (mm)
General tolerances in accordance with DIN/ISO 2768-1 f
DRAWING TITLE
Base plate
DRAWN BY vdc
DATE 01-11-2018
CHECKED BY ifs/vdc
DATE 01-11-2018
DESIGNED BY ifs/vdc
DATE 20-10-2018
SIZE A3
DRAWING No 2
MATERIAL Aluminum
REV 1
SCALE 1:4
QUANTITY: 1
SHEET 2/25
H G F E D C B A
4 3 2 1

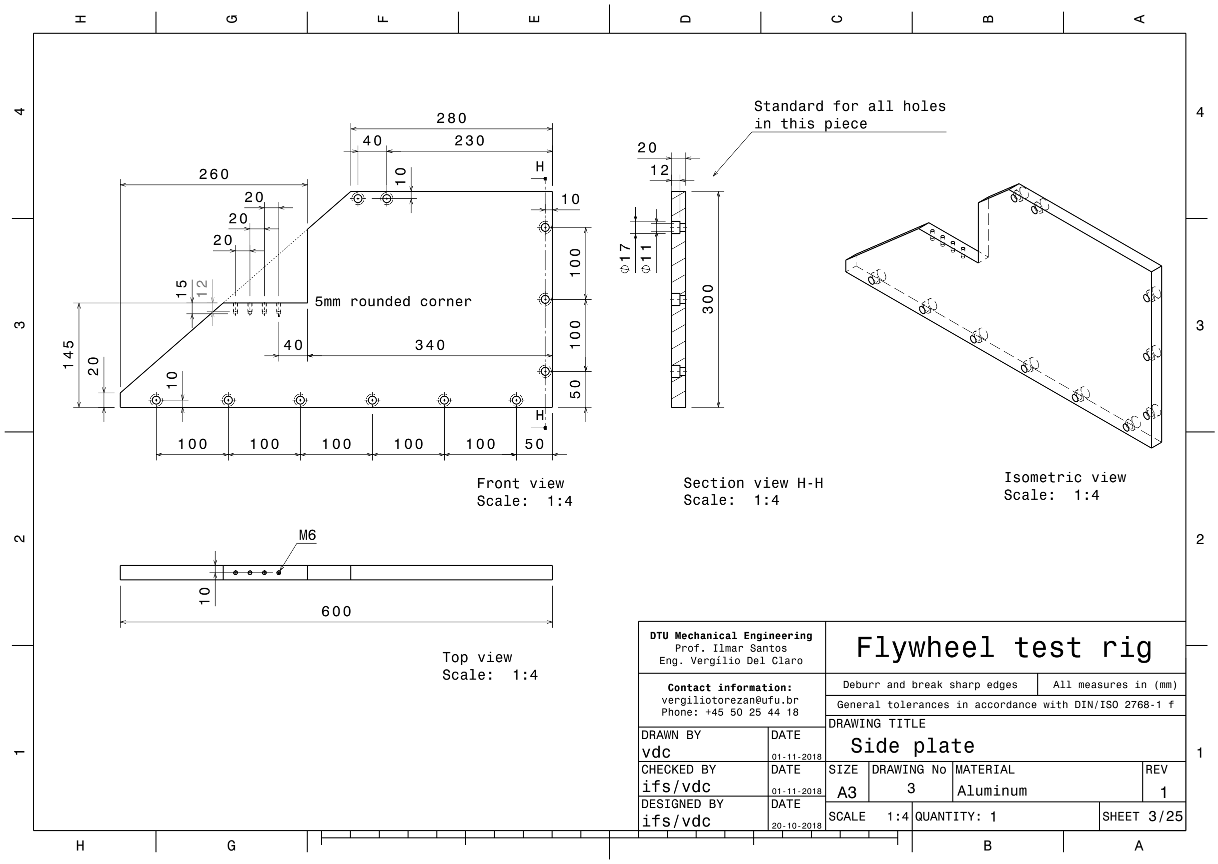
Standard for all holes in this piece
280
40
230
260
10
H
20
20
20
15
12
10
5mm rounded corner
40
340
100
100
50
145
20
10
100
100
100
100
100
50
H
Front view
Scale: 1:4
20
12
Ø17
Ø11
300
Section view H-H
Scale: 1:4
Isometric view
Scale: 1:4
M6
10
600
Top view
Scale: 1:4
DTU Mechanical Engineering
Prof. Ilmar Santos
Eng. Vergilio Del Claro
Flywheel test rig
Contact information:
vergiliotorezan@ufu.br
Phone: +45 50 25 44 18
Deburr and break sharp edges
All measures in (mm)
General tolerances in accordance with DIN/ISO 2768-1 f
DRAWING TITLE
Side plate
DRAWN BY vdc
DATE 01-11-2018
CHECKED BY ifs/vdc
DATE 01-11-2018
DESIGNED BY ifs/vdc
DATE 20-10-2018
SIZE A3
DRAWING No 3
MATERIAL Aluminum
REV 1
SCALE 1:4
QUANTITY: 1
SHEET 3/25
H G F E D C B A
4 3 2 1

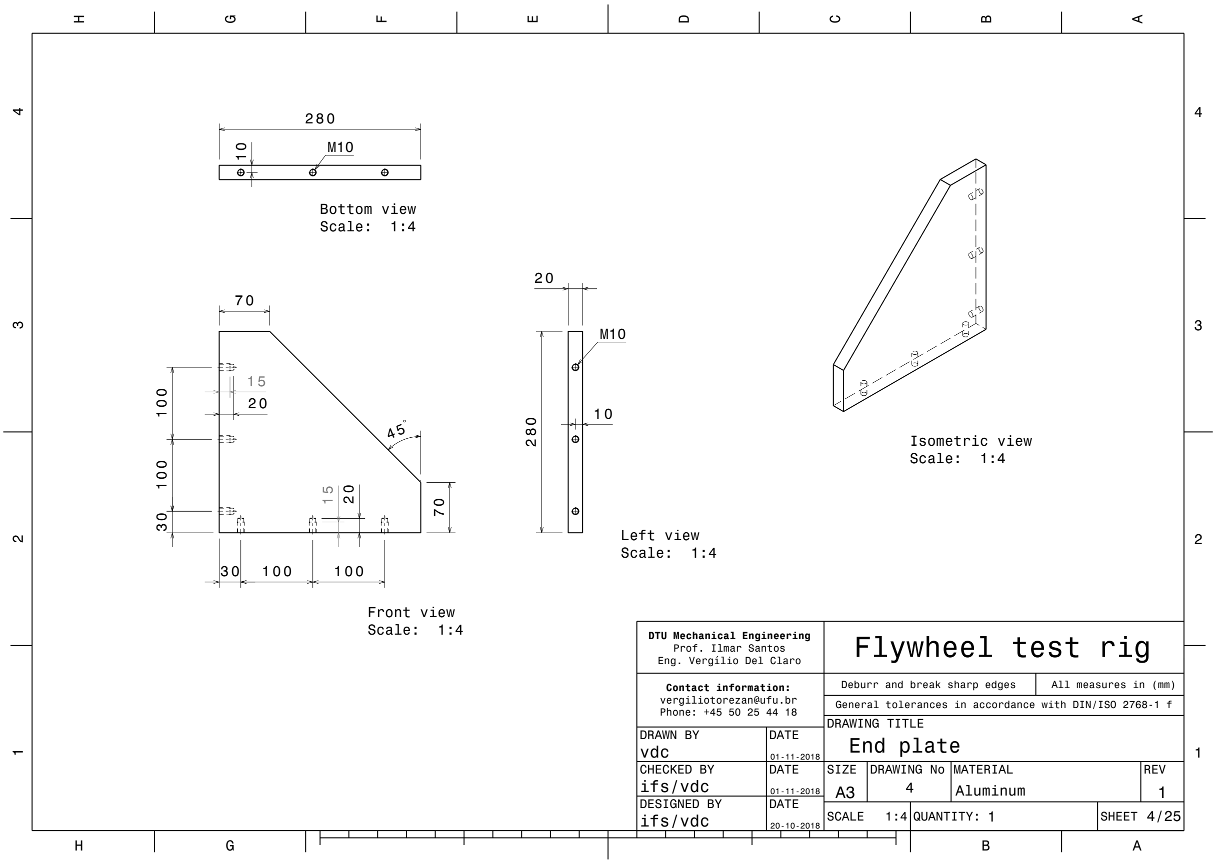

DTU Mechanical Engineering
Prof. Ilmar Santos
Eng. Vergílio Del Claro

Contact information:
vergiliotorezan@ufu.br
Phone: +45 50 25 44 18

Flywheel test rig

Deburr and break sharp edges | All measures in (mm)
General tolerances in accordance with DIN/ISO 2768-1 f

DRAWING TITLE: End plate
DRAWN BY: vdc | DATE: 01-11-2018
CHECKED BY: ifs/vdc | DATE: 01-11-2018
DESIGNED BY: ifs/vdc | DATE: 20-10-2018
SIZE: A3 | DRAWING No: 4 | MATERIAL: Aluminum | REV: 1
SCALE: 1:4 | QUANTITY: 1 | SHEET 4/25

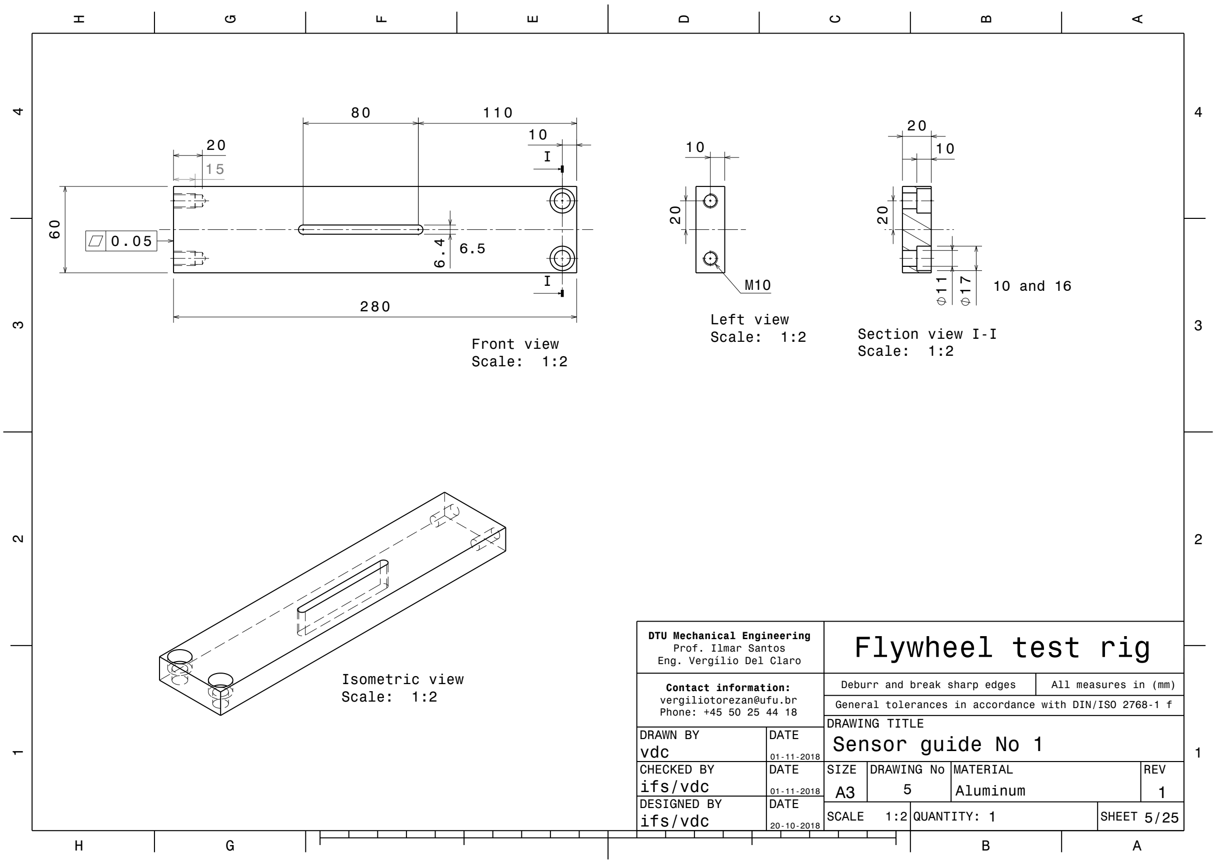

DTU Mechanical Engineering
Prof. Ilmar Santos
Eng. Vergílio Del Claro

Contact information:
vergiliotorezan@ufu.br
Phone: +45 50 25 44 18

Flywheel test rig

Deburr and break sharp edges | All measures in (mm)
General tolerances in accordance with DIN/ISO 2768-1 f

DRAWING TITLE: Sensor guide No 1
DRAWN BY: vdc | DATE: 01-11-2018
CHECKED BY: ifs/vdc | DATE: 01-11-2018
DESIGNED BY: ifs/vdc | DATE: 20-10-2018
SIZE: A3 | DRAWING No: 5 | MATERIAL: Aluminum | REV: 1
SCALE: 1:2 | QUANTITY: 1 | SHEET 5/25

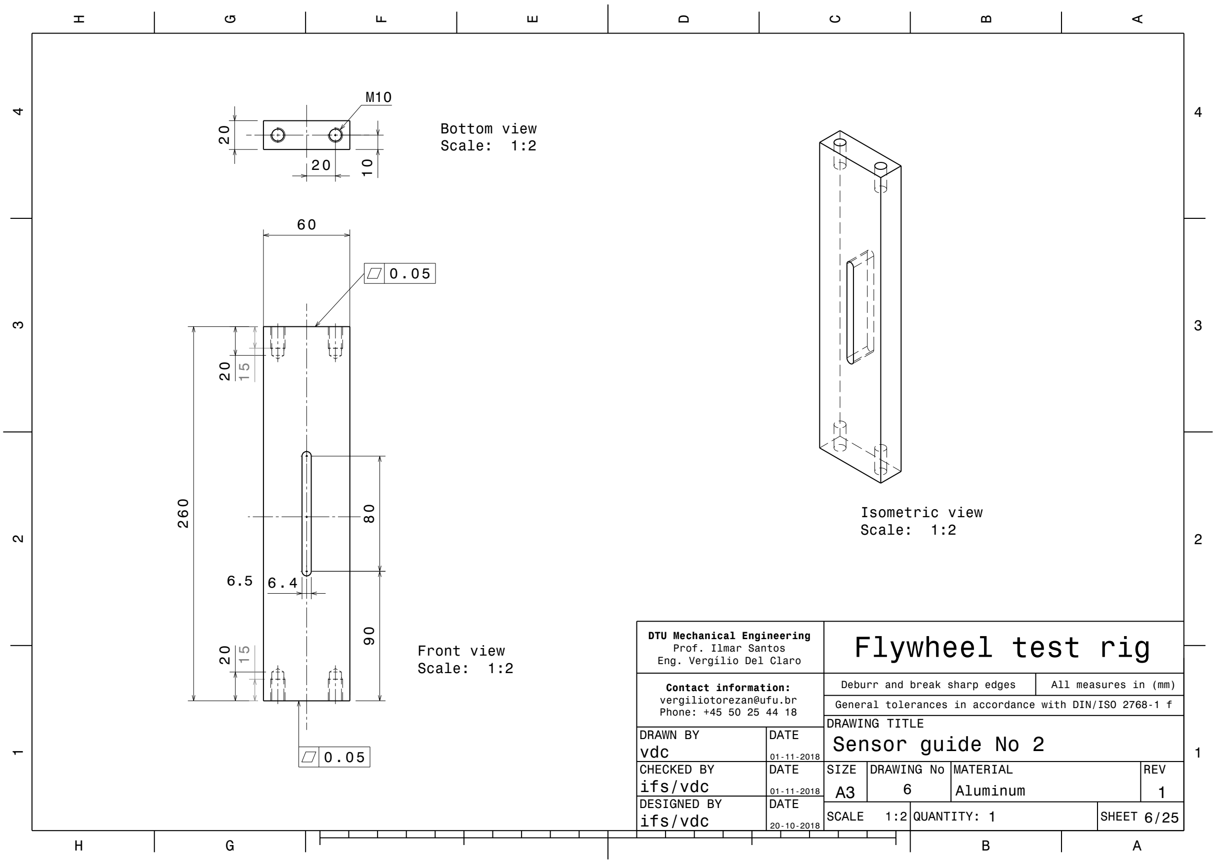
M10
Bottom view
Scale: 1:2
20
20
10
60
0.05
20
15
260
80
6.5
6.4
90
20
15
0.05
Front view
Scale: 1:2
Isometric view
Scale: 1:2
DTU Mechanical Engineering
Prof. Ilmar Santos
Eng. Vergilio Del Claro
Contact information:
vergiliotorezan@ufu.br
Phone: +45 50 25 44 18
Flywheel test rig
Deburr and break sharp edges
All measures in (mm)
General tolerances in accordance with DIN/ISO 2768-1 f
DRAWING TITLE
Sensor guide No 2
DRAWN BY
vdc
DATE
01-11-2018
CHECKED BY
ifs/vdc
DATE
01-11-2018
DESIGNED BY
ifs/vdc
DATE
20-10-2018
SIZE
A3
DRAWING No
6
MATERIAL
Aluminum
REV
1
SCALE 1:2
QUANTITY: 1
SHEET 6/25
H
G
F
E
D
C
B
A
1
2
3
4

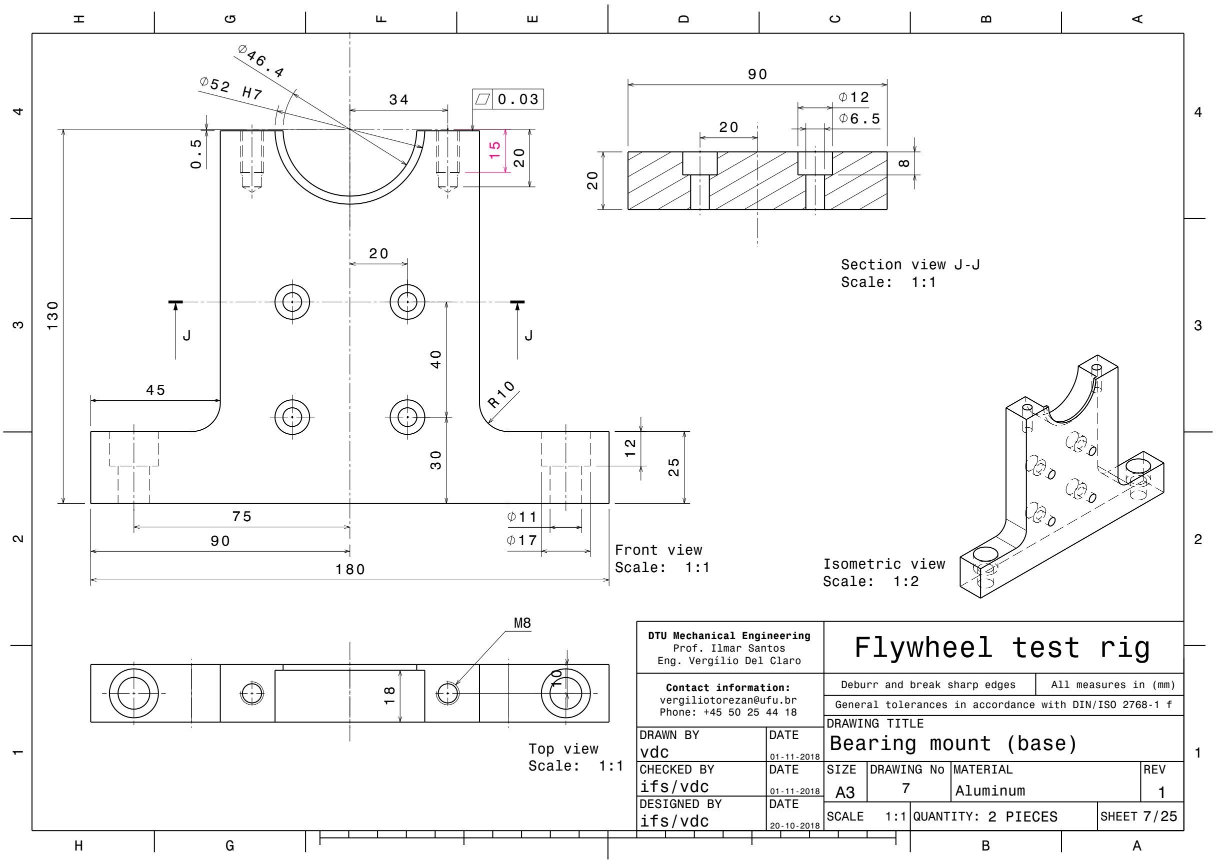
⌀46.4
⌀52 H7
34
0.03
0.5
15
20
130
20
J
J
40
R10
45
30
12
25
75
90
180
⌀11
⌀17
Front view
Scale: 1:1
90
⌀12
⌀6.5
20
20
8
Section view J-J
Scale: 1:1
Isometric view
Scale: 1:2
M8
18
10
Top view
Scale: 1:1
DTU Mechanical Engineering
Prof. Ilmar Santos
Eng. Vergilio Del Claro
Contact information:
vergiliotorezan@ufu.br
Phone: +45 50 25 44 18
Flywheel test rig
Deburr and break sharp edges
All measures in (mm)
General tolerances in accordance with DIN/ISO 2768-1 f
DRAWING TITLE
Bearing mount (base)
DRAWN BY
vdc
DATE
01-11-2018
CHECKED BY
ifs/vdc
DATE
01-11-2018
DESIGNED BY
ifs/vdc
DATE
20-10-2018
SIZE
A3
DRAWING No
7
MATERIAL
Aluminum
REV
1
SCALE 1:1
QUANTITY: 2 PIECES
SHEET 7/25
H
G
F
E
D
C
B
A
1
2
3
4

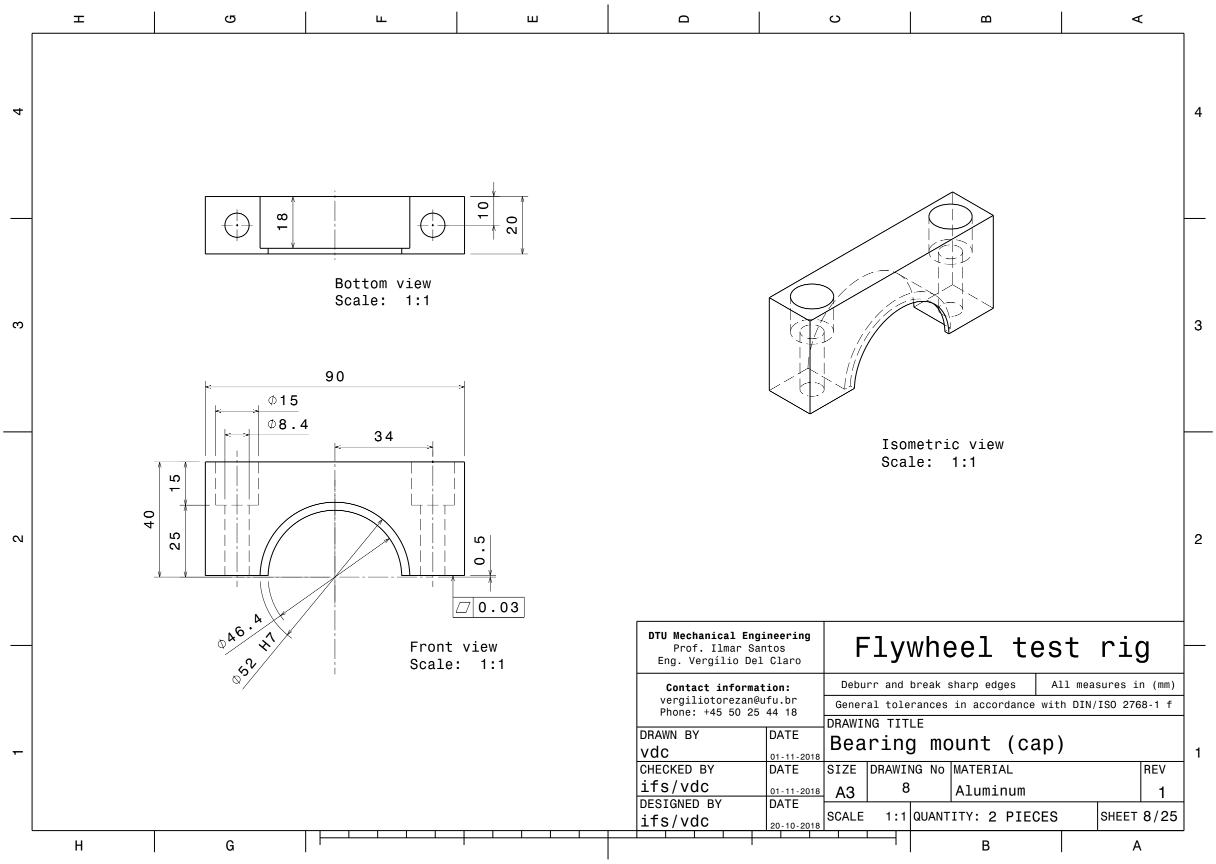

DTU Mechanical Engineering
Prof. Ilmar Santos
Eng. Vergílio Del Claro

Contact information:
vergiliotorezan@ufu.br
Phone: +45 50 25 44 18

Flywheel test rig

Deburr and break sharp edges | All measures in (mm)
General tolerances in accordance with DIN/ISO 2768-1 f

DRAWING TITLE: Bearing mount (cap)
DRAWN BY: vdc | DATE: 01-11-2018
CHECKED BY: ifs/vdc | DATE: 01-11-2018
DESIGNED BY: ifs/vdc | DATE: 20-10-2018
SIZE: A3 | DRAWING No: 8 | MATERIAL: Aluminum | REV: 1
SCALE: 1:1 | QUANTITY: 2 PIECES | SHEET 8/25

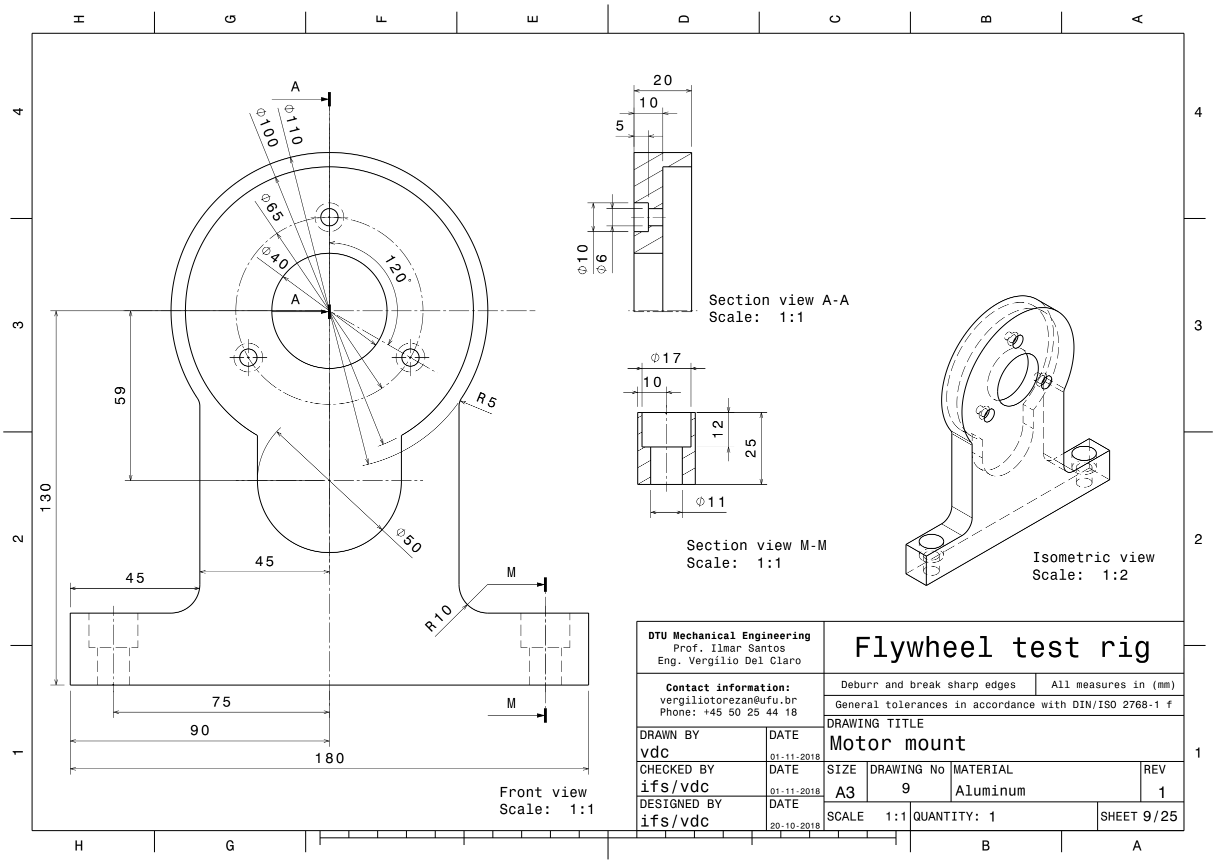

DTU Mechanical Engineering
Prof. Ilmar Santos
Eng. Vergílio Del Claro

Contact information:
vergiliotorezan@ufu.br
Phone: +45 50 25 44 18

Flywheel test rig

Deburr and break sharp edges | All measures in (mm)
General tolerances in accordance with DIN/ISO 2768-1 f

DRAWING TITLE: Motor mount
DRAWN BY: vdc | DATE: 01-11-2018
CHECKED BY: ifs/vdc | DATE: 01-11-2018
DESIGNED BY: ifs/vdc | DATE: 20-10-2018
SIZE: A3 | DRAWING No: 9 | MATERIAL: Aluminum | REV: 1
SCALE: 1:1 | QUANTITY: 1 | SHEET 9/25

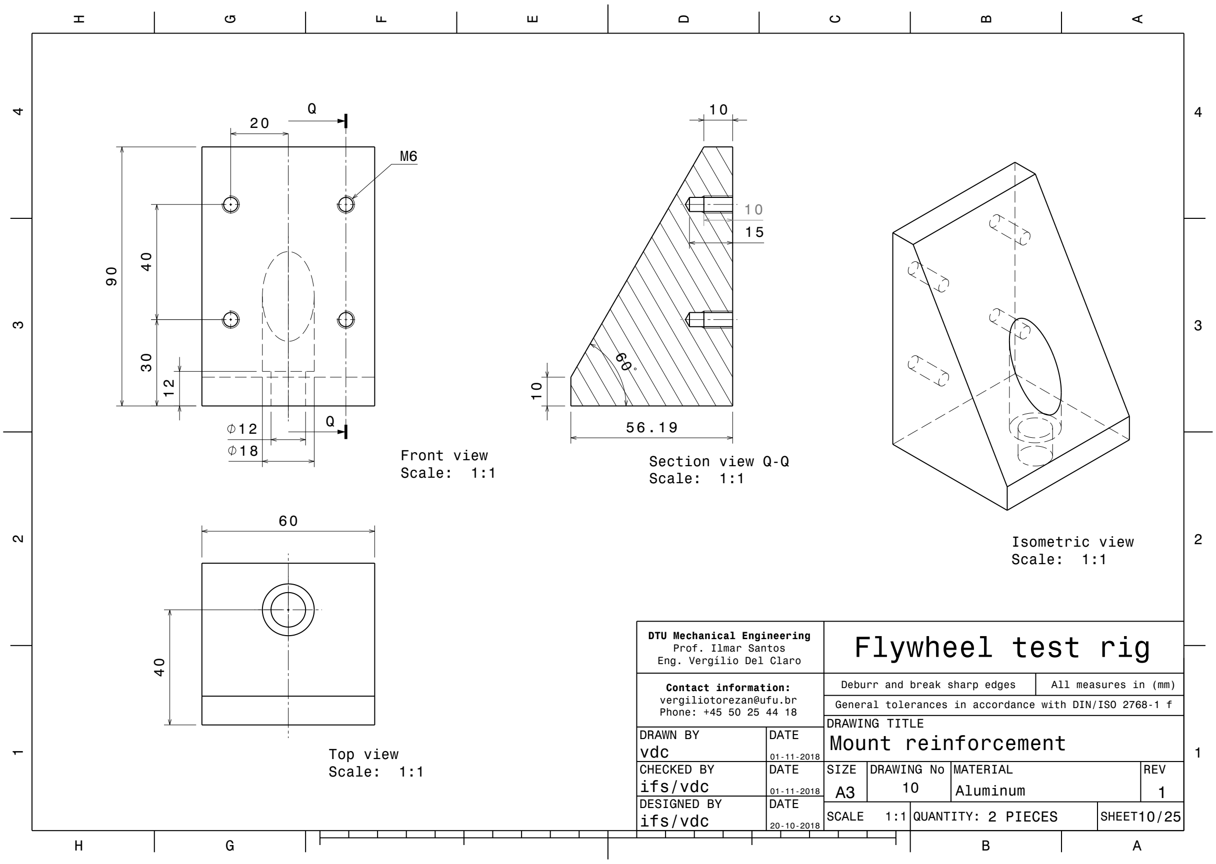

DTU Mechanical Engineering
Prof. Ilmar Santos
Eng. Vergilio Del Claro

Flywheel test rig

Contact information:
vergiliotorezan@ufu.br
Phone: +45 50 25 44 18

Deburr and break sharp edges | All measures in (mm)
General tolerances in accordance with DIN/ISO 2768-1 f

DRAWING TITLE
Mount reinforcement

DRAWN BY vdc | DATE 01-11-2018
CHECKED BY ifs/vdc | DATE 01-11-2018
DESIGNED BY ifs/vdc | DATE 20-10-2018

SIZE A3 | DRAWING No 10 | MATERIAL Aluminum | REV 1
SCALE 1:1 | QUANTITY: 2 PIECES | SHEET 10/25

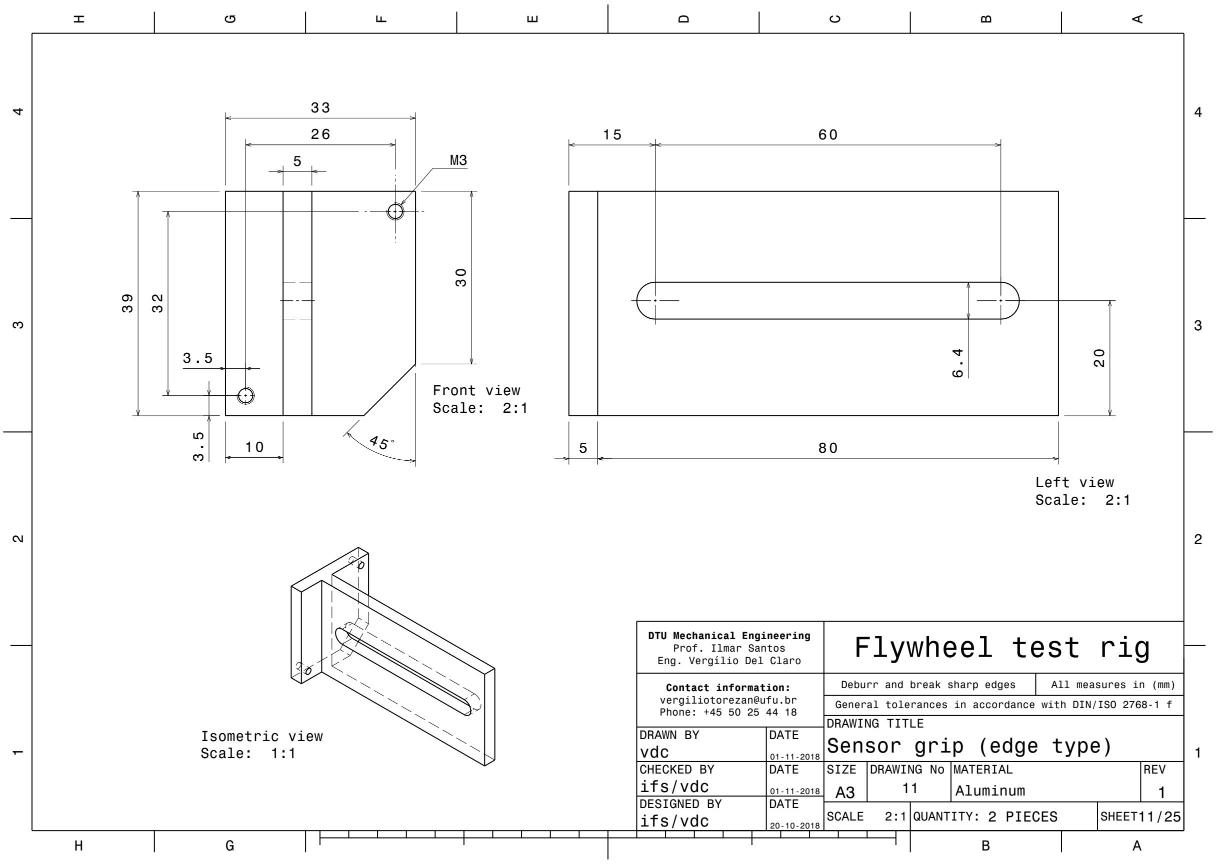

DTU Mechanical Engineering
Prof. Ilmar Santos
Eng. Vergilio Del Claro

Flywheel test rig

Contact information:
vergiliotorezan@ufu.br
Phone: +45 50 25 44 18

Deburr and break sharp edges | All measures in (mm)
General tolerances in accordance with DIN/ISO 2768-1 f

DRAWING TITLE
Sensor grip (edge type)

DRAWN BY vdc | DATE 01-11-2018
CHECKED BY ifs/vdc | DATE 01-11-2018
DESIGNED BY ifs/vdc | DATE 20-10-2018

SIZE A3 | DRAWING No 11 | MATERIAL Aluminum | REV 1
SCALE 2:1 | QUANTITY: 2 PIECES | SHEET 11/25

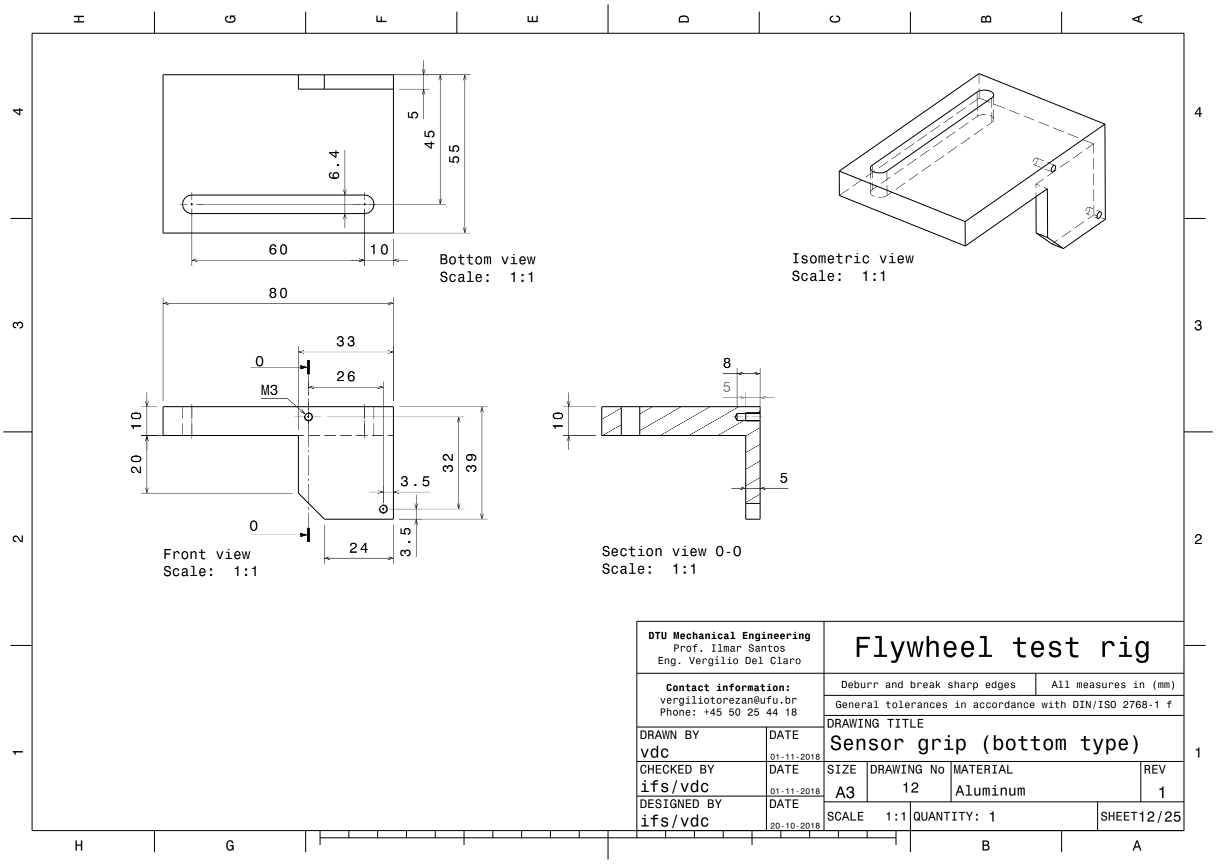

DTU Mechanical Engineering
Prof. Ilmar Santos
Eng. Vergílio Del Claro

Flywheel test rig

Contact information:
vergiliotorezan@ufu.br
Phone: +45 50 25 44 18

Deburr and break sharp edges | All measures in (mm)
General tolerances in accordance with DIN/ISO 2768-1 f

DRAWING TITLE: Sensor grip (bottom type)
DRAWN BY: vdc | DATE: 01-11-2018
CHECKED BY: ifs/vdc | DATE: 01-11-2018
DESIGNED BY: ifs/vdc | DATE: 20-10-2018
SIZE: A3 | DRAWING No: 12 | MATERIAL: Aluminum | REV: 1
SCALE: 1:1 | QUANTITY: 1 | SHEET 12/25

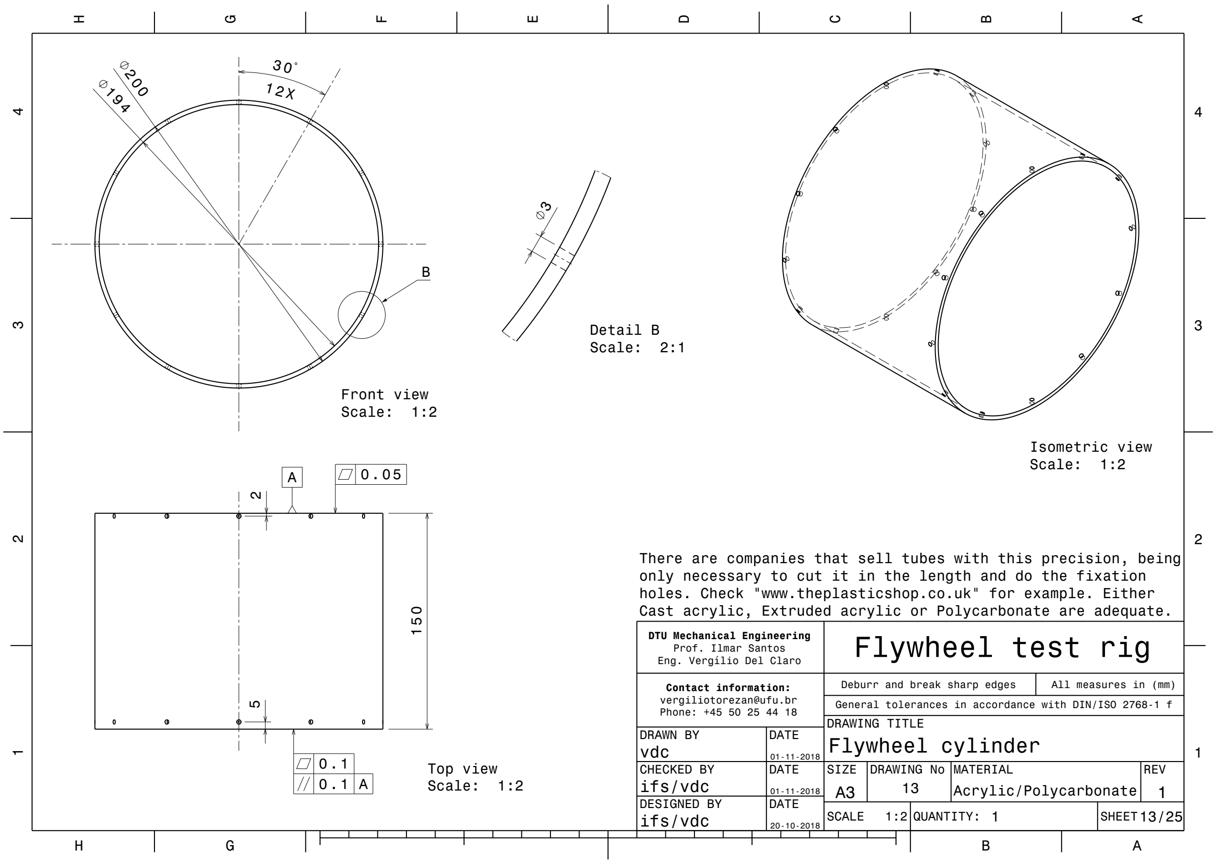

There are companies that sell tubes with this precision, being only necessary to cut it in the length and do the fixation holes. Check "www.theplasticshop.co.uk" for example. Either Cast acrylic, Extruded acrylic or Polycarbonate are adequate.

DTU Mechanical Engineering
Prof. Ilmar Santos
Eng. Vergílio Del Claro

Flywheel test rig

Contact information:
vergiliotorezan@ufu.br
Phone: +45 50 25 44 18

Deburr and break sharp edges | All measures in (mm)
General tolerances in accordance with DIN/ISO 2768-1 f

DRAWING TITLE: Flywheel cylinder
DRAWN BY: vdc | DATE: 01-11-2018
CHECKED BY: ifs/vdc | DATE: 01-11-2018
DESIGNED BY: ifs/vdc | DATE: 20-10-2018
SIZE: A3 | DRAWING No: 13 | MATERIAL: Acrylic/Polycarbonate | REV: 1
SCALE: 1:2 | QUANTITY: 1 | SHEET 13/25

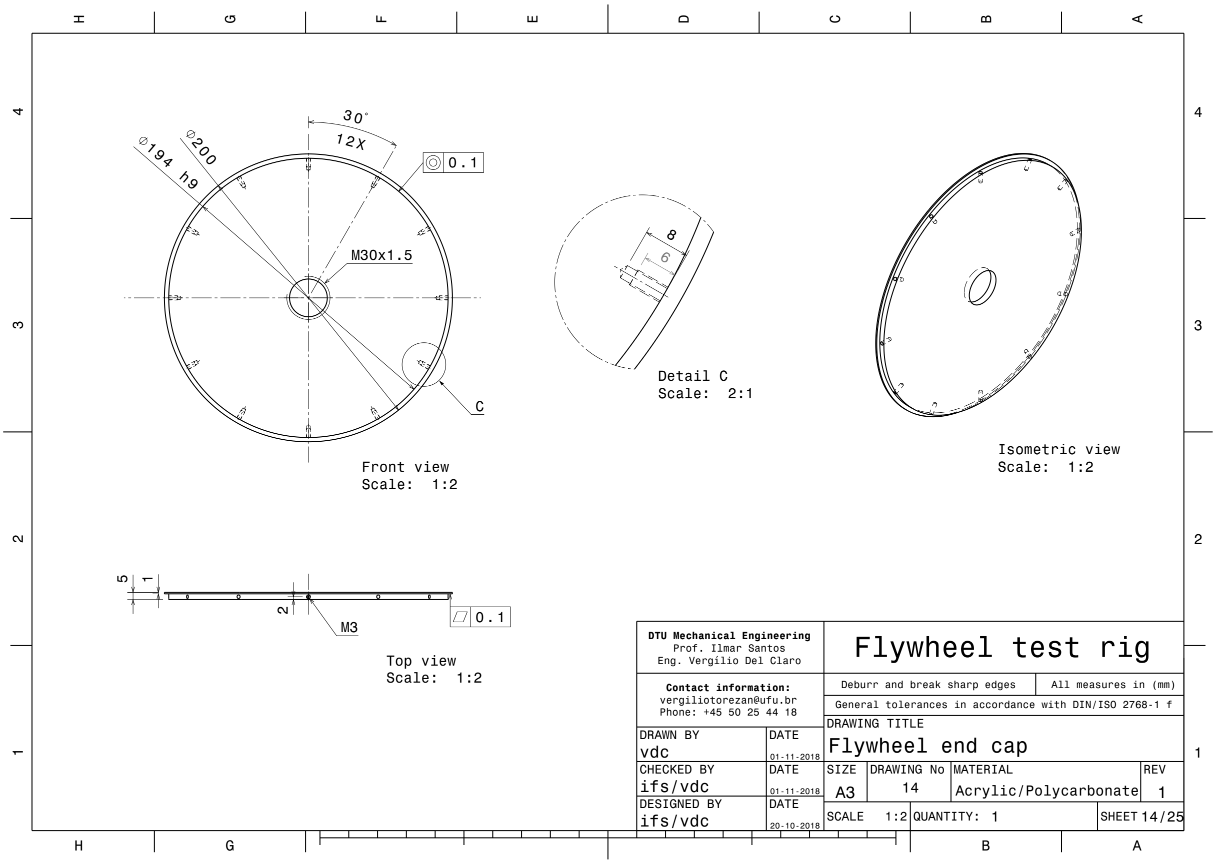

DTU Mechanical Engineering
Prof. Ilmar Santos
Eng. Vergilio Del Claro

Flywheel test rig

Contact information:
vergiliotorezan@ufu.br
Phone: +45 50 25 44 18

Deburr and break sharp edges | All measures in (mm)
General tolerances in accordance with DIN/ISO 2768-1 f

DRAWN BY vdc	DATE 01-11-2018	DRAWING TITLE Flywheel end cap			
CHECKED BY ifs/vdc	DATE 01-11-2018	SIZE A3	DRAWING No 14	MATERIAL Acrylic/Polycarbonate	REV 1
DESIGNED BY ifs/vdc	DATE 20-10-2018	SCALE 1:2		QUANTITY: 1	SHEET 14/25

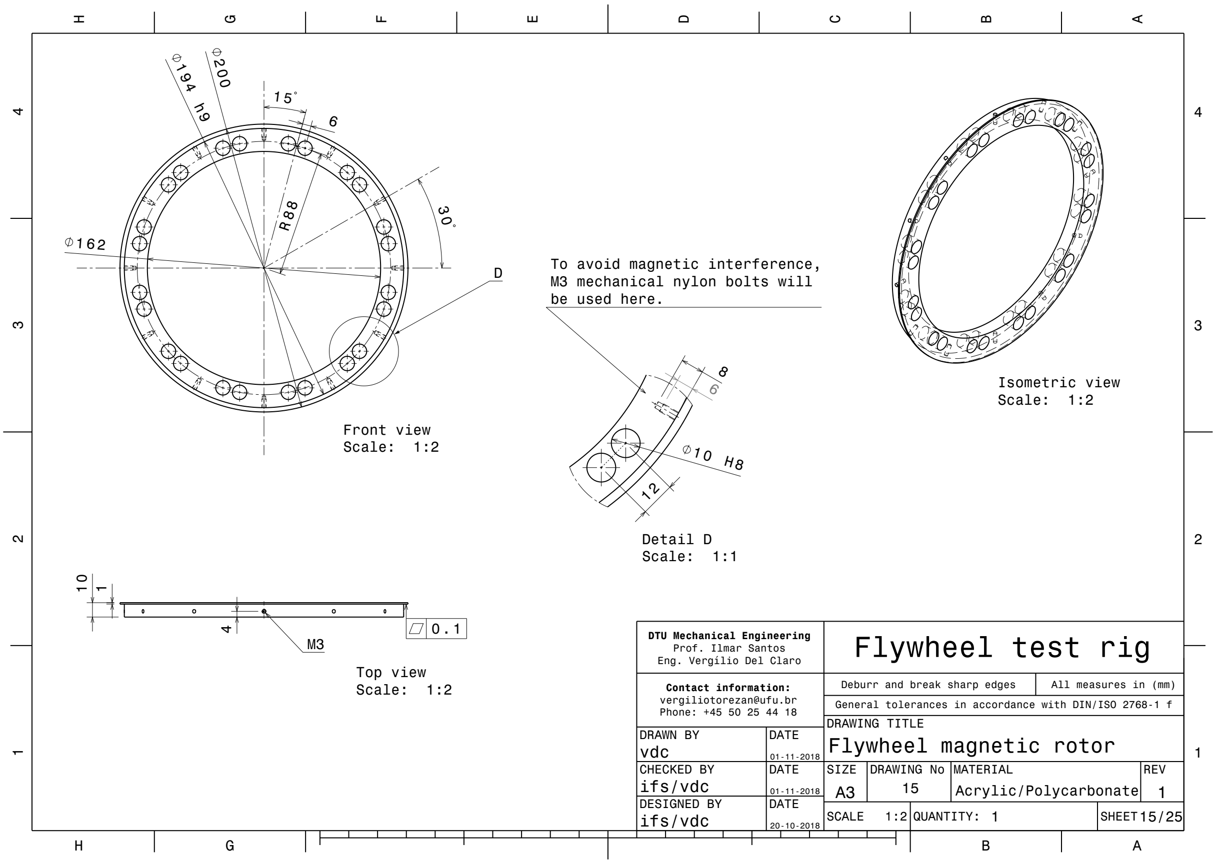

To avoid magnetic interference, M3 mechanical nylon bolts will be used here.

DTU Mechanical Engineering
Prof. Ilmar Santos
Eng. Vergilio Del Claro

Flywheel test rig

Contact information:
vergiliotorezan@ufu.br
Phone: +45 50 25 44 18

Deburr and break sharp edges | All measures in (mm)
General tolerances in accordance with DIN/ISO 2768-1 f

DRAWN BY vdc	DATE 01-11-2018	DRAWING TITLE Flywheel magnetic rotor			
CHECKED BY ifs/vdc	DATE 01-11-2018	SIZE A3	DRAWING No 15	MATERIAL Acrylic/Polycarbonate	REV 1
DESIGNED BY ifs/vdc	DATE 20-10-2018	SCALE 1:2		QUANTITY: 1	SHEET 15/25

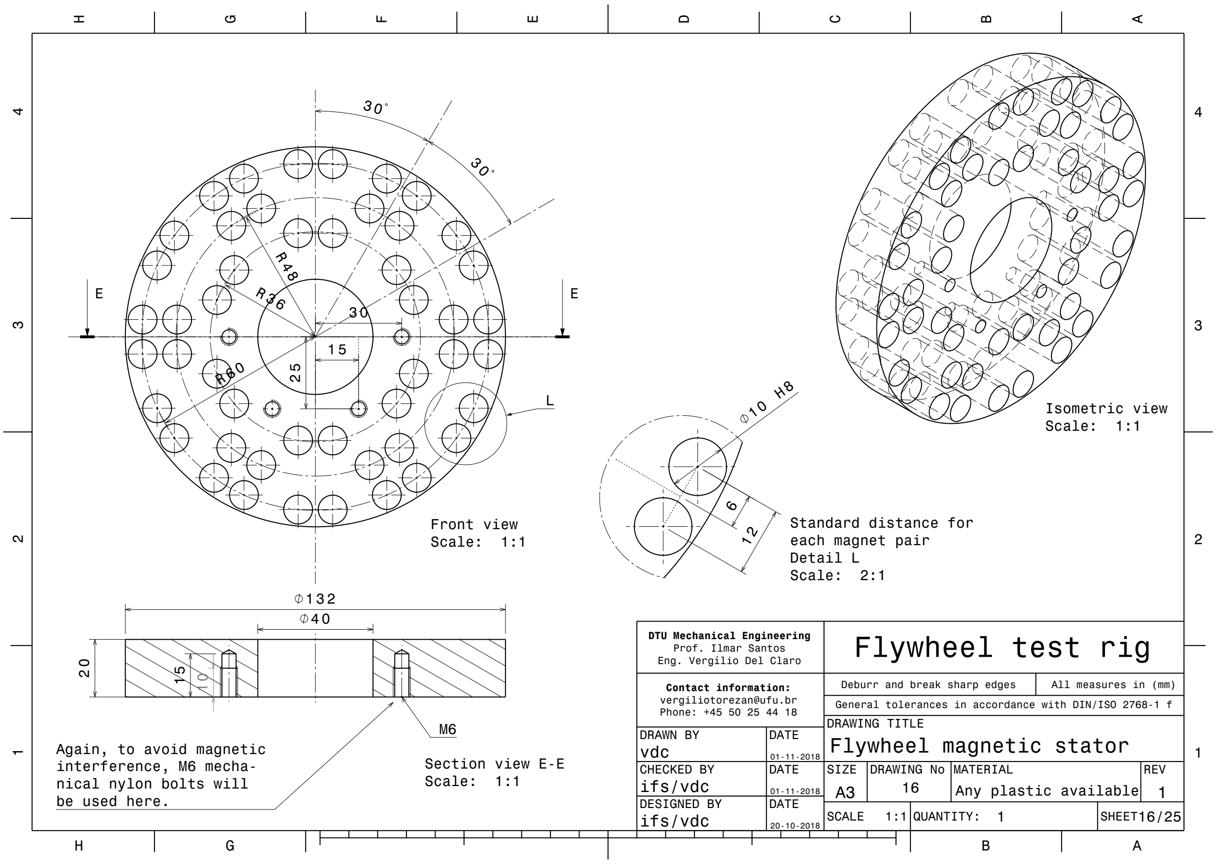

Again, to avoid magnetic interference, M6 mechanical nylon bolts will be used here.

DTU Mechanical Engineering
Prof. Ilmar Santos
Eng. Vergílio Del Claro

Contact information:
vergiliotorezan@ufu.br
Phone: +45 50 25 44 18

Flywheel test rig

Deburr and break sharp edges — All measures in (mm)
General tolerances in accordance with DIN/ISO 2768-1 f

DRAWING TITLE: Flywheel magnetic stator

DRAWN BY vdc	DATE 01-11-2018				
CHECKED BY ifs/vdc	DATE 01-11-2018	SIZE A3	DRAWING No 16	MATERIAL Any plastic available	REV 1
DESIGNED BY ifs/vdc	DATE 20-10-2018	SCALE 1:1	QUANTITY: 1		SHEET 16/25

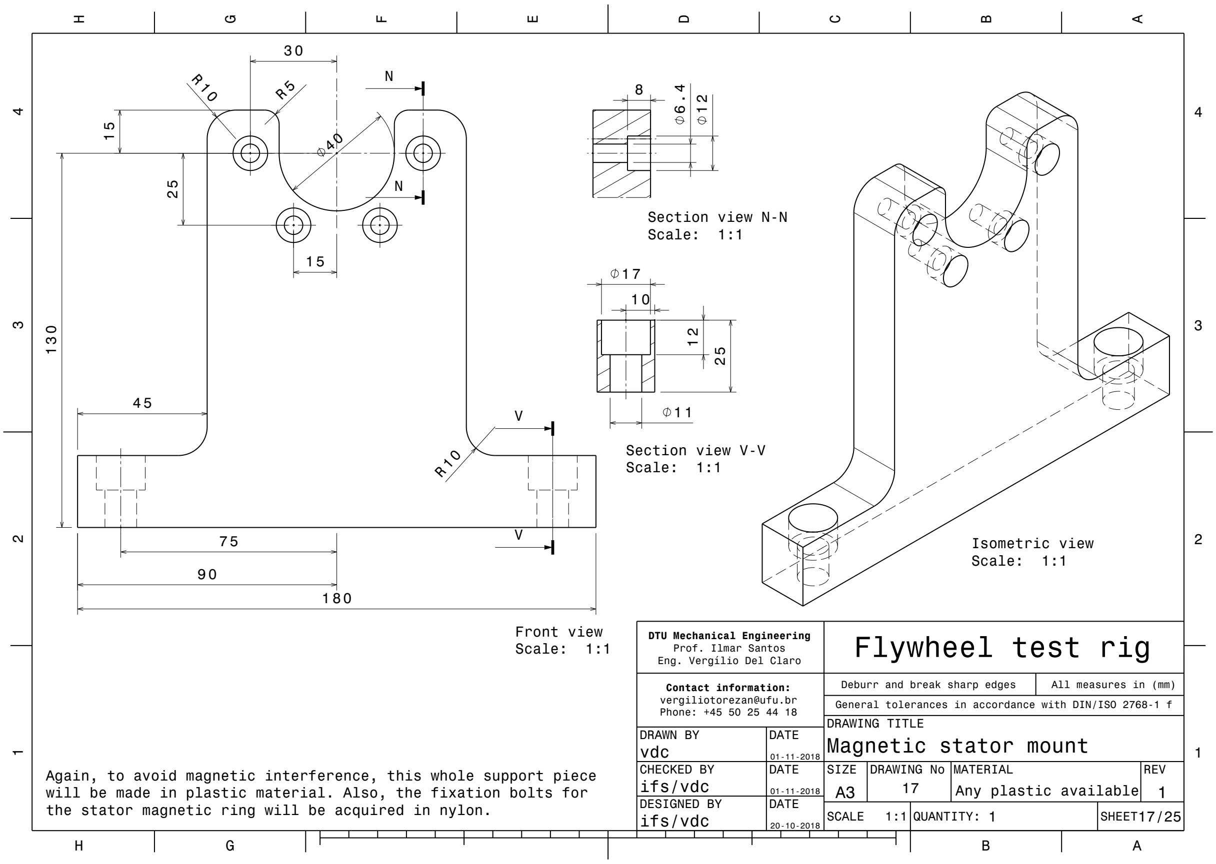

Again, to avoid magnetic interference, this whole support piece will be made in plastic material. Also, the fixation bolts for the stator magnetic ring will be acquired in nylon.

DTU Mechanical Engineering
Prof. Ilmar Santos
Eng. Vergílio Del Claro

Contact information:
vergiliotorezan@ufu.br
Phone: +45 50 25 44 18

Flywheel test rig

Deburr and break sharp edges — All measures in (mm)
General tolerances in accordance with DIN/ISO 2768-1 f

DRAWING TITLE: Magnetic stator mount

DRAWN BY vdc	DATE 01-11-2018				
CHECKED BY ifs/vdc	DATE 01-11-2018	SIZE A3	DRAWING No 17	MATERIAL Any plastic available	REV 1
DESIGNED BY ifs/vdc	DATE 20-10-2018	SCALE 1:1	QUANTITY: 1		SHEET 17/25

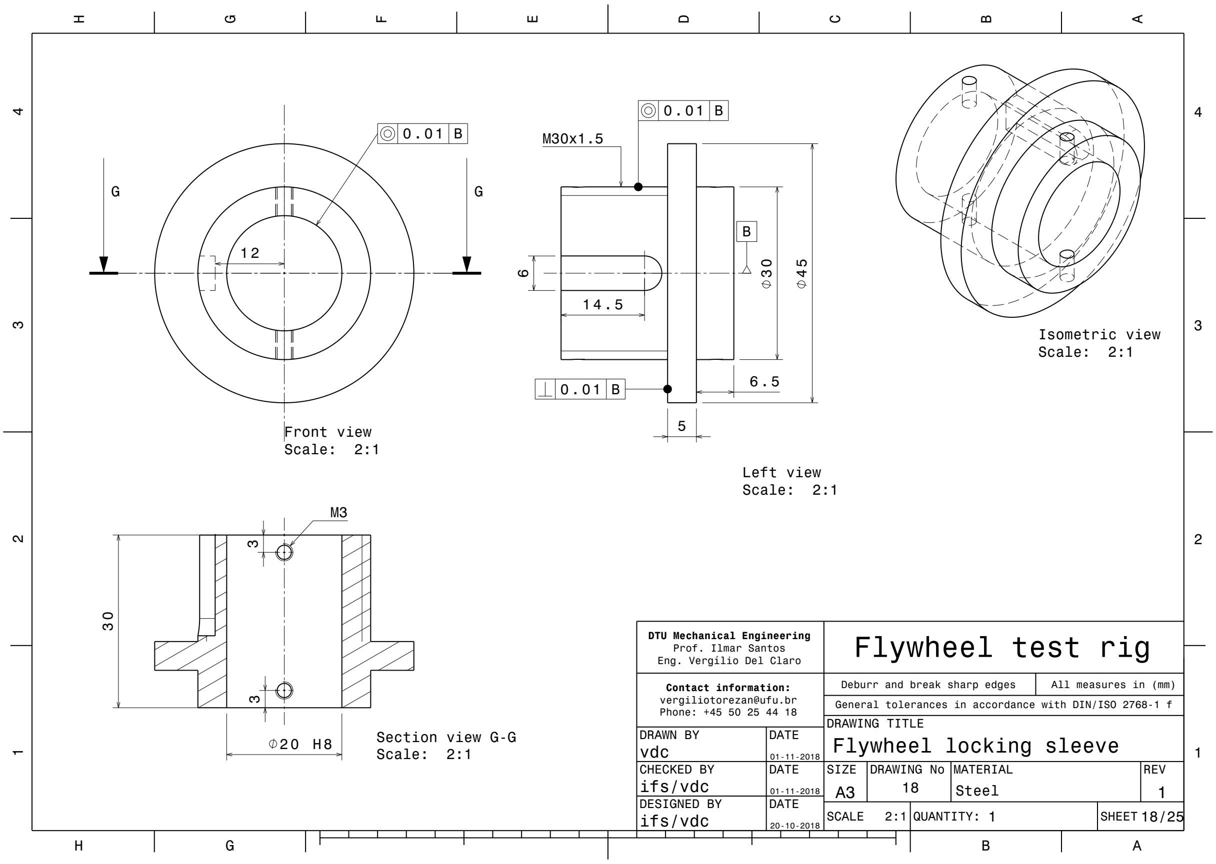

DTU Mechanical Engineering
Prof. Ilmar Santos
Eng. Vergilio Del Claro

Flywheel test rig

Contact information:
vergiliotorezan@ufu.br
Phone: +45 50 25 44 18

Deburr and break sharp edges
All measures in (mm)
General tolerances in accordance with DIN/ISO 2768-1 f

DRAWN BY vdc
DATE 01-11-2018
DRAWING TITLE Flywheel locking sleeve
CHECKED BY ifs/vdc
DATE 01-11-2018
SIZE A3
DRAWING No 18
MATERIAL Steel
REV 1
DESIGNED BY ifs/vdc
DATE 20-10-2018
SCALE 2:1
QUANTITY: 1
SHEET 18/25

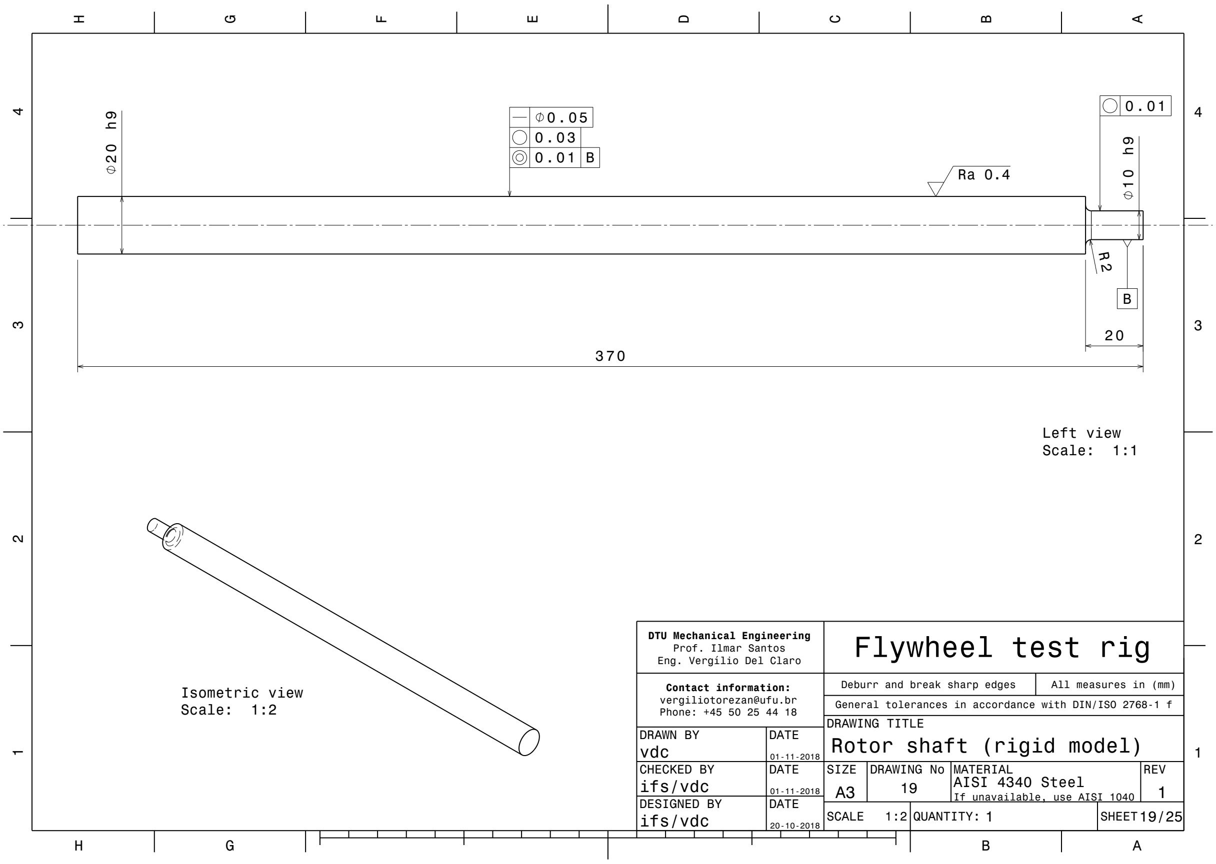

DTU Mechanical Engineering
Prof. Ilmar Santos
Eng. Vergilio Del Claro

Flywheel test rig

Contact information:
vergiliotorezan@ufu.br
Phone: +45 50 25 44 18

Deburr and break sharp edges
All measures in (mm)
General tolerances in accordance with DIN/ISO 2768-1 f

DRAWN BY vdc
DATE 01-11-2018
DRAWING TITLE Rotor shaft (rigid model)
CHECKED BY ifs/vdc
DATE 01-11-2018
SIZE A3
DRAWING No 19
MATERIAL AISI 4340 Steel
If unavailable, use AISI 1040
REV 1
DESIGNED BY ifs/vdc
DATE 20-10-2018
SCALE 1:2
QUANTITY: 1
SHEET 19/25

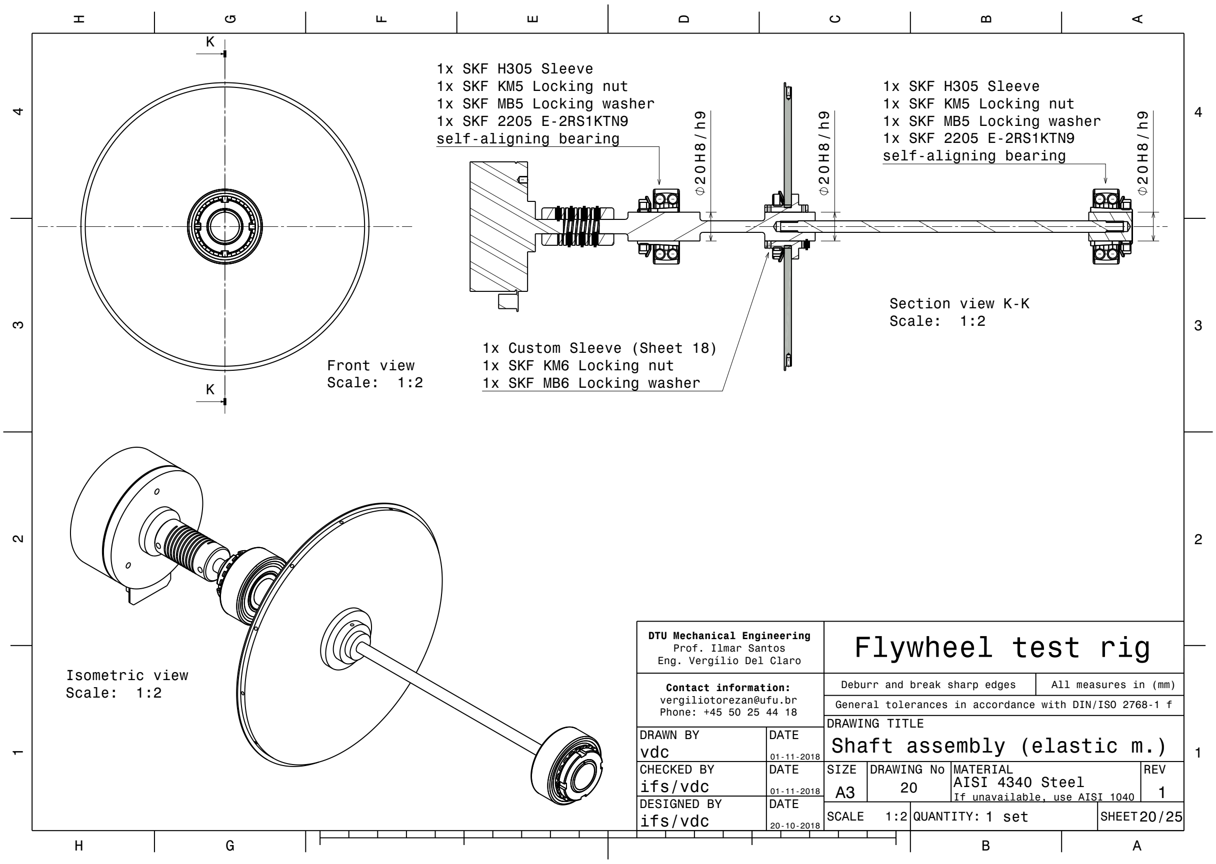

DTU Mechanical Engineering
Prof. Ilmar Santos
Eng. Vergílio Del Claro

Flywheel test rig

Contact information:
vergiliotorezan@ufu.br
Phone: +45 50 25 44 18

Deburr and break sharp edges | All measures in (mm)
General tolerances in accordance with DIN/ISO 2768-1 f

DRAWN BY vdc	DATE 01-11-2018	DRAWING TITLE Shaft assembly (elastic m.)			
CHECKED BY ifs/vdc	DATE 01-11-2018	SIZE A3	DRAWING No 20	MATERIAL AISI 4340 Steel If unavailable, use AISI 1040	REV 1
DESIGNED BY ifs/vdc	DATE 20-10-2018	SCALE 1:2	QUANTITY: 1 set		SHEET 20/25

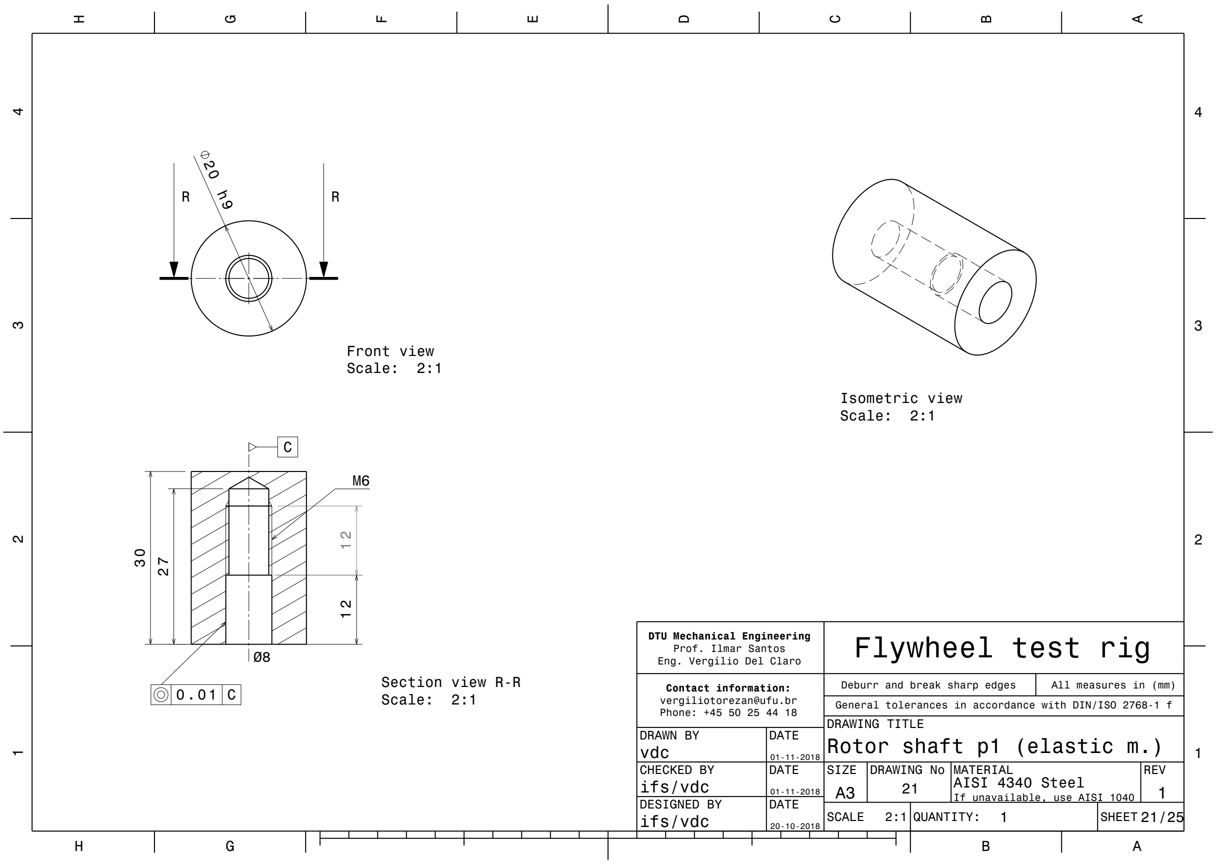

DTU Mechanical Engineering
Prof. Ilmar Santos
Eng. Vergílio Del Claro

Flywheel test rig

Contact information:
vergiliotorezan@ufu.br
Phone: +45 50 25 44 18

Deburr and break sharp edges | All measures in (mm)
General tolerances in accordance with DIN/ISO 2768-1 f

DRAWN BY vdc	DATE 01-11-2018	DRAWING TITLE Rotor shaft p1 (elastic m.)			
CHECKED BY ifs/vdc	DATE 01-11-2018	SIZE A3	DRAWING No 21	MATERIAL AISI 4340 Steel If unavailable, use AISI 1040	REV 1
DESIGNED BY ifs/vdc	DATE 20-10-2018	SCALE 2:1	QUANTITY: 1		SHEET 21/25

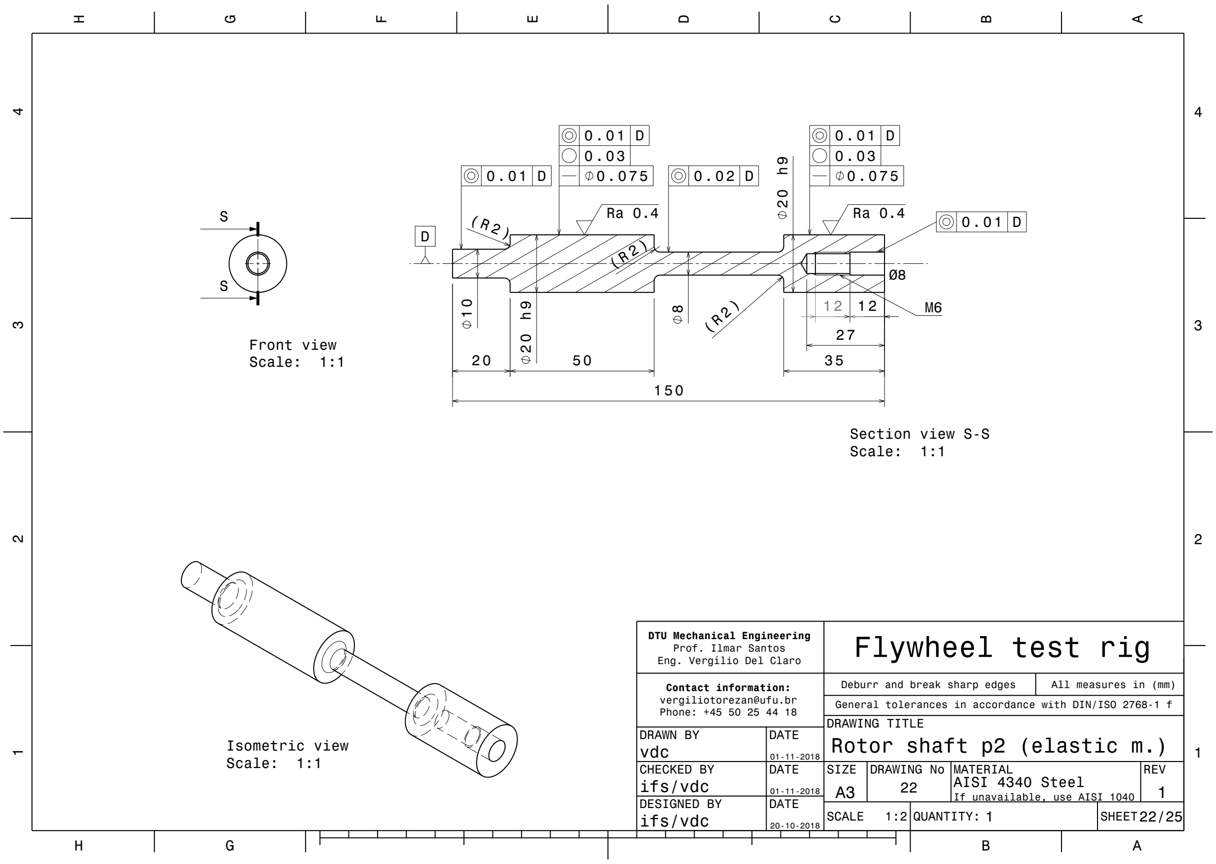

DTU Mechanical Engineering
Prof. Ilmar Santos
Eng. Vergilio Del Claro

Flywheel test rig

Contact information:
vergiliotorezan@ufu.br
Phone: +45 50 25 44 18

Deburr and break sharp edges | All measures in (mm)
General tolerances in accordance with DIN/ISO 2768-1 f

DRAWN BY: vdc | DATE: 01-11-2018
CHECKED BY: ifs/vdc | DATE: 01-11-2018
DESIGNED BY: ifs/vdc | DATE: 20-10-2018

DRAWING TITLE: Rotor shaft p2 (elastic m.)
SIZE: A3 | DRAWING No: 22 | MATERIAL: AISI 4340 Steel, If unavailable, use AISI 1040 | REV: 1
SCALE: 1:2 | QUANTITY: 1 | SHEET 22/25

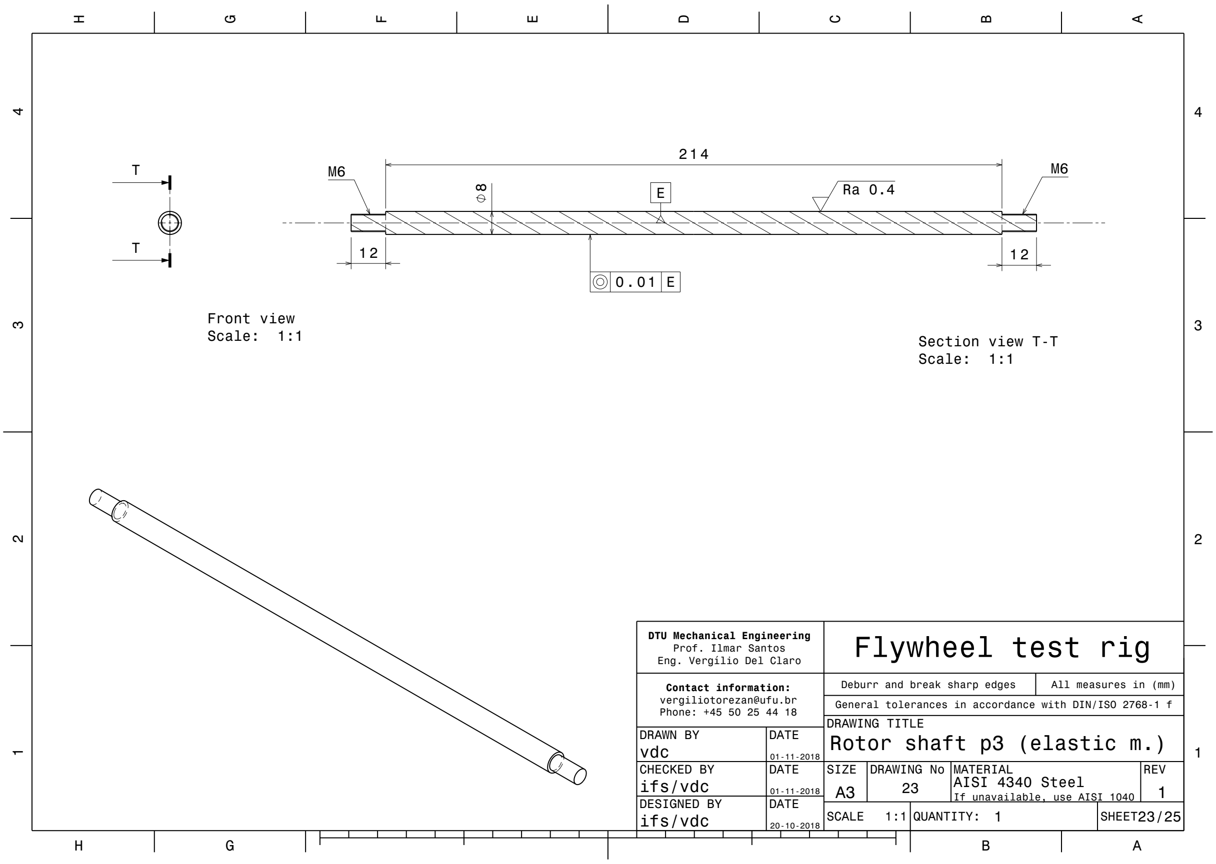

DTU Mechanical Engineering
Prof. Ilmar Santos
Eng. Vergilio Del Claro

Flywheel test rig

Contact information:
vergiliotorezan@ufu.br
Phone: +45 50 25 44 18

Deburr and break sharp edges | All measures in (mm)
General tolerances in accordance with DIN/ISO 2768-1 f

DRAWN BY: vdc | DATE: 01-11-2018
CHECKED BY: ifs/vdc | DATE: 01-11-2018
DESIGNED BY: ifs/vdc | DATE: 20-10-2018

DRAWING TITLE: Rotor shaft p3 (elastic m.)
SIZE: A3 | DRAWING No: 23 | MATERIAL: AISI 4340 Steel, If unavailable, use AISI 1040 | REV: 1
SCALE: 1:1 | QUANTITY: 1 | SHEET 23/25

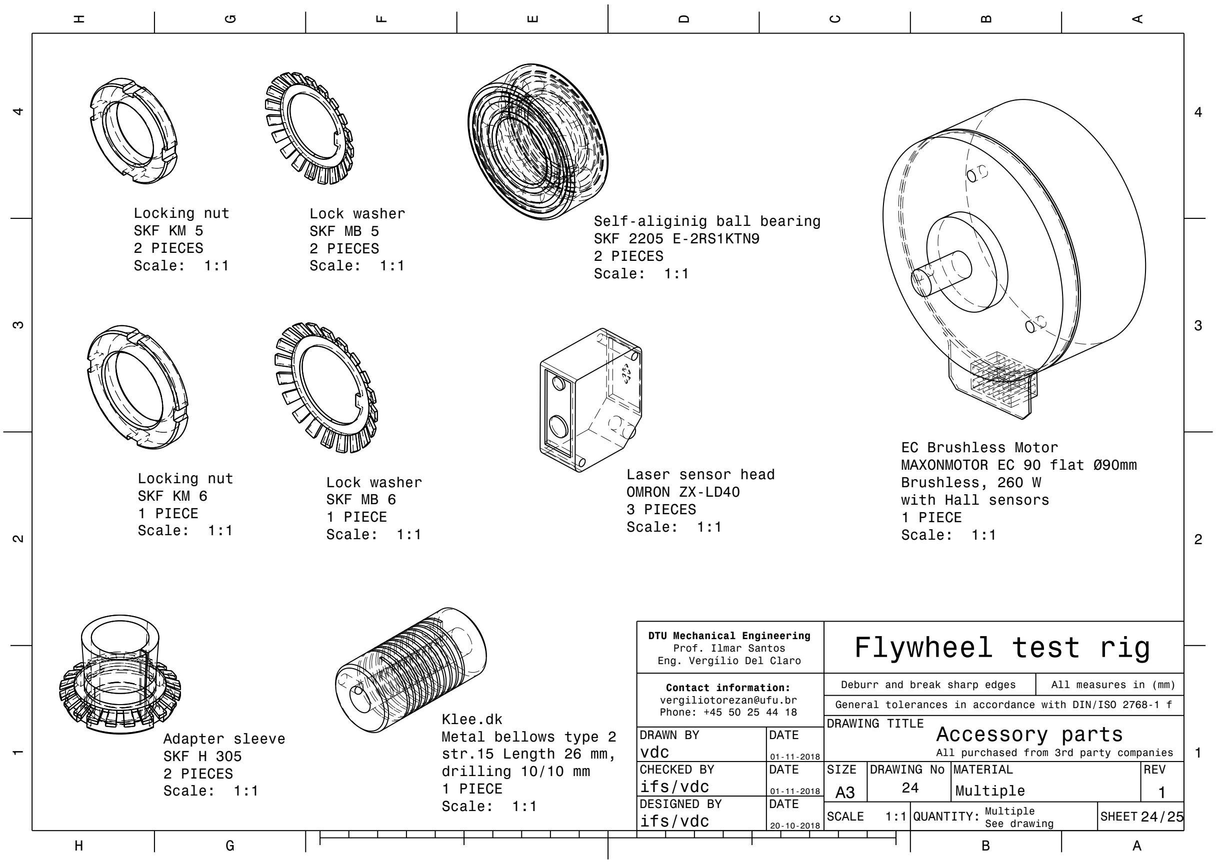

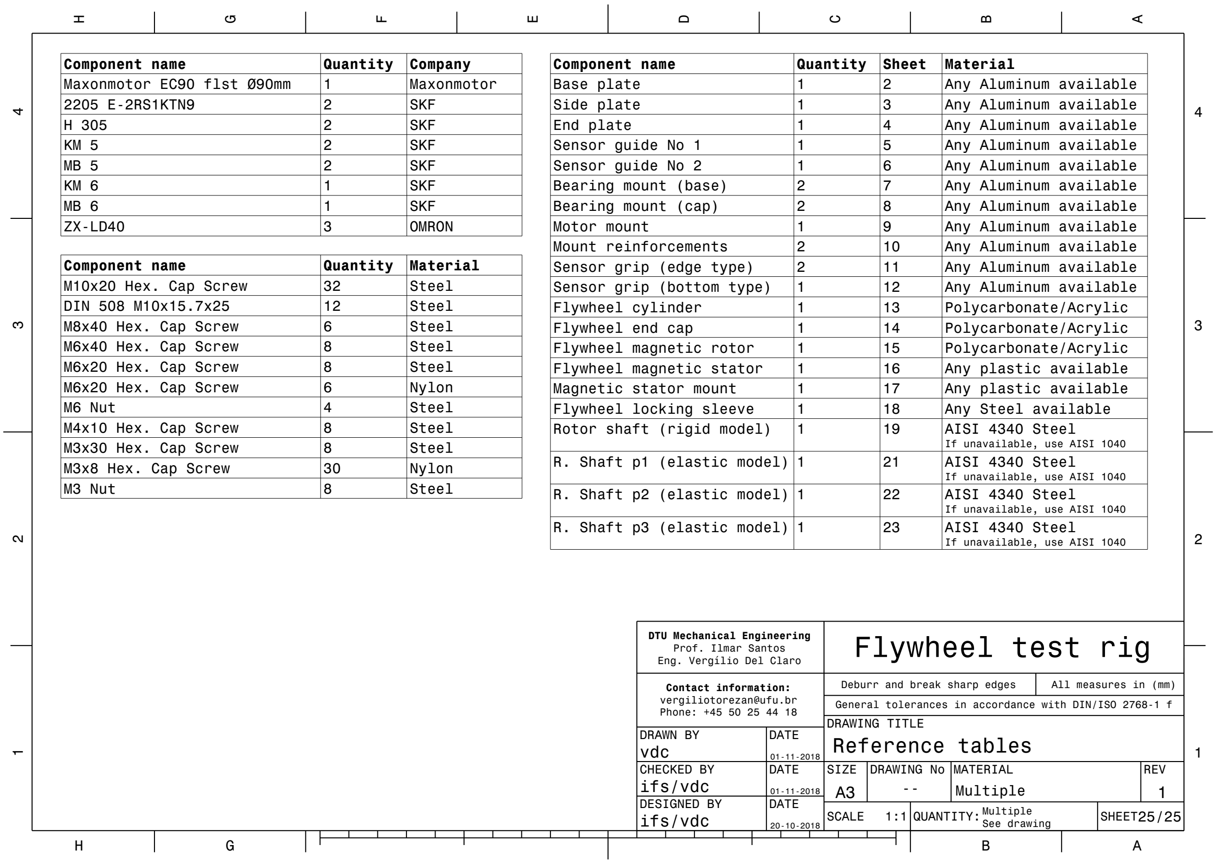

Component name	Quantity	Company
Maxonmotor EC90 flst Ø90mm	1	Maxonmotor
2205 E-2RS1KTN9	2	SKF
H 305	2	SKF
KM 5	2	SKF
MB 5	2	SKF
KM 6	1	SKF
MB 6	1	SKF
ZX-LD40	3	OMRON

Component name	Quantity	Material
M10x20 Hex. Cap Screw	32	Steel
DIN 508 M10x15.7x25	12	Steel
M8x40 Hex. Cap Screw	6	Steel
M6x40 Hex. Cap Screw	8	Steel
M6x20 Hex. Cap Screw	8	Steel
M6x20 Hex. Cap Screw	6	Nylon
M6 Nut	4	Steel
M4x10 Hex. Cap Screw	8	Steel
M3x30 Hex. Cap Screw	8	Steel
M3x8 Hex. Cap Screw	30	Nylon
M3 Nut	8	Steel

Component name	Quantity	Sheet	Material
Base plate	1	2	Any Aluminum available
Side plate	1	3	Any Aluminum available
End plate	1	4	Any Aluminum available
Sensor guide No 1	1	5	Any Aluminum available
Sensor guide No 2	1	6	Any Aluminum available
Bearing mount (base)	2	7	Any Aluminum available
Bearing mount (cap)	2	8	Any Aluminum available
Motor mount	1	9	Any Aluminum available
Mount reinforcements	2	10	Any Aluminum available
Sensor grip (edge type)	2	11	Any Aluminum available
Sensor grip (bottom type)	1	12	Any Aluminum available
Flywheel cylinder	1	13	Polycarbonate/Acrylic
Flywheel end cap	1	14	Polycarbonate/Acrylic
Flywheel magnetic rotor	1	15	Polycarbonate/Acrylic
Flywheel magnetic stator	1	16	Any plastic available
Magnetic stator mount	1	17	Any plastic available
Flywheel locking sleeve	1	18	Any Steel available
Rotor shaft (rigid model)	1	19	AISI 4340 Steel If unavailable, use AISI 1040
R. Shaft p1 (elastic model)	1	21	AISI 4340 Steel If unavailable, use AISI 1040
R. Shaft p2 (elastic model)	1	22	AISI 4340 Steel If unavailable, use AISI 1040
R. Shaft p3 (elastic model)	1	23	AISI 4340 Steel If unavailable, use AISI 1040

DTU Mechanical Engineering
Prof. Ilmar Santos
Eng. Vergílio Del Claro

Contact information:
vergiliotorezan@ufu.br
Phone: +45 50 25 44 18

Flywheel test rig

Deburr and break sharp edges | All measures in (mm)
General tolerances in accordance with DIN/ISO 2768-1 f

DRAWING TITLE
Reference tables

DRAWN BY vdc	DATE 01-11-2018				
CHECKED BY ifs/vdc	DATE 01-11-2018	SIZE A3	DRAWING No --	MATERIAL Multiple	REV 1
DESIGNED BY ifs/vdc	DATE 20-10-2018	SCALE 1:1	QUANTITY: Multiple See drawing		SHEET 25/25

Appendix B

Matrix of orthotropic material properties

The expanded equations for each individual term of the transversely orthotropic material matrix are presented. These are functions of β and θ, the out-of-plane and in-plane fiber angles, respectively, relative to the shaft longitudinal direction. β will be zero for the uni and bi-directional cases, however it is represented here for the sake of generality. In this formulation, the super index ^{k} defines the ply, in order to facilitate an automated numerical assembling of this matrix for any given number of layers. The terms with no super-index ^{k} come from the standard orthotropic material matrix, defined in Chapter 2.

$$C_{11}^k = C_{11} * cos(\beta)^4 + cos(\beta)^2 * sin(\beta)^2 * ((4 * C_{44} + 2 * C_{21}) * cos(\theta)^2 + (4 * C_{55} + 2 * C_{13}) * sin(\theta)^2) + sin(\beta)^4 * (C_{22} * cos(\theta)^4 + (4 * C_{66} + 2 * C_{23}) * cos(\theta)^2 * sin(\theta)^2 + C_{33} * sin(\theta)^4)$$

$$C_{12}^k = cos(\beta)^2 * sin(\beta)^2 * ((4 * C_{66} + 2 * C_{23}) * cos(\theta)^2 * sin(\theta)^2 + C_{33} * sin(\theta)^4 - 4 * C_{55} * sin(\theta)^2 + C_{22} * cos(\theta)^4 - 4 * C_{44} * cos(\theta)^2 + C_{11}) + (cos(\beta)^4 + sin(\beta)^4) * (C_{13} * sin(\theta)^2 + C_{21} * cos(\theta)^2)$$

$$C_{13}^k = sin(\beta)^2 * (C_{23} * (cos(\theta)^4 + sin(\theta)^4) + (C_{33} + C_{22} - 4 * C_{66}) * cos(\theta)^2 * sin(\theta)^2) + cos(\beta)^2 * (C_{13} * cos(\theta)^2 + C_{21} * sin(\theta)^2)$$

$$C^k_{14} = cos(\beta) * sin(\beta)^3 * (C_{22} * cos(\theta)^4 - (C_{21} + 2 * C_{44}) * cos(\theta)^2 - (4 * C_{66} + 2 * C_{23}) * cos(\theta)^2 * sin(\theta)^2 + (C_{13} + 2 * C_{55}) * sin(\theta)^2 + C_{33} * sin(\theta)^4) + cos(\beta)^3 * sin(\beta) * ((C_{13} + 2 * C_{55}) * sin(\theta)^2 + (C_{21} + 2 * C_{44}) * cos(\theta)^2 - C_{11})$$

$$C^k_{15} = sin(\beta)^3 * ((2 * C_{66} + C_{23} - C_{33}) * cos(\theta) * sin(\theta)^3 + (-2 * C_{66} - C_{23} + C_{22}) * cos(\theta)^3 * sin(\theta)) + cos(\beta)^2 * sin(\beta) * (2 * C_{44} - 2 * C_{55} + C_{21} - C_{13}) * cos(\theta) * sin(\theta)$$

$$C^k_{16} = cos(\beta)^3 * (C_{21} - C_{13}) * cos(\theta) * sin(\theta) + cos(\beta) * sin(\beta)^2 * ((2 * C_{66} + C_{23} - C_{33}) * cos(\theta) * sin(\theta)^3 + (-2 * C_{66} - C_{23} + C_{22}) * cos(\theta)^3 * sin(\theta))$$

$$C^k_{22} = cos(\beta)^4 * (C_{22} * cos(\theta)^4 + (4 * C_{66} + 2 * C_{23}) * cos(\theta)^2 * sin(\theta)^2 + C_{33} * sin(\theta)^4) + cos(\beta)^2 * sin(\beta)^2 * ((4 * C_{44} + 2 * C_{21}) * cos(\theta)^2 + (4 * C_{55} + 2 * C_{13}) * sin(\theta)^2) + C_{11} * sin(\beta)^4$$

$$C^k_{23} = cos(\beta)^2 * (C_{23} * (cos(\theta)^4 + sin(\theta)^4) + (C_{33} + C_{22} - 4 * C_{66}) * cos(\theta)^2 * sin(\theta)^2) + sin(\beta)^2 * (C_{13} * cos(\theta)^2 + C_{21} * sin(\theta)^2)$$

$$C^k_{24} = cos(\beta)^3 * sin(\beta) * (C_{22} * cos(\theta)^4 - (C_{21} + 2 * C_{44}) * cos(\theta)^2 - (4 * C_{66} + 2 * C_{23}) * cos(\theta)^2 * sin(\theta)^2 + (C_{13} + 2 * C_{55}) * sin(\theta)^2 + C_{33} * sin(\theta)^4) + cos(\beta) * sin(\beta)^3 * ((C_{13} + 2 * C_{55}) * sin(\theta)^2 + (C_{12} + 2 * C_{44}) * cos(\theta)^2 - C_{11})$$

$$C^k_{25} = sin(\beta)^3 * (C_{21} - C_{13}) * cos(\theta) * sin(\theta) + cos(\beta) * sin(\beta)^3 * ((2 * C_{66} + C_{23} - C_{33}) * cos(\theta) * sin(\theta)^3 + (-2 * C_{66} - C_{23} + C_{22}) * cos(\theta)^3 * sin(\theta) + (2 * C_{55} - 2 * C_{44}) * cos(\theta) * sin(\theta))$$

$$C^k_{26} = cos(\beta)^3 * ((2 * C_{66} + C_{23} - C_{33}) * cos(\theta) * sin(\theta)^3 + (-2 * C_{66} - C_{33} + C_{22}) * cos(\theta)^3 * sin(\theta)) + cos(\beta) * sin(\beta)^2 * (2 * C_{44} - 2 * C_{55} + C_{21} - C_{13}) * cos(\theta) * sin(\theta)$$

$$C^k_{33} = C_{33} * cos(\theta)^4 + (2 * (2 * C_{66} + C_{23})) * cos(\theta)^2 * sin(\theta)^2 + C_{22} * sin(\theta)^4$$

$$C^k_{34} = cos(\beta) * sin(\beta) * ((C_{33} + C_{22} - 4 * C_{66}) * cos(\theta)^2 * sin(\theta)^2 + C_{23} * (cos(\beta)^4 + sin(\beta)^4) - C_{13} * cos(\theta)^2 - C_{12} * sin(\theta)^2)$$

$C^k_{35} = sin(\beta) * ((-2 * C_{66} - C_{23} + C_{22}) * cos(\theta) * sin(\theta)^3 + (2 * C_{66} + C_{23} - C_{33}) * cos(\theta)^3 * sin(\theta))$

$C^k_{36} = cos(\beta) * ((-2 * C_{66} - C_{23} + C_{22}) * cos(\theta) * sin(\theta)^3 + (2 * C_{66} + C_{23} - C_{33}) * cos(\theta)^3 * sin(\theta))$

$C^k_{44} = (cos(\beta)^4 + sin(\beta)^4) * (C_{44} * cos(\theta)^2 + C_{55} * sin(\theta)^2) + cos(\beta)^2 * sin(\beta)^2 * (C_{11} + C_{22} * cos(\theta)^4 + (-2 * C_{44} - 2 * C_{12}) * cos(\theta)^2 + (-2 * C_{55} - 2 * C_{13}) * sin(\theta)^2 + (4 * C_{66} + 2 * C_{23}) * cos(\theta)^2 * sin(\theta)^2)$

$C^k_{45} = cos(\beta)^3 * (C_{44} - C_{55}) * cos(\theta) * sin(\theta) + cos(\beta) * sin(\beta)^2 * ((-2 * C_{66} - C_{23} + C_{22}) * cos(\theta)^3 * sin(\theta) + (2 * C_{66} + C_{23} - C_{33}) * cos(\theta) * sin(\theta)^3 + C_{55} - C_{44} - C_{12} + C_{13})$

$C^k_{46} = sin(\beta)^3 * (C_{44} - C_{55}) * cos(\theta) * sin(\theta) + cos(\beta)^2 * sin(\beta) * ((-2 * C_{66} - C_{23} + C_{22}) * cos(\theta)^3 * sin(\theta) + (2 * C_{66} + C_{23} - C_{33}) * cos(\theta) * sin(\theta)^3 + (C_{55} - C_{44} - C_{12} + C_{13}) * cos(\theta) * sin(\theta))$

$C^k_{55} = cos(\beta)^2 * (C_{55} * cos(\theta)^2 + C_{44} * sin(\theta)^2) + sin(\beta)^2 * (C_{66} * (cos(\theta)^4 + sin(\theta)^4) + (C_{33} + C_{22} - 2 * C_{66} - 2 * C_{23}) * cos(\theta)^2 * sin(\theta)^2)$

$C^k_{56} = cos(\beta) * sin(\beta) * (C_{66} * (cos(\theta)^4 + sin(\theta)^4) + (C_{33} + C_{22} - 2 * C_{66} - 2 * C_{23}) * cos(\theta)^2 * sin(\theta)^2 - C_{44} * sin(\theta)^2 - C_{55} * cos(\theta)^2)$

$C^k_{66} = sin(\beta)^2 * (C_{55} * cos(\theta)^2 + C_{44} * sin(\theta)^2) + cos(\beta)^2 * (C_{66} * (cos(\theta)^4 + sin(\theta)^4) + (C_{33} + C_{22} - 2 * C_{66} - 2 * C_{23}) * cos(\theta)^2 * sin(\theta)^2)$